INFORMATION TO USERS

This manuscript has been reproduced from the microfilm master. UMI films the text directly from the original or copy submitted. Thus, some thesis and dissertation copies are in typewriter face, while others may be from any type of computer printer.

The quality of this reproduction is dependent upon the quality of the copy submitted. Broken or indistinct print, colored or poor quality illustrations and photographs, print bleedthrough, substandard margins, and improper alignment can adversely affect reproduction.

In the unlikely event that the author did not send UMI a complete manuscript and there are missing pages, these will be noted. Also, if unauthorized copyright material had to be removed, a note will indicate the deletion.

Oversize materials (e.g., maps, drawings, charts) are reproduced by sectioning the original, beginning at the upper left-hand corner and continuing from left to right in equal sections with small overlaps.

Photographs included in the original manuscript have been reproduced xerographically in this copy. Higher quality 6" x 9" black and white photographic prints are available for any photographs or illustrations appearing in this copy for an additional charge. Contact UMI directly to order.

UMI®

Properties of the Molecular Interstellar Medium in the Lenticular Galaxy NGC 5866

Andrew G. LeBlanc

Submitted in partial fulfilment
of the requirements for the degree of
Master of Science

Saint Mary's University
Halifax, Nova Scotia

September 2001

0-612-65732-9

Canada

Table of Contents

LIST OF FIGURES

List of Tables

Certificate of Examination

Department of Astronomy and Physics
Saint Mary's University
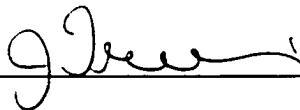
Dr. Gary Welch
Associate Professor of Astronomy and Physics
Saint Mary's University
(supervisor)

Dr. Francine Marleau
Assistant Professor of Astronomy and Physics
Saint Mary's University

Dr. George Mitchell
Professor of Astronomy and Physics
Saint Mary's University

Dr. Judith Irwin
Associate Professor of Physics
Queen's University
(External Reader)

Acknowledgements

A thesis is a strange thing. It starts off small and slowly becomes bigger. Almost unnoticeably, it grows to unmanageable proportions. Each new piece of information spawns more questions which need to be answered, chapters double in size, direction shifts, and focus becomes lost. At some point it gets tamed and cut back, rearranged and finally crystallizes into what you see before you.

Although from the outset it appears to be the work of a single author, this is hardly the case. Without the help of many people a thesis could never truly be finished. Outside influences are essential to the refinement of the text and the quality of the content. Naturally, in thanking the many people who have helped, the thesis supervisor gets first billing since they are involved from the inception, long before writing can even be considered. Also, most of the responsibility for the above mentioned editing falls into their lap. Dr. Gary Welch has provided consistent encouragement, advice, and insight throughout the entire process and deserves much of the credit. This includes everything from infinite patience during the slow times to resurrecting reference papers which were otherwise impossible to find or oblivious to me. Gary also needs to be included with the faculty thanks since he was a part of all of the soon to be mentioned groups.

The Master of Science in Astronomy programme at SMU covers 17520 hours; many of those hours were spend in the grad office. Peter started the program with me and has played an important role over the last 2 years, since, misery loves company. Any assignment, presentation, project, test or exam I had, so did Peter. Sandro, Trish, JR, Kevin and Dave deserve mention as well. Though they are of differing graduating classes, they shared in many of the late nights/early mornings with Peter and I, both astronomy and beer related (and not to forget Nick when mentioning beer). Many faculty members also enriched my time here. Dr. Turner, Dr. Guenther, Dr. Loken and Dr. Sarty provided me with an excellent education inside and outside the class room. Dr. Butler gave me the opportunity to take on roles of greater responsibility than normally assigned to a grad student at Saint Mary's. One of these was the chance to teach the forensic science class physics labs. These were both interesting and exciting to watch. Dr. Clarke and Dr. Turner, were on my comprehensive exam committee and Dr. Marleau, Dr. Mitchell and Dr. Irwin from Queen's assured that the final version of this thesis met the high standards of the scientific community and that I, too, did the same. Thanks also to Dave and Shawna for ensuring that the computers ran smoothly.

Finally, much gratitude needs to be extended to my loving family. Mom, Dad, Grandma, Grandpa, Aunt Janet, Uncle Johnny, Leah, Scott and Jill all helped through financial contributions, lending much moral support and providing constant encouragement. Sarah should be included here. Realistically, she should be thanked right after Gary, were it not for my desire to include her in with my family. She heard about every twist and turn along the way and provided much needed comfort and support during the slow times and even proof read a few of the chapters.

Thank you to everyone mentioned here and to any I have missed.

Abstract

The IRAM 30m telescope has been used to observe the J=1-0 transition of ^{12}CO at several positions along the central dust lane of NGC 5866. The data were used to determine the large-scale properties of the molecular interstellar medium. We find that the interstellar medium mass, $M(H_2) = 4.55 \pm 0.43 \times 10^8$ M⊙, is consistent with simple mass-return calculations from evolved stars (e.g. Faber & Gallagher, 1976). A computer model was employed to constrain the distribution and kinematics of the gas, by attempting to simulate the multi-position spectroscopy. The gas is found to be in a broken Gaussian ring-like distribution with several warmer areas mostly found on the red shifted side. Rotation velocities much higher than those reported for bot the stars and the ionized gas are required to reproduce the observed CO line width. The star formation rate is ≈ 0.05 M⊙/yr from Hα data, about average for an S0 galaxy, suggests that NGC 5866 is in mass balance based on the calculated mass return rate. The origin of the gas is most likely internal. However, the rapid rotation of the gas, a $M_{H_2}/M_{HI} \geq 3.5$, and evidence for a higher star formation rate in the past suggest that the gas might have been perturbed by an outside influence.

Chapter 1

Introduction

1.1 The S0 Galaxy Class

Lenticular (S0) galaxies present interesting laboratories for testing theories of the interstellar medium (ISM), galaxy interaction and galaxy formation. The S0 class of galaxies was not discovered, but first proposed in order to complete Hubble's "tuning fork" diagram, illustrating possible galactic evolution in his landmark book, *The Realm of the Nebulae* (Hubble, 1936). Hubble's tuning fork diagram, shows a sequence of increasingly elongated ellipticals (E0-E7) ending with the S0 class and then bifurcating into spiral branches showing increasingly extended spiral structure, one with a central bar (SBa-SBc), one without bars (Sa-Sc). When discussing galactic evolution, we interpret the sequence to go from spiral to elliptical, however, ellipticals, S0s and Sas are referred to as early-type galaxies based on Hubble's original suggestion. The formation of S0 galaxies remains a topic of debate. Some believe that later type spirals lose their angular momentum and heat up their stars through interaction with other galaxies or the

intergalactic medium in dense clusters, eventually ending up as an early-type (Spitzer & Baade, 1951, Gunn & Gott, 1972, Icke, 1985, Dressler, 1997). Others argue that a lenticular galaxy can be formed simply by having a normal spiral exhaust its gas supply through star formation (Sandage, Freeman & Stokes, 1970). Either way, the S0 galaxy class is the keystone to the whole evolutionary sequence since lenticulars are regarded as transition objects between the ellipticals and the spirals. After writing *The Realm of the Nebulae*, Hubble went on to find many examples of the S0 class but did not publish on them specifically (Sandage, Sandage & Kristian, eds., 1975). The first true description of the S0 galaxy class was not published until 1961 in the *Hubble Atlas of Galaxies* (Sandage, 1961).

Lenticular galaxies get their name from their double convex lens-like appearance. An S0 galaxy seen edge-on has a large bulge and a visible disk with no spiral structure. The class is divided into 3 major subclasses, $S0_1$, $S0_2$, $S0_3$ in order to further illustrate the transition between elliptical and spiral galaxies. The $S0_1$ subclass is closest to an elliptical in appearance and is the "earliest" form of S0 galaxy. The $S0_3$ subclass is closest to normal spirals, being characterized by the presence of a dust lane within the disk when viewed edge-wise (Sandage, 1961). NGC 5866 is a good example of an $S0_3$ galaxy.

1.2 The Lenticular Interstellar Medium

The original opinion concerning lenticular galaxies was that they are dead, in the sense of having no appreciable interstellar medium (ISM) and no longer creating new stars. Faber

& Gallagher (1976) showed in their seminal work that all early-type galaxies should, however, presently have robust ISMs due to mass return from dying stars. Without continuous star formation or some other way of removing gas, an easily detectable ISM should develop in a Hubble time. More recent studies, with more sensitive equipment, have confirmed that, indeed, ellipticals and S0 galaxies do have some form of an ISM in many cases (see Henkel & Wiklind, 1997, for a review of the molecular ISM, Knapp, 1998, for a general overview). However, despite this theoretical prediction and numerous observations, many early-type galaxies show only a sparse ISM or none at all. If all lenticulars have dying stars returning gas, where is this gas going?

Most S0 galaxies are found within dense clusters like the Virgo and Coma clusters of galaxies. Looking back in time at high redshifts shows that the spirals were once more common than they are today, whereas early-types were less common (e.g. Dressler *et al.*, 1997). These two observations have lead many to speculate that early-type galaxies form from spiral galaxies and that the environment must play an important role. Dressler (1980) showed that there is a morphology-density relationship: although all types of galaxies are found in all environments, the number of S0s per unit volume rises with number of galaxies per unit volume. That seems to confirm that at least in some cases, S0s are formed through environmental influences. In high density regions, S0s most likely form from normal spiral galaxies which have their gas removed by interaction with other galaxies or through ram-pressure stripping (Gunn & Gott, 1972) by the hot intergalactic medium (IGM), whose presence in dense galaxy clusters is revealed through its X-ray emission.

Galaxy interaction is a convenient hypothesis since it can also explain why some early-type galaxies have an interstellar medium. A second interaction, after the one which presumably formed the S0 galaxy, provides an accretion source to replenish the lenticular's ISM. Kinematical studies of the gas in S0s suggests that the ISM has been accreted from external sources, at least in some cases (Bertola *et al.*, 1992). The most convincing example of an external origin for gas in an S0 is counter-rotation with respect to the stars, since it is very hard to explain this from an internal origin standpoint (Bertola *et al.*, 1992).

The previously discussed S0 formation theories and ISM evolution scenarios fall short when discussing field S0s since none of the cluster conditions, such as, an intergalactic medium or large local number density of galaxies, exist which could cause a morphological transformation or an ISM exchange. For this reason, field S0s are interesting to study. NGC 5866, the focus of this work, is most likely in a loose group of galaxies but this environment is not comparable to those in the Virgo and Coma clusters due to the lower number density of galaxies and lack of an observed IGM. Could similar mechanisms be effective in such seemingly different environments? This seems doubtful, but there are other ways of removing gas from a galaxy which do not require interaction. Winds from type Ia supernovae have been shown to be effective at removing any gas returned to the ISM from dying stars (Matthews & Baker, 1971). Also, star formation cannot be ruled out in these galaxies. A starburst period can easily deplete much of the gas by converting it into stars and expelling the remaining gas by type II supernovae.

1.3 Motivation

The study of molecular gas in galaxies is important since new stars form out of this cool gas (see Young & Scoville, 1991, for an overview) and also because of a significant fraction of the total ISM might be in molecular form. CO observations provide one of the easiest ways of studying the molecular ISM since many of its rotational transitions are observable in radio wavelengths through the Earth's atmosphere. Studying a galaxy's molecular gas kinematics and distribution provides powerful clues as to how the galaxy formed and what has happened to the galaxy in the past, in terms of interactions and star formation histories.

Shedding light on the competing theories concerning the origin of the ISM in lenticulars and presenting a comprehensive picture of what a typical S0 galaxy is like are the motivation behind a volume limited survey of the cool ISM in S0 galaxies, currently being performed by Welch & Sage (2001). The survey members were chosen based on distances and morphologies published in the Tully (1988) *Nearby Galaxies Catalogue*. The survey looks for ^{12}CO in the J=1-0 and J=2-1 transitions and also for atomic Hydrogen, HI.

This work presents a study of one of the survey members, NGC 5866, using extensive ^{12}CO J=1-0 data from the Institut de Radioastronomie Millimetrique (IRAM) 30m telescope. The goal is to provide a general overview of what the cool interstellar medium is like in NGC 5866. Discussion on the molecular gas mass, and how it compares to

other interstellar matter phases (HI, dust) will be presented along with details of the molecular gas distribution and kinematics gleaned from a simple computer model.

CO has been previously detected in NGC 5866. The central questions of *where did the ISM come from?* and *where is the gas going?* will be answered through analysis of the above and by comparing the results to published statistics on the S0 class in general in order to present a complete picture of the cool ISM in NGC 5866. In general, ISM origin theories fall into two categories, internal or external. If the gas in NGC 5866 is of internal origin, the gas evolved completely in a "closed box", if its origin is external, the gas was captured from some other source such as a dwarf companion. This is perhaps an oversimplification as there may only be partial stripping in an interaction or simply a perturbation of the gas.

NGC 5866 should have an appreciable ISM based on the simple prediction of Faber & Gallagher (1976). The mass return rate and the accumulated mass of the ISM are found by assuming a planetary nebulae birth rate and mass and scaling by the size of the galaxy, reflected by the galaxy's bolometric luminosity. Integrating over a given time period reveals the predicted ISM mass. The planetary nebula birth rate used is 9.2×10^{-12} /yr/$L_\odot$(bol) (Peimbert, 1993), and individual planetary nebulae are assumed to have a mass of 0.3 $M_\odot$, which gives a yearly mass loss rate of 2.76×10^{-12} $M_\odot$/yr/$L_\odot$(bol). The bolometric luminosity of NGC 5866 is 3.77×10^{10} $L_\odot$ (bolometric correction from Peimbert, 1993), yielding a mass return rate (MRR) of

$$MRR = 0.10 \ M_\odot/yr \qquad (1.1)$$

Integrating this value over 10^{10} years gives the predicted ISM mass from stellar material returned to interstellar space,

$$M_{ISM} = 10^9 \ M_\odot \qquad (1.2)$$

The mass given in equation 1.2 is on the order of what any search for an interstellar medium in NGC 5866 should find. Due to the simple nature of this calculation, the mass found here can only be used as a guideline. However, appreciable deviation from this value, either up or down, would indicate an external influence. Other quantities such as the star formation rate and star formation efficiency will be discussed in order to answer the second question.

1.4 NGC 5866

NGC 5866 is an edge-on, SO_3 galaxy at a distance of 15.3 Mpc, located in the NGC 5907 group of galaxies, along with other bright members, NGC 5907 and NGC 5879. The galaxy has a prominent dust lane tilted by $\sim 2\text{-}5°$ from the optical major axis (Burbidge & Burbidge, 1960, Bertola *et al.*, 1992), and is a strong infrared emitter having been detected by the Infrared Astronomical Satellite (IRAS). The Röntgen Satellite (ROSAT) X-ray observatory satellite found X-ray emission from NGC 5866 with a X-ray luminosity of $\sim 2.8 \times 10^{40}$ erg/s in the 0.1-2 keV band (Pellegrini, 1994). CO was first detected in NGC 5866 by Thronson *et al.* (1989) and Wiklind & Henkel (1989). Wiklind & Henkel (1989) reported on the first partial mapping of the CO in this galaxy and found that the CO followed the optical dust lane but did not publish their map. Previous studies give estimates of the H_2 mass from CO data in the range of $\sim 10^8$ solar masses, $M_\odot$, (Wiklind & Henkel, 1989, Thronson *et al.*, 1989, Young *et al.*, 1995, Taniguchi *et*

al.,1994) but no positive detection of HI has been made. The upper limits on 21 cm emission give an atomic Hydrogen mass of no more than $\sim10^8$ M$\odot$ (e.g. Gallagher, Faber & Balick 1975, Knapp & Gunn, 1982, Balkowski & Chamaraux, 1983 Haynes *et al.*, 1990). From [C II] (158 μm) and [O I] (63 μm) emission lines, Malhotra *et al.* (2000) find that the ultraviolet emission from an old stellar population is 2-3 times less than that needed to heat the warm ISM (100K). Could the difference be made up from newly formed stars? Shields (1991) performed a survey of Hα emission in X-ray selected, early-type galaxies, finding that the emission from NGC 5866 is extended over the inner $\sim$4 kpc of the galaxy disk and not confined to the nuclear region as seen in the other galaxies in the sample. NGC 5866 was the only case to show this kind distribution for its Hα emission in the sample. A large molecular ISM, strong far infrared (FIR) emission and extensive Hα emission point to ongoing star formation in this galaxy.

Chapter 2

Observations and Data Reduction

The IRAM 30m telescope, located on Pico Veleta, Spain, was used to observe [12]CO emission from NGC 5866. The J=1-0 (115 GHz) transition was observed at 9 locations along the optical major axis November, 1998. The observations were made by G. A. Welch and L. J. Sage as part of a volume limited survey of nearby lenticular galaxies. The telescope main beam has a FWHM = 20.9" (1.55 kpc at a distance of 15.3 Mpc) for the J=1-0 transition, and the telescope was moved by 11" between observations. Table 2.1 lists the sky positions of each of the pointings. The data were collected using heterodyne receivers which use superconductor-insulator-superconductor mixers and operate in the lower side band mode. The data were obtained in beam-switching mode using a throw of 240" in azimuth at a rate of 1 Hz. Telescope pointing and focus were checked approximately every 2 hours using a bright quasar or the planet Mars. System temperatures were typically 300-400 K for [12]CO J=1-0. The raw spectra were collected

using a filterbank spectrometer with a resolution of 1 MHz and a bandwidth of 512 MHz, centred at 745 kms^{-1}. The intensity was measured in terms of main beam temperature.

Data were processed by the author using the CLASS software package for single dish observations. All individual 4 minute scans were summed for each pointing after removing any "bad" channels. The data were binned to a resolution of 10.4 kms^{-1} using a Hanning smoothing procedure. Each binned spectrum was inspected by eye and a window created to include the emission feature. Linear baseline subtraction then provided values for the integrated intensity (area under the line) and RMS deviation in the baseline. Figures 2.2-2.10 show the pointing data spectra along with the window showing the line width, located under the baseline. The term "line width" is defined here as the velocity range over which there is obvious signal.

Table 2.1 Coordinates of the 11 ^{12}CO J=1-0 observations. The centre pointing (number 5) is located at $\alpha(1950) = 15^h05^m7^s.0$, $\delta(1950) = 55°57'20"$.

Pointing	Integration Time (minutes)	Offsets (") ΔR.A.	ΔDec
1	24.00	-34.67	27.09
2	26.00	-26.00	20.31
3	24.00	-17.34	13.54
4	24.00	-8.67	6.77
5	36.00	0.00	0.00
6	40.00	8.67	-6.77
7	24.00	17.34	-13.54
8	24.00	26.00	-20.31
9	24.00	34.67	-27.09

Figure 2.1 The IRAM 30m CO J=1-0 observations are superposed on an optical image of NGC 5866. The FOV is 108" × 85". Circles show the telescope FWHM of 21" for the J=1-0 transition.
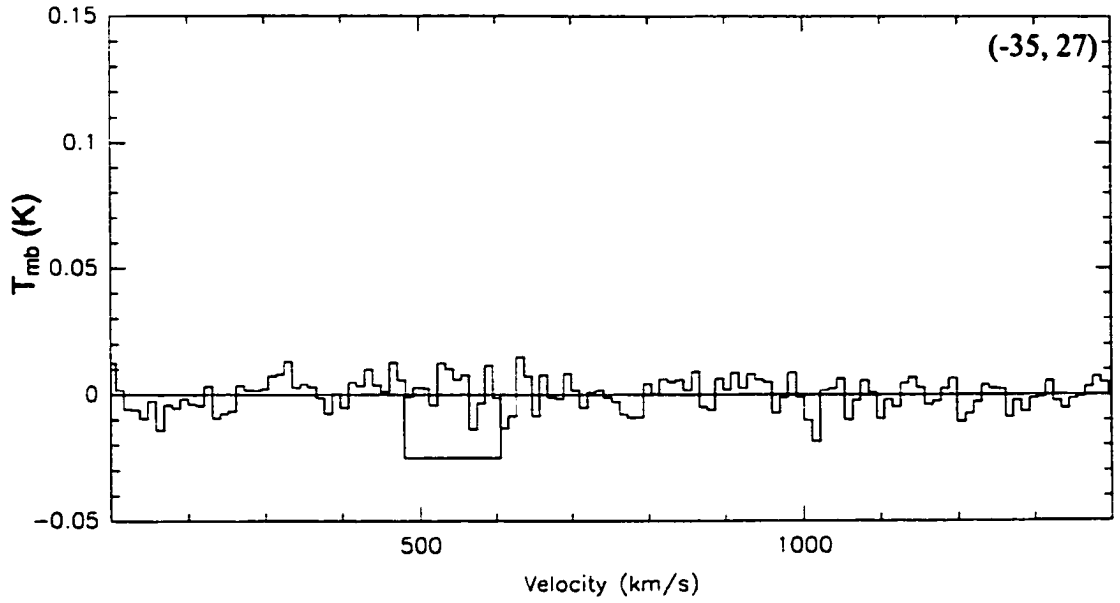
Figure 2.2 This and the following 8 figures show the pointing data and the window used to estimate the line width. The IRAM 30m data for the –35, 27 arcseconds offset (right ascension and declination, respectively) with the baseline subtracted. The line window is also shown under the baseline. The offset in arcseconds is presented in the upper right hand corner.
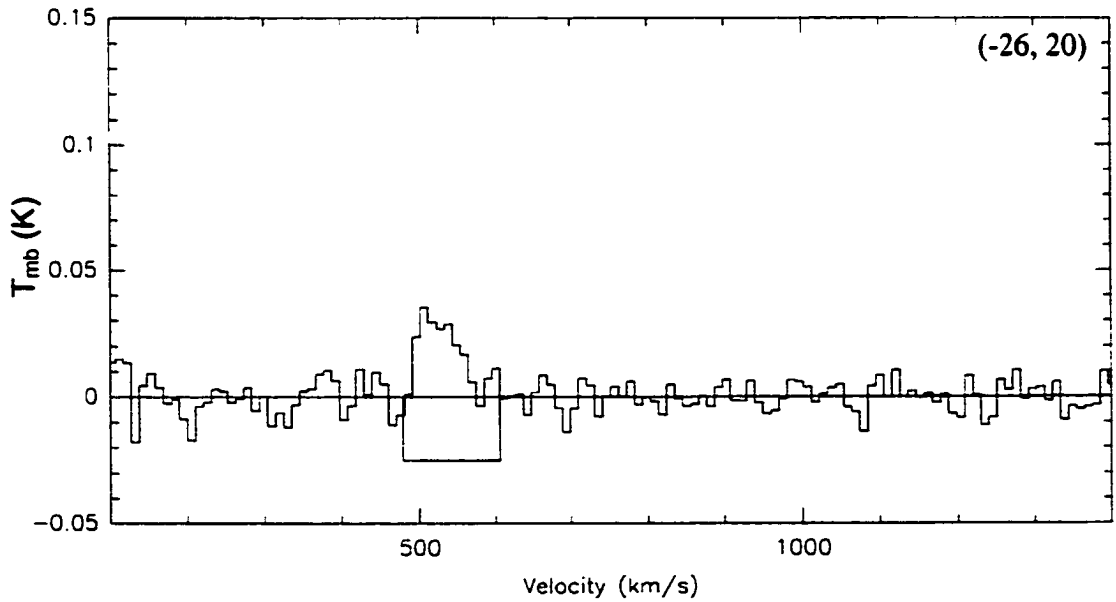
Figure 2.3 Same as figure 2.2 except the telescope offset is –26, 20 arcseconds
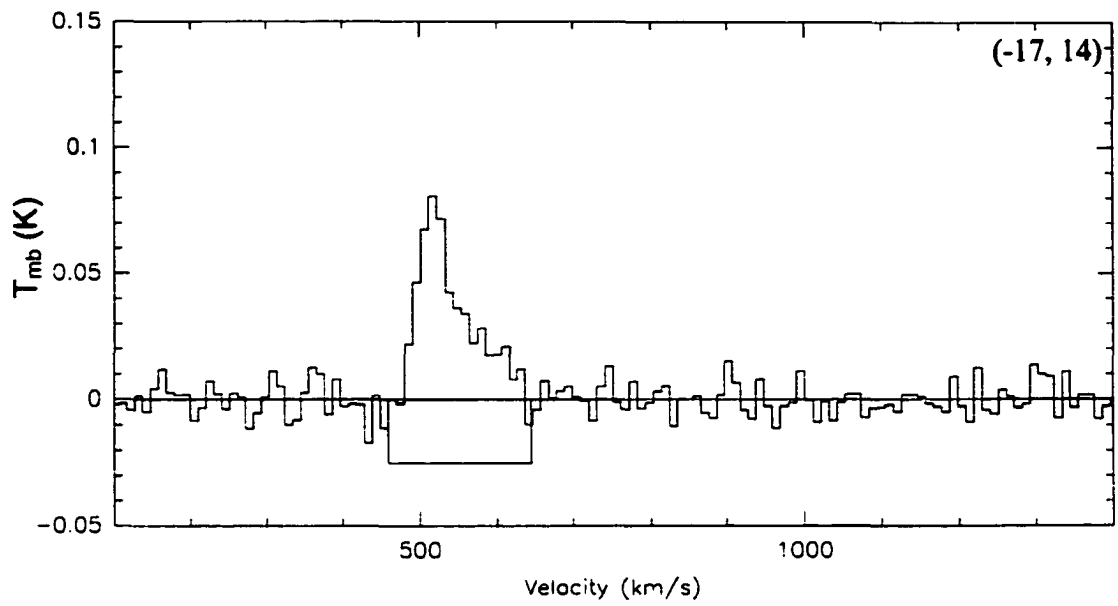
Figure 2.4 Same as figure 2.2 except the telescope offset is –17,14 arcseconds.
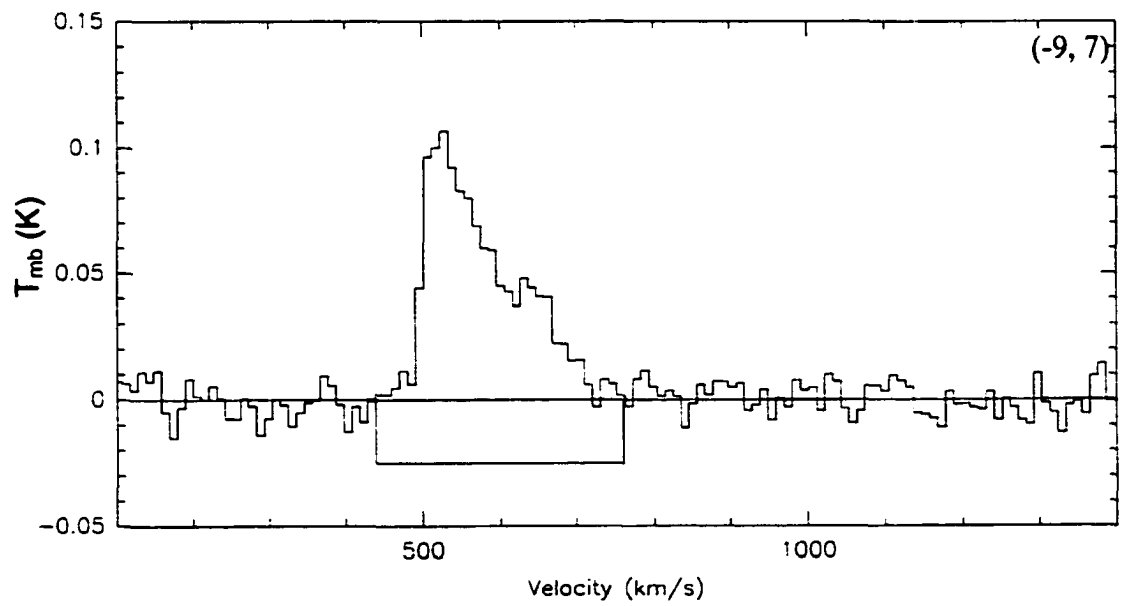
Figure 2.5 Same as figure 2.2 except the telescope offset is –9,7 arcseconds.
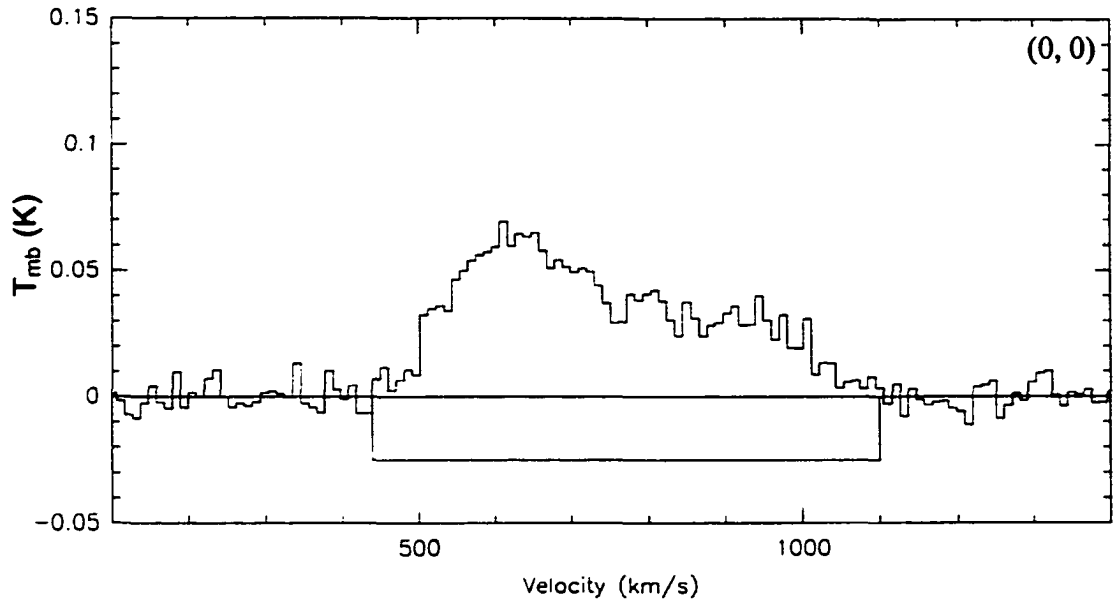
Figure 2.6 Same as figure 2.2 except the telescope offset is 0,0 arcseconds.
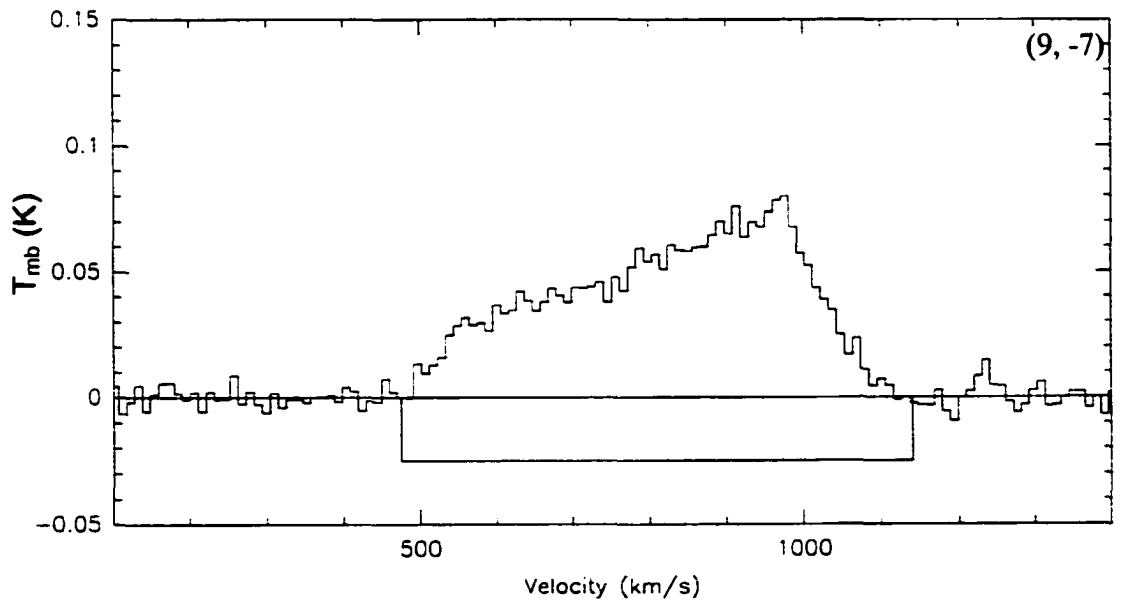
Figure 2.7 Same as figure 2.2 except the telescope offset is 9,-7 arcseconds
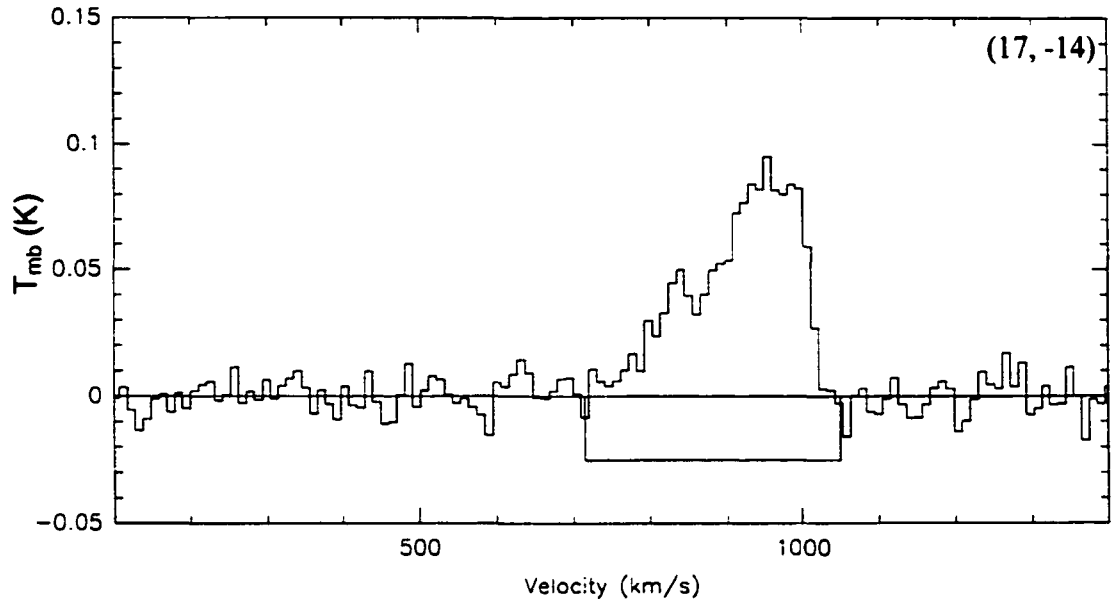
Figure 2.8 Same as figure 2.2 except the telescope offset is 17,-14 arcseconds.
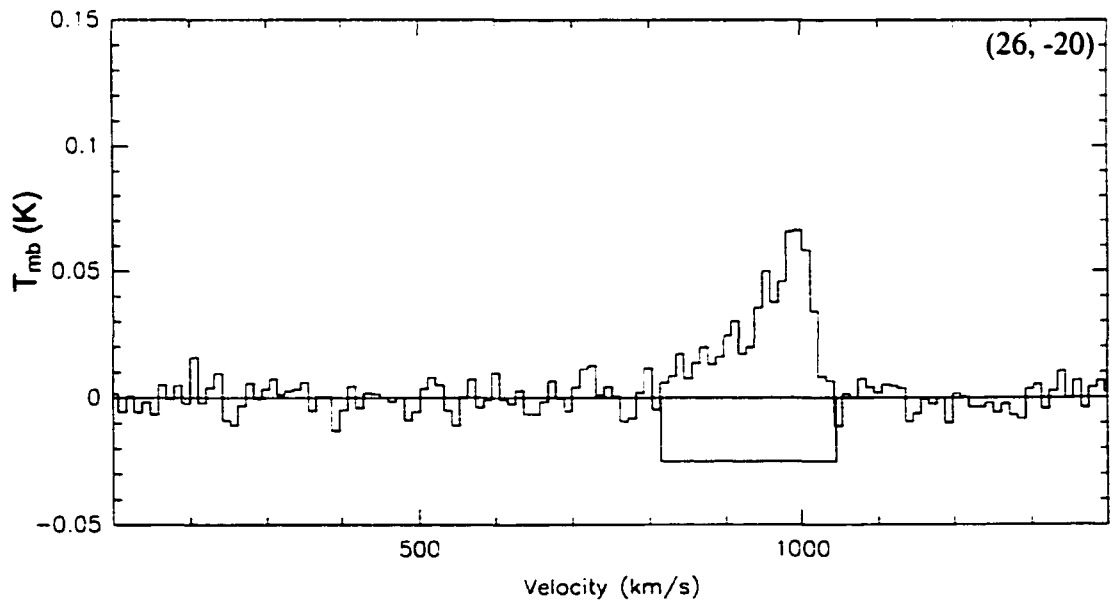
Figure 2.9 Same as figure 2.2 except the telescope offset is 26,-20 arcseconds.
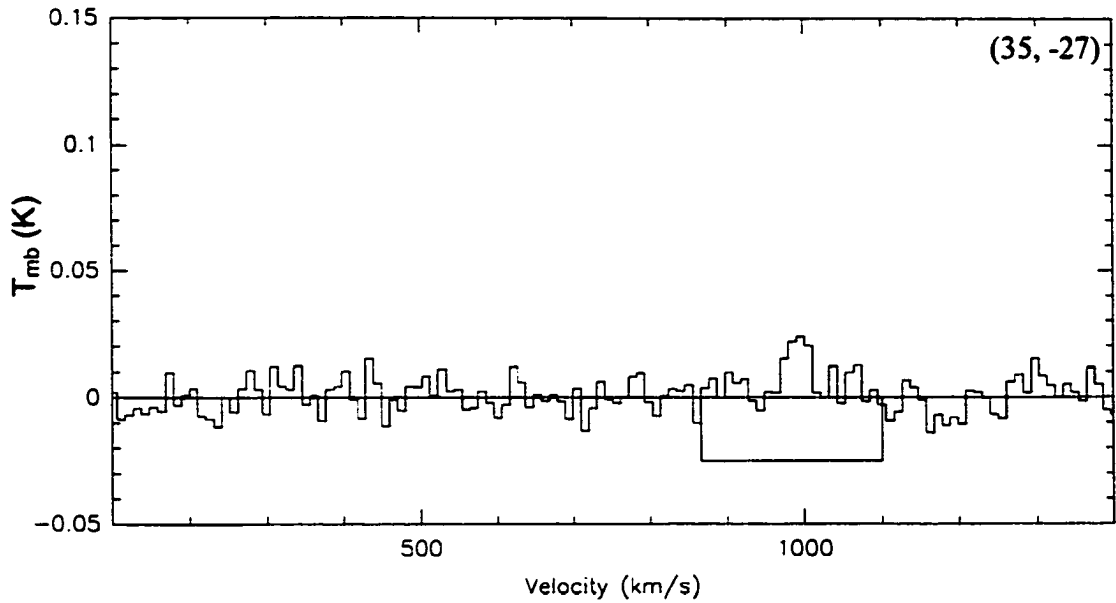
Figure 2.10 Same as figure 2.2 except the telescope offset is 35,-27 arcseconds.

The large line widths show that the molecular gas is rotating quickly, with a maximum velocity on the order of 300 kms^{-1}. The outer pointings (figures 2.3-2.5 and figures 2.8-2.9) show little evidence for a drop in rotation speed at large radii. The data show that the CO emission lines are complex with peaks and dips seen in the central pointings (figures 2.5-2.8). The centre pointing (figure 2.6) clearly shows more power at lower velocities (below the centre velocity of 745 kms^{-1}) compared to higher velocity bins (above 745 kms^{-1}). The centre pointing data also suggest a dip in power around the systemic velocity, suggesting less gas in the centre of the galaxy. The 9,-7" pointing (figure 2.7) shows significant signal over almost the same velocity range as the centre pointing. This is interesting since the same effect is not seen when the telescope beam is pointed on the opposite side of the galaxy (figure 2.5). Both the -9,7" and the 17,-14"

pointings (figures 2.5 and 2.8 respectively) show a "saw tooth" shape with a secondary peak around 100 kms^{-1} on either side of 745 kms^{-1} in the respective pointing. The outer most pointings preserve the saw tooth shape in roughly the same velocity bins with progressively weaker signal. This implies that all of the CO in the central region of NGC 5866 has been seen by these observations.

Chapter 3

Results

3.1 The Global Properties of the Molecular ISM

The following gives an overview of the various molecular ISM properties found for NGC 5866 and how the data were used to obtain them. A short discussion on each result is presented, which will be elaborated on in the next chapter.

3.1.1 H_2 Mass

In this study the molecular hydrogen content is gleaned from the ^{12}CO data. CO is thought to be a good tracer of molecular hydrogen since both molecules form in cool regions ($\lesssim 100$ K), and are believed to be well mixed (see Young & Scoville, 1991, for an overview).

The first step in finding the molecular hydrogen mass, $M(H_2)$, is to integrate the main beam temperature over velocity for all the pointings, as in equation 3.1, to get the integrated CO intensity, I_{CO}.

$$I_{CO} = \int T_{MB} dV \quad \text{(K kms}^{-1}\text{)} \tag{3.1}$$

with I_{CO} in K kms^{-1}, velocity, V, in kms^{-1} and main beam temperature in Kelvins, K. The integral is evaluated over the velocity limits of the observed line width (see table 3.1). The uncertainty in I_{CO} was calculated from the RMS uncertainty in the temperature integrated over the line width for each pointing. The telescope calibration is expected to provide an additional uncertainty of 10-20 % (not reflected in the uncertainties quoted in table 3.1). The CO J=1-0 intensities were converted into an H_2 mass, $M(H_2)$, using several assumptions discussed below.

The relationship between CO and H_2 is described by the CO/H_2 conversion factor, X_{CO}. Since H_2 is not easily detected, another, more accessible molecule must be used as a tracer in order to measure the H_2 indirectly. The ^{12}CO molecule has several rotational transitions which emit radiation at radio wavelengths and are observable through the atmosphere on Earth. X_{CO} translates the integrated CO intensity into an H_2 column density. Clearly, the accuracy of the conversion factor is essential in order to accurately measure $M(H_2)$.

The X_{CO} value of $2.3 \pm 0.3 \times 10^{20}$ molecules/cm^2/(K kms^{-1}), used here, is taken from Strong et al. (1988) who obtain it using CO J=1-0 data from all sources in the galactic

plane of the Milky Way with galactic latitude ranging from $-7°$ to $+7°$ and diffuse galactic γ-ray measurements.

Diffuse γ-ray emission from the ISM is expected from cosmic ray interaction with Hydrogen atoms. The diffuse γ-ray intensity, I_γ, is related to the emissivity, ϵ_γ, and the number of hydrogen atoms, from both atomic and molecular hydrogen, and is expressed as:

$$I_\gamma = \varepsilon_\gamma \{N(HI) + 2X_{CO}I_{CO}\} \qquad (cm^{-2}sr^{-1}s^{-1}) \qquad (3.2)$$

Since I_{CO} is measured directly and N(HI) is obtained independently from 21 cm emission, the γ-ray data place strict constraints on X_{CO} for the Milky Way (Strong et $al.$, 1988, Bloemen, 1989). The conversion factor most likely depends on the metallicity of the individual galaxy's ISM (e.g. Wilson, 1994, 1995, Taylor et $al.$, 1998), however, there is little evidence to suggest that the metallicity of NGC 5866 and that of the Milky Way is very different. Metallicity is proportional to galactic luminosity (Bothun et $al.$, 1984 use M_H data, Bica & Alloin, 1987 use M_B) and the absolute visual magnitudes of NGC 5866 and the Milky Way are quite close: -21.0 and -20.9, respectively (Hamabe et $al.$, 1979, and van den Bergh, 2000, respectively), although the value for the Milky Way is uncertain. Although more work is needed to truly verify the metallicity of NGC 5866, the conversion factor of NGC 5866 is assumed to be the same as that of the Milky Way.

This work assumes a distance of 15.3 Mpc to NGC 5866 (Tully, 1988), in order to be consistent with the data reduction of the rest of the S0 survey members. Estimates for the distance to NGC 5866 vary wildly in the literature (anywhere from 11-25 Mpc) and the

accuracy of many of the results presented here are sensitive to the distance used. For example, small changes in the assumed distance create large differences in the computed H_2 masses, since it is proportional to the distance squared (see equation 3.3).

The remaining parameters used to derive $M(H_2)$ are obtained directly; one then has:

$$M(H_2) = 4.267 \times 10^{-19} \theta^2 D^2 \alpha X_{CO} I_{CO} \quad (M_\odot) \tag{3.3}$$

where D is the assumed distance in Mpc (15.3 Mpc), θ is the FWHM of the telescope beam in arcseconds (20.9" for J=1-0), and α is the ratio between the CO/H_2 conversion factor in NGC 5866 and the Milky Way (α=1). Table 3.1 gives the integrated CO intensities for both transitions and the H_2 masses for each pointing. Because the telescope was moved about one half the full width half maximum (FWHM) in the J=1-0 transition between observations, the total H_2 mass for NGC 5866 was found by adding every second pointing along the major axis. The mass was calculated a second time using the remaining pointings. Table 3.1 groups the pointings in the way they used to obtain the two estimates for $M(H_2)$. The results were averaged to give

$$M(H_2) = 4.55 \pm 0.43 \times 10^8 \, M_\odot \tag{3.4}$$

Table 3.1 The H_2 mass results. The $M(H_2)$ values were obtained using equation 3.4. Table 3.2 lists molecular mass values found by other workers for comparison.

offset (")	line window (km s^{-1})	I$_{CO}$ (1-0) (K km s^{-1})	H$_2$ mass (10^7 M$\odot$)	total H$_2$ mass (10^8 M$\odot$)
(1)	(2)	(3)	(4)	(5)
-35, 27	479-606	0.3116 ± 0.80	0.313 ± 0.80	
-17, 14	460-645	5.404 ± 1.18	5.42 ± 1.18	
0, 0	440-1100	22.016 ± 3.41	22.1 ± 3.43	4.32 ± 0.47
17, -14	715-1050	13.831 ± 2.32	13.9 ± 2.33	
35, -27	866-1100	1.5252 ± 1.58	1.53 ± 1.58	
-26, 20	479-606	2.105 ± 0.83	2.11 ± 0.83	
-9, 7	440-760	12.557 ± 2.09	12.6 ± 2.10	4.78 ± 0.39
9, -7	475-1140	26.708 ± 2.87	26.8 ± 2.88	
26, -20	815-1045	6.2609 ± 1.31	6.28 ± 1.32	

Avg. H$_2$ mass:	4.55 ± 0.43

col. (1) gives the RA and Dec offsets in arcseconds, respectively, col. (2) gives the velocity limits used in equation 3.1, col. (3) is the observed intensity from equation 3.1, col. (4) gives the calculated $M(H_2)$ from each pointing and col. (5) gives the total $M(H_2)$ value from the two groups of pointings and at the bottom, the average of both totals.

3.1.2 The Molecular to Atomic Hydrogen Gas Ratio

The molecular to atomic gas mass ratio, M_{H2}/M_{HI}, in galaxies is often used as a statistical measure against other galaxies of the same type or to compare against other morphological types. This information can be used to explore theories of interaction, gas evolution and environment as all of these factors affect the mass ratio. Previous studies have shown that early-type galaxies often have higher M_{H2}/M_{HI} values than do later types (Casoli et al., 1998). The average molecular to atomic hydrogen mass ratio in S0s is ~0.4

(Casoli *et al.*, 1998) while later types (Sa-Sd) have mass ratio values ~0.3 (Casoli *et al.*, 1998). The samples of Casoli *et al.* (1998) include members of the Virgo and Coma clusters among others. From a volume limited sample of Sa-Sd galaxies, the median value of M_{H2}/M_{HI} = 0.15 (Sage, 1993). Many S0 galaxies are found in dense clusters of galaxies and owe their high M_{H2}/M_{HI} values to interaction or ram pressure stripping of the HI gas. The M_{H2}/M_{HI} ratio in NGC 5866 can be used as a clue as to how its environment might have affected it.

Since no HI has been detected in NGC 5866, the HI mass upper limit, M_{HI}, was calculated from HI flux upper limit of Knapp & Gunn (1982) and equation 3.5. Equation 3.6 (from Haynes & Giovanelli, 1984) assumes that the HI is optically thin and is written as:

$$M_{HI} = 2.36 \times 10^5 D^2 S \Delta V \quad (M_\odot) \tag{3.5}$$

where $S = 6 \times 10^{-3}$ Jy is the observed HI flux in Janskys (Jy), 1 Jy = 10^{-26} Wm^{-2}Hz^{-1}, D is the distance in Mpc and ΔV in the line width in kms^{-1}.

The HI mass was calculated using a line width of 406 kms^{-1} from the stellar and ionized gas rotation curves of Fisher (1997) for NGC 5866 and also a line width of 610 kms^{-1} from the CO data presented here. The results were found to be,

$$M_{HI} < 1.3 \times 10^8 \, M_\odot \, (\Delta V = 406 \, kms^{-1}) \tag{3.6}$$

$$M_{HI} < 2.0 \times 10^8 \, M_\odot \, (\Delta V = 610 \, kms^{-1}) \tag{3.7}$$

Table 3.2 lists the various values of $M(H_2)$ found for NGC 5866 along with the M_{H2}/M_{HI} values calculated using the H2 masses listed in column 1 and the HI mass values from

equations 3.6 and 3.7. From table 3.2, $M_{H2}/M_{HI} \geq 3.5$ for NGC 5866 contrasts with the average value of ~0.4 as found by Casoli *et al.* (1998) for the average value from a sample of 7 S0 galaxies and 20 S0-a galaxies. Such large M_{H2}/M_{HI} ratios are not unprecedented. However, those are mostly seen in cluster environments where significant interaction is taking place (e.g. NGC 4710, in the Virgo cluster, has a M_{H2}/M_{HI} of ~30 (Wrobel & Kenney, 1992)). It should be repeated that NGC 5866 is most likely a member of the NGC 5907 loose group of galaxies and that NGC 5907 shows several signs of interaction. The topic of previous interaction in the NGC 5907 group will be explored in chapter 4.

Table 3.2 H_2 masses for NGC 5866, scaled to a distance of 15.3 Mpc, from this work and the literature. The H_2/HI mass ratio lower limits are also given from the 2 HI upper limits shown in equations 3.6 and 3.7

H_2 mass 10^8 M☉ (1)	M_{H2}/M_{HI} (2)
4.55 ± 0.43	≥2.3 - 3.5
0.877[a]	≥0.43 - 0.67
6.19[b]	≥3.1 - 4.8
1.31[c]	≥0.66 - 1.0
3.74[d]	≥1.9 – 2.9

a.Wiklind & Henkel (1989), b.Thronson *et al.* (1989), c.Taniguchi *et al.* (1994), d.Young *et al.* (1995). Col. (1) the H_2 mass from CO measurements scaled to 15.3 Mpc. The varying results reflect different beam sizes and number of pointings used by the various authors. Also, Thronson *et al.* (1989) use different assumptions about the CO/H_2 conversion factor. Col. (2) the range of molecular gas to atomic gas mass ratios from the largest and smallest derived HI gas masses, $M_{HI} < 1.3 \times 10^8$ M☉ and $< 2.0 \times 10^8$ M☉ (flux from Knapp & Gunn (1982) and line widths of 406 kms⁻¹ and 610 kms⁻¹, respectively).

3.1.3 The Gas to Dust Ratio

The gas to dust ratio is an important quantity since dust is required for the formation of H_2 and other molecules. The dust content determines the metallicity of both the ISM and the stars which form from it. The mass of the dust in a galaxy can be inferred from its FIR emission. The dust mass in NGC 5866 was found by using equation 3.8, taken from Thronson et al. (1989) as adapted from Thronson & Telesco (1986) which assumes an opacity of 25 cm^2g^{-1} at 100 μm:

$$M_{dust} = 5D^2 F_{100}[\exp(144/T_d) - 1] \quad (M_\odot)$$

(3.8)

where the distance, D is in Mpc, F_{100} is the IRAS 100 μm flux in Jy (16.1 Jy from the IRAS Faint Source Catalogue) and T_d is the dust temperature in K (30 K from Thronson et al., 1989). From equation 3.8,

$$M_{dust} = 2.3 \times 10^6 \ M_\odot$$

(3.9)

which implies $200 \lesssim M_{gas}/M_{dust} \lesssim 300$, where M_{gas} is the mass of the molecular and the atomic Hydrogen. The lower and upper limits are calculated based on the HI mass limits found in section 3.1.2. The gas to dust mass ratio in NGC 5866 is 2-4 times lower than the average value of ~800 which Thronson et al. (1989) give for S0 galaxies with only HI upper limits. That could imply either a deficiency of hydrogen or an overabundance of dust in NGC 5866 compared to similar galaxies. However, it could also be a temperature effect. The gas to dust ratio is found to be ~800 by assuming the temperature of the gas is 38 K instead of 30 K. Thronson et al. caution that the temperature they quote is not an accurate physical temperature but is a measure of the relative abundance of ISM components. The fact that the temperature is so uncertain and that the dust mass equation

is extremely sensitive to the dust temperature used, the gas to dust ratio in NGC 5866 could be considered average within a large uncertainty range.

3.1.4 The Current Star Formation Rate

The central questions of this work are: Where did the gas come from, and where is it going? The second question is addressed in this section. The most obvious mechanism of gas depletion is star formation.

The star formation rate (SFR) of a galaxy can be calculated from its far infrared (FIR) emission. Following Thronson *et al.* (1989), FIR emission is defined as $40\mu m$-$125\mu m$ radiation, unless otherwise stated. In normal galaxies FIR radiation is primarily the result of dust grains which have been heated by massive, newly formed stars. That energy is then re-emitted at longer wavelengths. Consequently, the amount of FIR radiation, can be used to measure how many new stars per unit time are forming in the galaxy with an assumed initial mass function, which we will call SFR_{FIR}. Ionized gas observations in NGC 5866 show that the HII regions are limited to the dust lane so it is a safe assumption that the FIR star formation rate will not be underestimated due to any star formation occurring outside of the dust shroud. The result is an upper limit, however, since stars of all ages actually contribute to heating all forms of dust in the galaxy, producing a global FIR flux. Diffuse dust clouds in galaxies are not associated with any star forming regions, but are heated by the general stellar radiation field and also contribute to the overall FIR luminosity.

All star formation rate calculations depend on the choice of initial mass function (IMF) since the number of stars which can contribute to the heating of the dust is important. The IMF gives the relative number of objects of different mass found in a specific volume of space. In other words, it tells us how many high mass and how many low mass stars are formed from a certain clump of gas. The IMF can be approximated mathematically as:

$$dN = N_o \xi(M) dM \qquad (3.10)$$

where N_0 is a normalizing constant. Equation 3.10 gives the number of stars, dN, between mass M and M+dM where $\xi(M)$ is the frequency of creation of a given stellar mass. The Salpeter IMF (Salpeter, 1955) is derived when using a simple power law for the frequency, shown in equation 3.11.

$$\xi(M) \propto M^{-2.35} \qquad (3.11)$$

The Salpeter IMF is only one of many derived from theory and observations. It is perhaps the simplest since it employs a single power law over all masses. Other IMFs use different power laws for different mass ranges (e.g. Miller & Scalo, 1979). Since different initial mass functions predict different amounts of OB stars, the star formation rate is sensitively dependent on the choice of IMF.

The value of SFR_{FIR} can be found from the far infrared luminosity by making three major assumptions. The first is the average mass to (bolometric) luminosity ratio of a star forming cluster and the second is the time scale on which this cluster produces stars that would heat the surrounding dust. The average mass to luminosity ratio, $\overline{M}/\overline{L}$, is formed using the average stellar mass from an assumed IMF, in this case, the Salpeter

IMF. That is divided by the bolometric luminosity of a star of average mass, found using an assumed luminosity function. Following Thronson & Telesco (1986), values of the luminosity function are taken from table 5 in Telesco & Gatley (1984). The third assumption is that the dust is optically thick to all wavelengths other than FIR, and so its resulting FIR luminosity is essentially the same as the bolometric luminosity of the stars. The star formation rate is therefore written as,

$$SFR_{FIR} = \frac{L_{FIR}}{t_{FIR}} \frac{\overline{M}}{\overline{L}} \quad (\text{M}\odot/\text{yr}) \tag{3.12}$$

where t_{FIR} is the time scale for which young stars heat the dust and L_{FIR} is the FIR luminosity in solar units. The value of t_{FIR} is estimated to be $\sim2 \times 10^6$ years from observations and theory (Thronson & Telesco, 1986), whereas $\overline{M}\big/\overline{L}$ equals 1.3×10^{-3} M$\odot$/L$\odot$ assuming a Salpeter IMF in the range of 0.1 to 100 M$\odot$ and the luminosity function of Telesco & Gatley (1984). Combining these quantities gives:

$$SFR_{FIR} = 6.5 \times 10^{-10} L_{FIR} \quad (\text{M}\odot/\text{yr}) \tag{3.13}$$

The quantity, L_{FIR}, is found from:

$$L_{FIR} = 5.6 \times 10^5 D^2 [2.58 F_{60} + F_{100}] \quad (\text{L}\odot) \tag{3.14}$$

where F_{100} and F_{60} are the IRAS fluxes at 100 and 60 micrometers (16.1 Jy and 4.88 Jy, respectively, from the IRAS Faint Source Catalogue). Equation 3.14 is based on fitting the FIR flux from two wavelengths to a modified black body spectrum incorporating a dust emissivity proportional to v^α, i.e. $F_v \propto vB_v(T_d)$, typically, $\alpha = 1$. From equation

3.14, $L_{FIR} = 3.8 \times 10^9$ Lo and putting this value into equations 3.13 gives a star formation rate of

$$SFR_{FIR} = 2.4 \text{ Mo/yr} \qquad (3.15)$$

for NGC 5866.

The nature of the time scale, t_{FIR}, is not agreed upon by all authors. Some view the physical interpretation as the time scale on which young OB stars destroy the surrounding medium, while others view it as the time scale on which the starburst takes place (Kennicutt, 1998a). Kennicutt (1998a) uses the mean luminosity and mass of a starburst region ($\sim 1.3 \times 10^8$ Lo and 10^6 Mo, respectively) given by the models of Leitherer & Heckman (1995) for starburst activity lasting between 10-100 Myr. This time scale is 2 orders of magnitude larger than that of Thronson & Telesco (1986). Writing SFR in the same form and under the same IMF assumptions as equation 3.13, gives:

$$SFR_{FIR} = 1.73 \times 10^{-10} L_{FIR} \quad \text{(Mo/yr)} \qquad (3.16)$$

again with L_{FIR} in Lo , however, this time defined as emission at wavelengths between 8-1000 μm. The far infrared luminosity as defined above was found using equation 3.17,

$$L_{FIR} = 391484 D^2 C(T_d)[2.58 F_{60} + F_{100}] \quad \text{(Lo)} \qquad (3.17)$$

where D is the distance in Mpc, F_{100} and F_{60} are the IRAS fluxes at 100 and 60 μm, respectively (same as above) and $C(T_d) = 1.648$ (Helou et al., 1988) is a constant based on the fraction of blackbody radiation with wavelengths between 1-1000 μm which is seen by the IRAS filters. This wavelength range for FIR is assumed to be consistent with 8-1000 μm. This gives $L_{FIR} = 4.3 \times 10^9$ Lo, a slightly larger value than that derived from equation 3.15. This is a reflection of the larger wavelength range included here. Using

this definition of L_{FIR} and equation 3.17, the star formation rate found from the far infrared luminosity is

$$SFR_{FIR} = 0.75 \ M_{\odot}/yr \tag{3.18}$$

Clearly, the choice of IMF, the uncertain nature and value of t_{FIR}, and the assumption of a large optical depth for the dust imply that these equations provide only rough estimates of the true SFR.

3.1.5 The Hα Star Formation Rate

Another measure of the star formation rate in external galaxies is their Hα luminosity, $L_{H\alpha}$. Hα emission results from HII regions around hot young stars, and is produced by a recombination of Hydrogen to the first excited level. The electron quickly drops to a lower energy level before the atom is re-ionized by high energy UV photons. The value of $SFR_{H\alpha}$ is a lower limit to the actual star formation rate, because dust in the external galaxy and the Milky Way absorbs Hα photons and reduces the flux received on Earth. The Hα luminosity used here has been corrected for foreground extinction. However, the intrinsic extinction from NGC 5866 has not been corrected for, and the contribution to the measured flux due to the [N II] ($\lambda = 6548$ Å and 6583 Å) lines needs to be removed. Shields (1991) assumes an [N II]/Hα ratio of 1.38 for the contribution of [N II] to the total flux. This value is uncertain (5-10%) and is not specific to NGC 5866 (Shields, 1991). Using the Salpeter IMF, the star formation rate via the Hα luminosity, $L_{H\alpha}$, is:

$$SFR_{H\alpha} = 3.04 \times 10^{-8} L_{H\alpha} \quad (M_{\odot}/yr) \tag{3.19}$$

adapted from Kennicutt (1998b) where $L_{H\alpha}$ is in solar units and the Hα star formation rate

is in solar masses per year. Using the largest measurement (717.7 pc in diameter at 15.3

Mpc) from Shields (1991), $L_{H\alpha} = 8.13 \times 10^5$ L$_\odot$,and scaling to a distance of 15.3 Mpc,

the star formation rate is found to be

$$SFR_{H\alpha} = 0.025 \text{ M}_\odot/\text{yr} \qquad (3.20)$$

Using the upper limit, $L_{H\alpha} < 1.54 \times 10^6$ L$_\odot$ from Shields' (1991) largest aperture

observation (1.44 kpc in diameter at 15.3 Mpc), the value could be as high as

$$SFR_{H\alpha} = 0.047 \text{ M}_\odot/\text{yr} \qquad (3.21)$$

These values are on the order of 10 times smaller than SFR_{FIR} from equation 3.16. This

is a reflection of the fact that the $SFR_{H\alpha}$ of equation 3.19 makes no correction for intrinsic

extinction and assumes that all UV photons are absorbed by the HII gas. Also, the

apertures do not see as much emission due to their small sizes. Given the large

uncertainties, it is not surprising that these values appear to be so different. Indeed, many

workers have found higher star formation rates from FIR data than from Hα (e.g.

Hopkins et al., 2001). The FIR luminosity has an unknown fraction of its flux not related

to star formation while the observed Hα flux is most certainly lower than the actual flux

due to reasons mentioned above.

3.1.6 The Gas Consumption Timescale

The star formation efficiency (SFE) is another useful quantity to answer the question of

where is the gas going. The SFE is a measure of how much gas is being used up forming

stars relative to the amount of gas available. Following Thronson & Telesco (1986) the

SFE can be expressed in terms of what fraction of the molecular gas is being turned into stars in a given year.

$$SFE = \frac{SFR}{M(H_2)} \quad (yr^{-1}) \qquad (3.22)$$

When using the SFR$_{FIR}$ of equation 3.15, the star formation efficiency is

$$SFE = 5.3 \times 10^{-9} \ yr^{-1} \qquad (3.23)$$

Thus, by taking the inverse of this result, the present star formation rate can be maintained for $\sim 2 \times 10^8$ years. This is only a small fraction of the age of the universe so, assuming a constant star formation rate, the gas must be replenished from some source in order to be seen today. Using the Kennicutt (1998a) SFR$_{FIR}$ from equation 3.18, the star formation efficiency becomes,

$$SFE = 1.44 \times 10^{-9} \ yr^{-1} \qquad (3.24)$$

This rate can be maintained for approximately 7×10^8 years, still a short length of time on cosmological scales. The lowest star formation rate is given by the Hα data and reveals a star formation efficiency of

$$SFE = 5.5 \times 10^{-11} \ yr^{-1} \qquad (3.25)$$

showing that star formation can continue at the present rate for ~ 18 Gyrs. Using the Hα flux upper limit formation rate gives a star formation efficiency of

$$SFE = 1.0 \times 10^{-10} \ yr^{-1} \qquad (3.26)$$

which means star formation can continue on the order of 10 Gyr. However, these gas consumption time scales are lower limits since no replenishment of the ISM has been considered.

The mass return rate, as calculated from Faber & Gallagher (1976) for NGC 5866 is 0.10

M⊙/yr. This is ~25 times less than the largest star formation rate from the far infrared

data. Assuming the higher star formation rate, it would seem that NGC 5866 will

consume its gas supply on the order of 10^8 yrs while it would take ~6 Gyr to replenish

$4.55 \pm 0.43 \times 10^8$ M⊙ of H_2 from simple mass return arguments. This suggests that the

star formation rate might oscillate on time scales on the order of several billion years. A

common measure of how the current star formation rate compares to the average past

SFR is the ratio, L_{FIR}/L_B (e.g. Wiklind & Henkel, 1990). This assumes that the blue

luminosity, L_B, is proportional to the star formation rate averaged over the last 10^9 years

i.e. that L_B is associated with lower mass stars than those responsible for most of the far

infrared emission (Thronson & Telesco, 1986, references therein). For NGC 5866,

$$L_{FIR}/L_B = 0.22 \tag{3.27}$$

using L_B from Tully (1988). The L_{FIR}/L_B value found here is roughly half the average

value of ~0.40 found for normal spiral galaxies and ~0.35 found for S0s (de Jong *et al.*,

1984). The low value of L_{FIR}/L_B implies that the star formation rate of NGC 5866 was

higher in the past if we assume that the SFR has been roughly constant over time in

normal spirals.

If either of the Hα star formation rates is correct then NGC 5866 is roughly in mass

balance since the present star formation rate can be maintained over a Hubble time.

Given the large uncertainties in the SFR calculations, the upper limit star formation rate

from the Hα data of 0.047 M⊙/yr will be used. This is a compromise between the upper

limits set by the far infrared data, which is believed to be the least accurate of the two

measures, and the lowest value from the Hα data. A simple calculation shows that the total cool ISM mass should be 5.3×10^8 M$\odot$. This is found by subtracting the total mass consumed by star formation in 10 Gyr from the total mass returned in the same time. The result is on the order of 6.4×10^8 M$\odot$ found by scaling up the molecular hydrogen mass to include Helium.

3.2 Morphology and Kinematics of the Molecular Gas

A computer model was used to help answer questions regarding the morphology and kinematics of the molecular gas in NGC 5866. COSPEC is a FORTRAN program used to simulate observed ^{12}CO line spectra. COSPEC models an infinitely thin rotating disk or ring of optically thick ^{12}CO. When discussing the models in general, the term "disk" is used since a ring is simply a special case of a disk in COSPEC. The disk can be of any angular size and rings of any angular radius. The model can be viewed at any inclination on the sky and at any angle to the major axis. The CO can be distributed in a choice of several different intensity profiles: constant intensity disk or ring, Gaussian disk or ring, exponential disk or truncated Gaussian ring. The disk models have their maximum intensity values at the centre. The model rotates as prescribed by a user defined rotation curve. The model allows the user to synthesize the complex structure in an observed spectrum by introducing co-moving regions of either lower or higher intensity into the chosen intensity profile. These "clouds" are transparent to one another so that no shadowing takes place. The code does not constrain the absolute physical cloud properties but does allow one to gauge roughly where they could be found in physical space and also suggests what their size and relative brightness might be. The program

also allows for the inclusion of a velocity dispersion component to any model. The velocity dispersion is incorporated using a Monte-Carlo simulation of an assumed Gaussian velocity distribution (Box-Mueller algorithm, Bevington & Robinson, 1992). The simulated spectra and the observations are plotted together for visual inspection and a "goodness of fit" value is calculated by summing the squares of the intensity differences in each velocity bin over the observed line.

For this project, the convolving beam is an approximation of the IRAM 30m power pattern for the J=1-0 CO transition (Greve *et al.*, 1998). The central pointing in the model (3" offset in this case) is normalized to the 0,0 pointing data. The model offset is 3" as opposed to zero, when simulating the 0,0 pointing, in order to best reproduce the centre pointing without complicating the model. 3" is considered to be within the uncertainty of the telescope pointing. The scale factor needed to equalize the model and the integrated intensities at this pointing is used for all other pointings. The source code is presented in appendix A and further details of the parameters and how the code was used in this work can be found in appendix B. In this work, the term "best fit model" refers to the model which best reproduced the observed spectra based on the goodness of fit parameter.

3.2.1   The Distribution of Molecular Gas in NGC 5866

The gas was best modelled by a Gaussian ring distribution with an outer radius of 30" seen edge-on. This is about the observed length of the optical dust lane in NGC 5866. The intensity peaked at a radius of 15", with a FWHM of 15". Several asymmetries or

"hot" and "cold" spots (called clouds and holes, respectively henceforth) were included to better fit the observed spectra. A unique distribution of asymmetries cannot be found based on the limited nature of the data, but clearly there are regions of greater intensity on the redshifted side relative to the blueshifted side. Table 3.3 lists the asymmetry parameters. There are several large regions of depressed intensity (~3-6" in diameter) located mostly at the same radius as the centre of the Gaussian ring. The necessity of these holes to improve the model argues for a broken ring structure for the molecular gas distribution. This is a common form of gas distribution in galaxies (Pogge & Eskridge, 1987). Most notably, the lenticular galaxy, NGC 404, has its molecular gas distributed in a ring with several pieces missing (Wiklind & Henkel, 1990). The areas of higher intensity are possibly giant molecular clouds warmed by the light from recently formed stars. The brighter clouds introduced in the model are on the order of 200 pc in size and make up only ~4% of the intensity output. This corresponds to a cloud mass of ~10^6 M$\odot$. These clouds are comparable in size and mass to the larger the giant molecular clouds in the Milky Way (Dame *et al.*, 2001). Figure 3.1 shows a diagram of how the holes and clouds are distributed in the model disk. Table 3.3 lists the parameters used in the best fit model.

The models were judged on the basis of how well they could synthesize the 4 central pointings (offsets seen in figures 3.5-3.8). The 4 central pointings show the strongest signal and have unique spectral shapes. The shapes of the outer pointings basically preserve the saw tooth pattern and so no new complications to the model are needed to synthesize these pointings. Figures 3.2 through 3.10 show the simulated spectra of the

best fit model, plotted with the data for comparison. The best model was found by first finding a rotation curve which could match the observed line width qualitatively. To begin, published stellar and ionized gas rotation curves for NGC 5866 (Fisher, 1997) were attempted, but failed to provide a reasonable fit. Section 3.2.2 discusses the Fisher (1997) data further. With the chosen rotation curve, several different intensity profiles where modelled starting with a simple constant intensity disk and on through the various distributions mentioned above (see appendix C for details and results of these experiments). A Gaussian ring (described above) was chosen as best based on the goodness of fit parameter and several asymmetries were included in order to match the spectra (table 3.3). Details on the parameter choosing process can be found in appendices B and C. For example, the Gaussian ring model without asymmetries is compared to the best fitting Gaussian disk (FWHM = 45") model in figures 3.11-3.14. The goodness of fit parameter is slightly lower at 0.224 for the Gaussian ring as opposed to that of the Gaussian disk, 0.238. The main benefit of a ring model over a disk is clear in figure 3.12. The goodness parameter is ~30% lower in the ring model. The low observed power around the systemic velocity of 745 kms^{-1} favours distributions with less power near the centre. The saw tooth pointings (figures 3.11, 3.14) are basically the same for both models. This is not surprising since the outer edge of a ring and a disk look basically the same. Also, for comparison, figures 3.15-3.18 show how the asymmetries improve the plain Gaussian ring model. The average goodness of fit parameter drops to 0.200 from 0.224, an improvement of ~10%. The asymmetries are most obvious in figure 3.16. The model still contains too much power in the centre but matches the shape of the spectra more closely. The plain Gaussian ring model provides too much power at the peak of the

saw tooth pointings, however the addition of several "holes" was effective at lowering the

peaks (figures 3.15, 3.18). The asymmetries also helped to flatten out the peak seen in

figure 3.17, and although, still too powerful, the best fit model is a closer match the shape

of the spectrum.
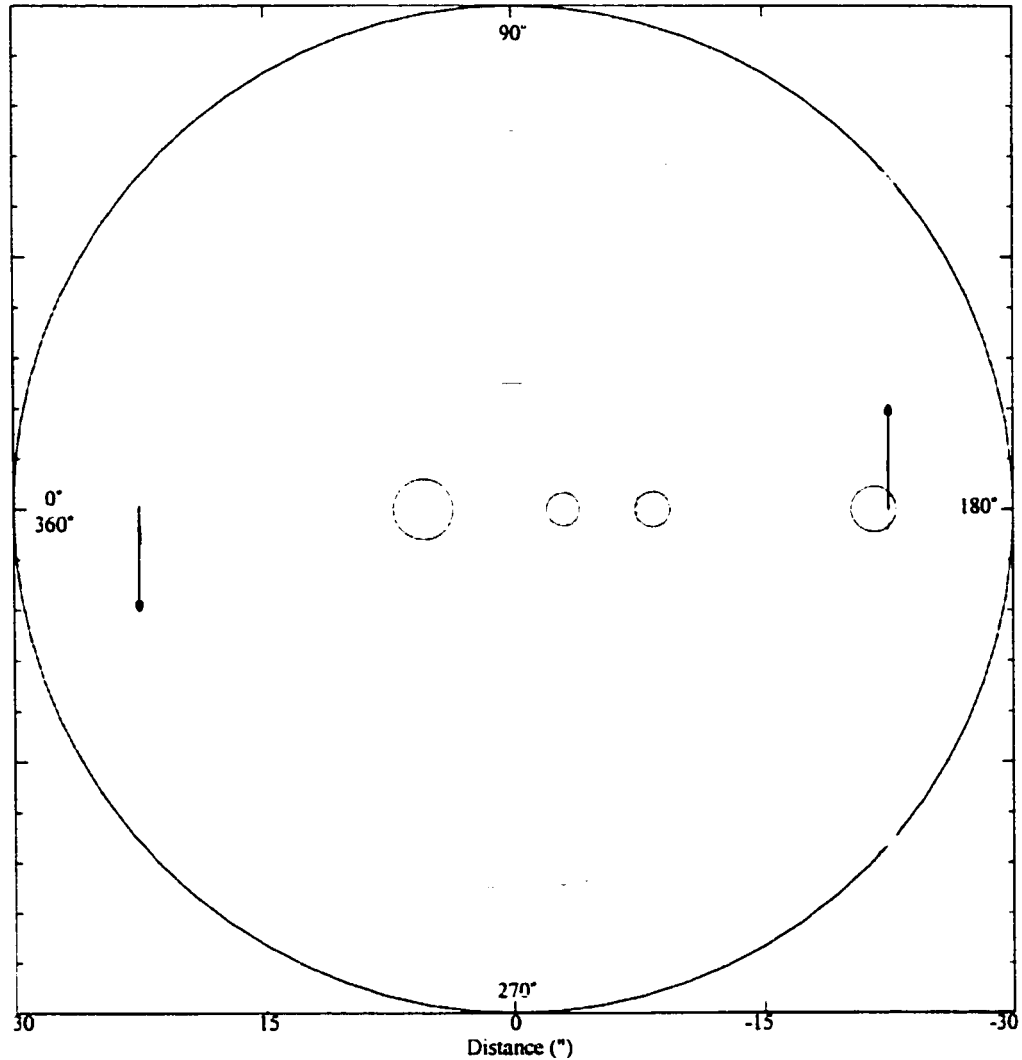
Figure 3.1 A schematic of the best fit model viewed face on (parameters used in this model are found in table 3.3). The azimuth of the cardinal locations is shown on the diagram. The arrows indicate the direction of rotation. The offsets for the convolving beam can be surmised from the distances listed on the bottom. The green circles locate the FWHM of the Gaussian ring. Blue circles represent the holes added to the model and the red circles represent the clouds incorporated into the model. The line of sight is perpendicular to the plane of the page looking from the bottom to the top.

Table 3.3 This table lists all of the parameters necessary to generate the COSPEC model which best matched the data. The results of this model are presented in the box at the bottom of the table. Figure 3.1 illustrates the geometrical quantities.

			pointing	offset (code)	CLASS RMS
systemic velocity (kms⁻¹)	745		pointing	offset (code)	CLASS RMS
			(")	(")	(K)
max. rotational velocity (kms⁻¹)	305				
Transition	J=1-0		0,0	3	5.17E-03
disk size (")	60		-9,7	14	6.53E-03
kink vel. in rot. curve (kms⁻¹)	200		9,-7	-8	4.32E-03
kink radius in rot. curve (")	10		17,-14	-19	6.92E-03
tip (degrees)	90				

cloud #	rad. position (frac. Of disk)	Azimuth (degrees)	Intensity (scalar)	Size (")	Size (cu)
1	0.5	91	0	3	10
2	0.5	79	0	3	10
3	0.18	0	2	3.6	12
4	0.1	180	2	1.98	6.6
5	0.28	180	7	2.1	7
6	0.72	180	3	2.7	9
7	0.9	139	0	6	20
8	0.9	221	0	6	20
9	0.5	139	0	2.7	9
10	0.5	221	0	2.7	9

mod. type	norm.co	ring rad. (")	FWHM frac. Disk	pointing (")	RESULTS Goodness	avg. good
gauss ring	2.54952E-04	15	0.25	0,0	0.168	0.200
				-9,7	0.239	
				9,-7	0.322	
				17,-14	0.078	

This table is presented in order to give the reader the full set of parameters needed to generate the best fit model. The units used above match those referred to in the code unless otherwise stated here. The upper left portion of the table lists the basic parameters of the rotation curve and disk. The term "size" refers to diameter. The "kink" velocity and radius refer to the location on the rotation curve where there is a change in regime. Essentially, the rotation curve rises to 200 kms⁻¹ at 10" and then continue to rise to the maximum rotational velocity (305 kms⁻¹) at the edge of the disk (30"). The term "tip" is the program name for the inclination of the disk (see appendix B for a detailed description of the COSPEC parameters). Since NGC 5866 is an edge on galaxy, the model uses an inclination of 90° to best simulate the data. Directly below the tip parameter is a list of the asymmetry parameters. These include the radial position, azimuth, intensity and size. Size is listed twice, once in " and once in computer units, cu. To run the code, the clouds sizes are input in cus. Figure 3.1 shows the asymmetries pictorially. Below the cloud parameters are the specific values of the Gaussian ring parameters. The upper right hand corner of the table lists how the telescope offsets and the COSPEC offsets match up along with the RMS uncertainty in the intensities as found by the CLASS data reduction software. These values are needed for computing the goodness of fit.

Looking at the best fit model again, the 9",-7" pointing (figure 3.7) is clearly the worst fit of the 4 central pointings. The excess power between 440-750 kms^{-1} could not be simulated with this simple model. It might represent molecular gas with distinct kinematics or an error in pointing. The latter seems unlikely since the 0,0 pointing data (figure 3.6) also show excessive power on the redshifted side, arguing that this is a real effect. Attempts to model the 9,-7 pointing by choosing offsets closer to the centre only slightly improved the fit (~6%) at an offset of −6" (as opposed to −8"). Offsets closer to 0" gave progressively worse fits overall but did fit the blueshifted side better between 475 and 745 kms^{-1}. Another strange feature of the 9,-7 pointing is the extra power found in the 945-1140 kms^{-1} bins. This looks like it could be an effect of velocity dispersion since it seems to be smoothing out the peak. Models with an adopted velocity dispersion matched this pointing slightly better in the 945-1140 kms^{-1} velocity bins since velocity dispersion necessarily adds power above the highest velocity given by the rotation curve (and also below the lowest velocity), figure 3.21 shows this effect. The other major difficulty with the model is the excess power seen at the peaks of both of the "saw tooth" spectra seen in figures 3.5 and 3.8. This could be reconciled by adding more holes to the model or requiring that the intensity drop off faster at larger radii. Indeed, Gaussian ring models with smaller FWHM do fit the saw tooth spectra better, but are worse on the whole. The simulated spectrum for the −26",20" offset (figure 3.3) has power too blueshifted compared to the data by about 50 kms^{-1}. This might means that the rotation curve drops back to a slightly lower velocity near the observed radius. However, the corresponding redshifted signal (figure 3.9) does not imply a drop in the rotation curve. This is might be due to the slight systematic shift in offsets between to the model and the

pointings (3"), which was necessary to best model the 4 central pointings. Figure 3.10

might be consistent with slightly reduced rotational speeds, but the signal is too faint to

provide compelling evidence.
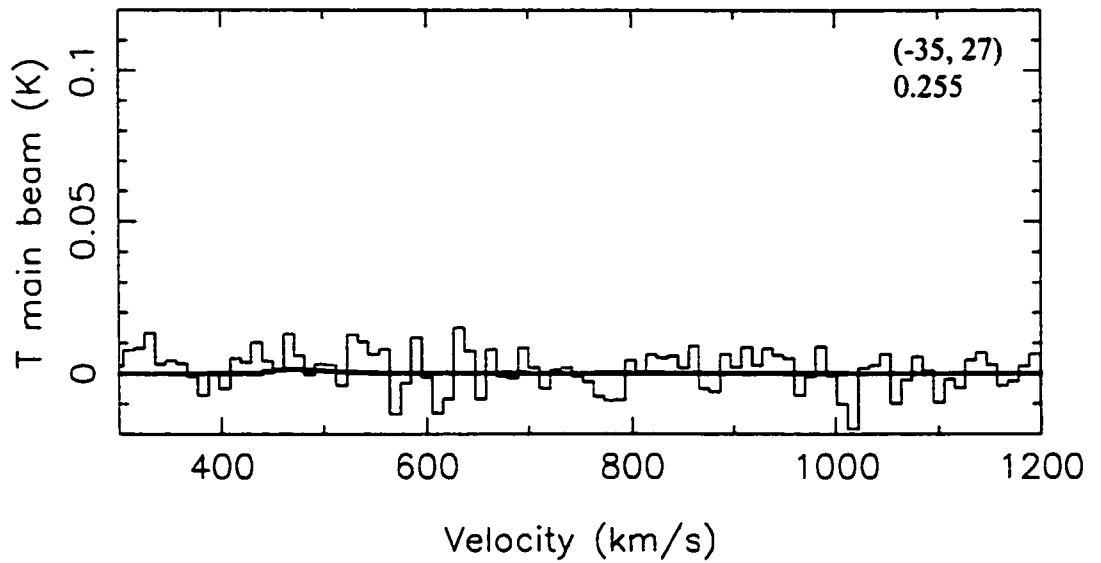
Figure 3.2   This and the following eight figures show how the best fitting model compares to the observations.   The darker line is the Gaussian ring model with asymmetries (ring radius = 15", FWHM = 15") plotted with the data (thin, noisy line). The model offset is 47".   The parameters used to generate this and the other spectra in figures 3.2 through 3.10 are found in table 3.3.   The telescope pointing offset in arcseconds and "the goodness of fit" of the model to the data is recorded in the upper right hand corner of the chart box.
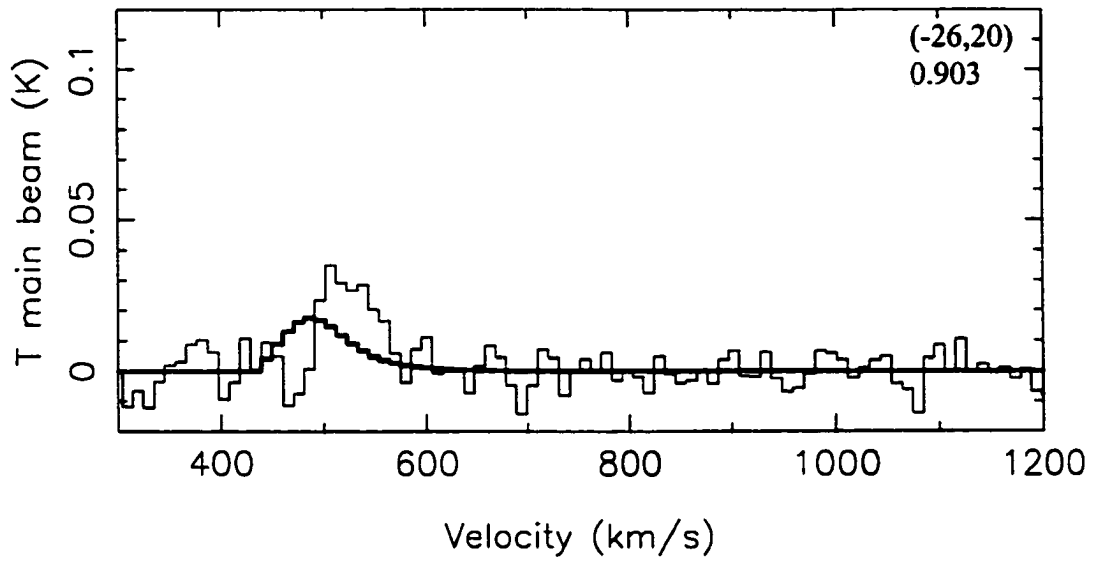
Figure 3.3 Same as Figure 3.2 except the model offset is 36".
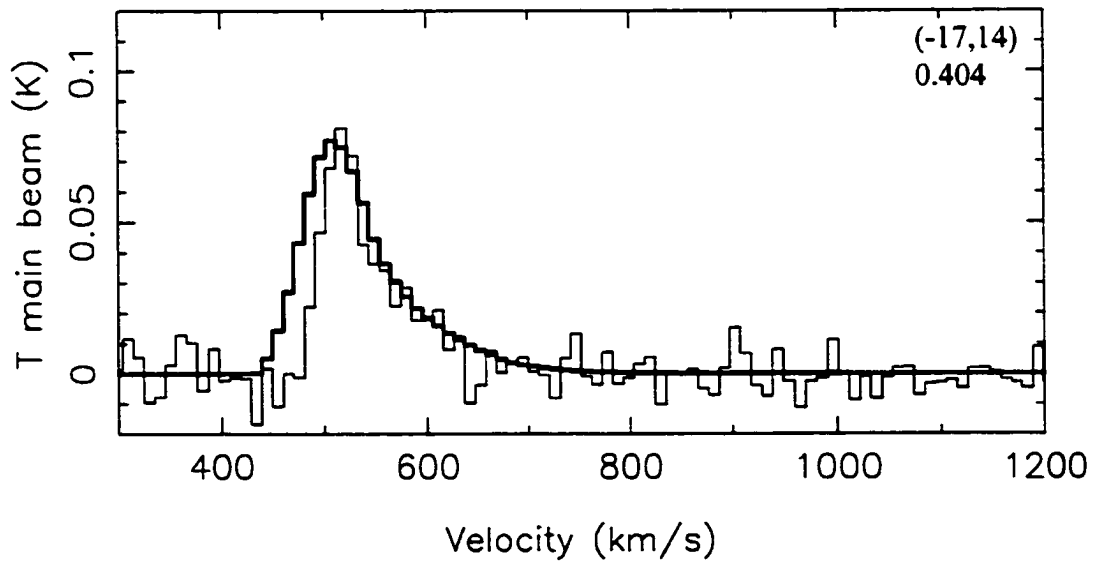
Figure 3.4 Same as Figure 3.2 except the model offset is 25".
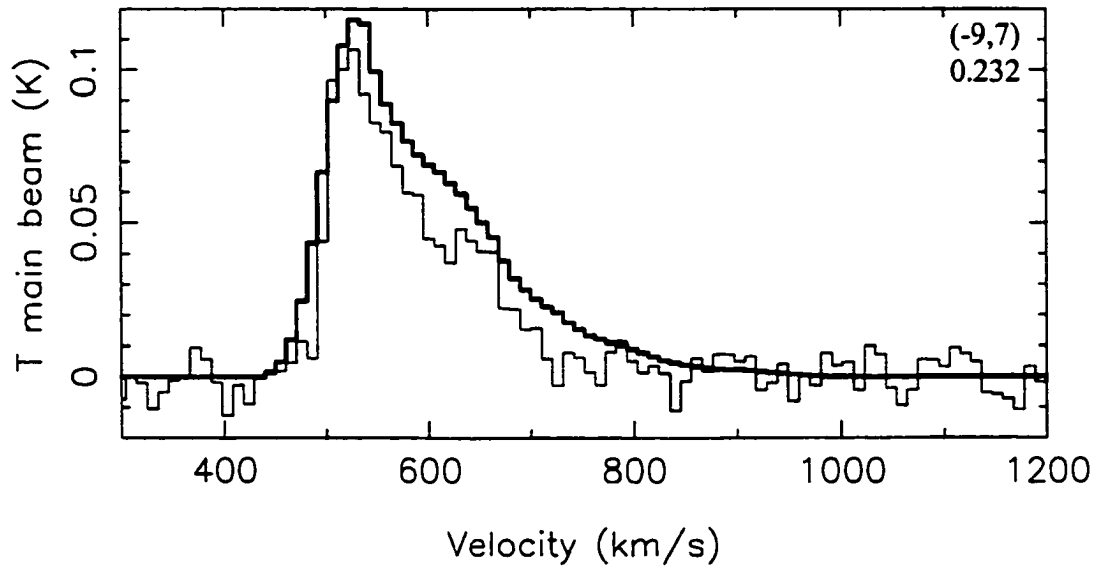
Figure 3.5 Same as Figure 3.2 except the model offset is 14".

Figure 3.6 Same as Figure 3.2 except the model offset is 3".

Figure 3.7 Same as Figure 3.2 except the model offset is –8".

Figure 3.8 Same as Figure 3.2 except the model offset is –19".

Figure 3.9 Same as Figure 3.2 except the model offset is −30".

Figure 3.10 Same as Figure 3.2 except the model offset is −41".
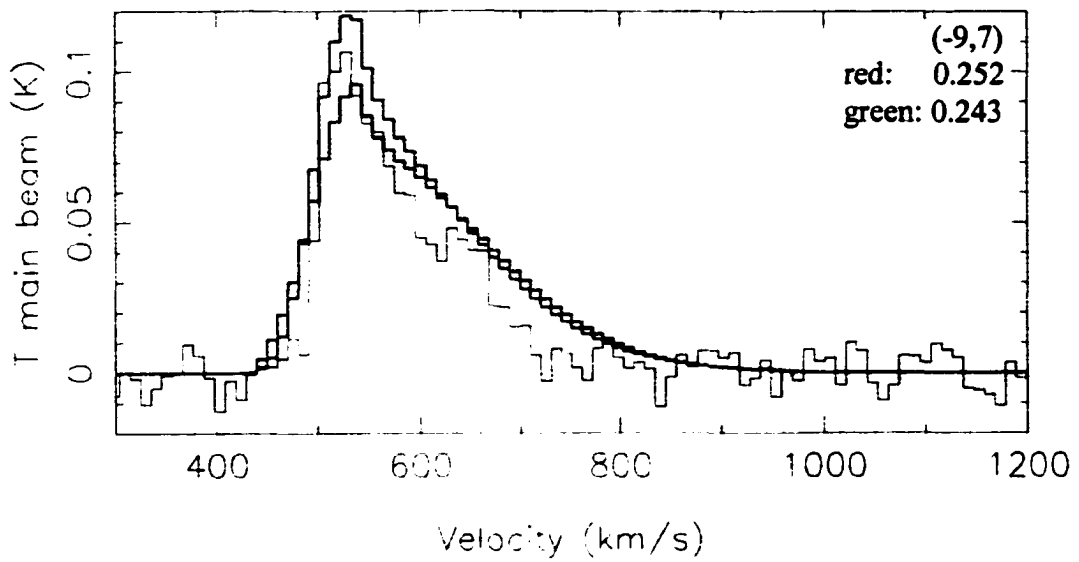
Figure 3.11 This and the following three figures show how a Gaussian ring model and a Gaussian disk model differ. The red line is the Gaussian ring model with no asymmetries (ring radius =15" and FWHM = 15"), the green line is the Gaussian disk model which best matched the data (FWHM = 45") and the noisy black line is the data. The model offsets are 14". The telescope pointing offset in arcseconds and the "goodness of fit" for each model is recorded in the top right hand corner.

Figure 3.12 Same as Figure 3.11 except the model offsets are 3".
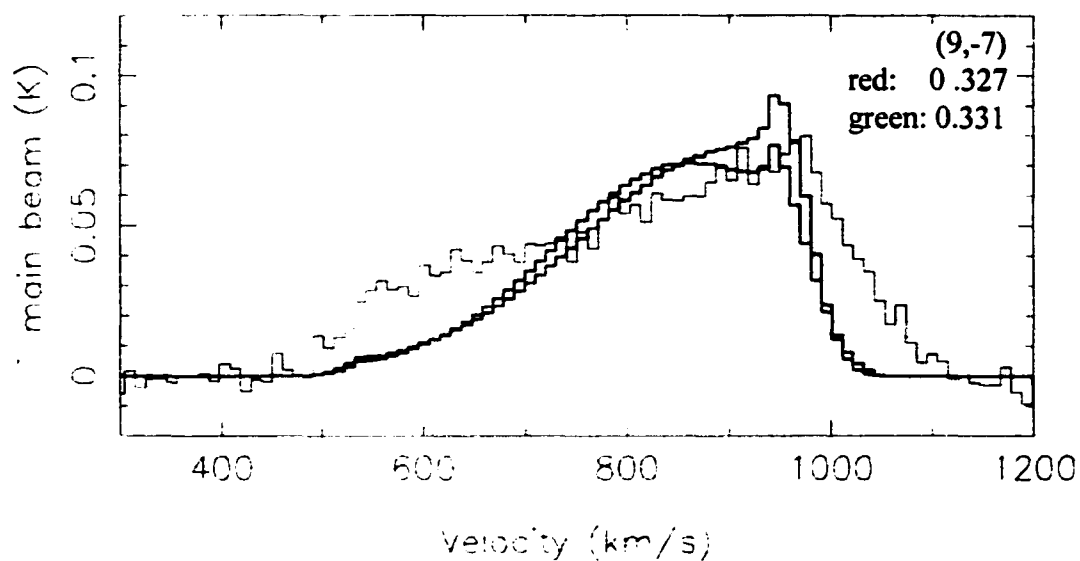
Figure 3.13 Same as Figure 3.11 except the model offsets are -8".
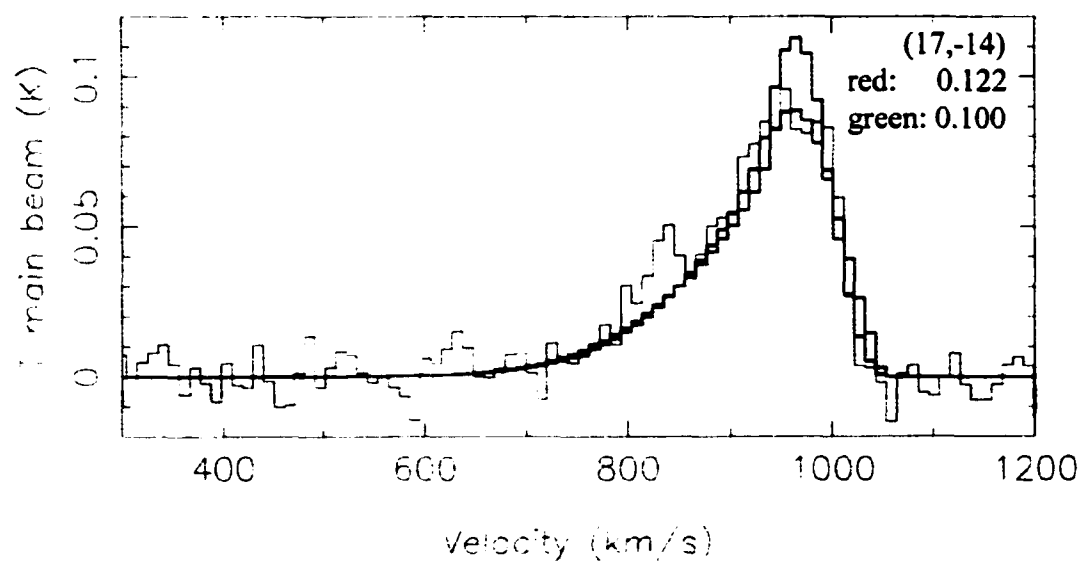
Figure 3.14 Same as Figure 3.11 except the model offsets are -19".
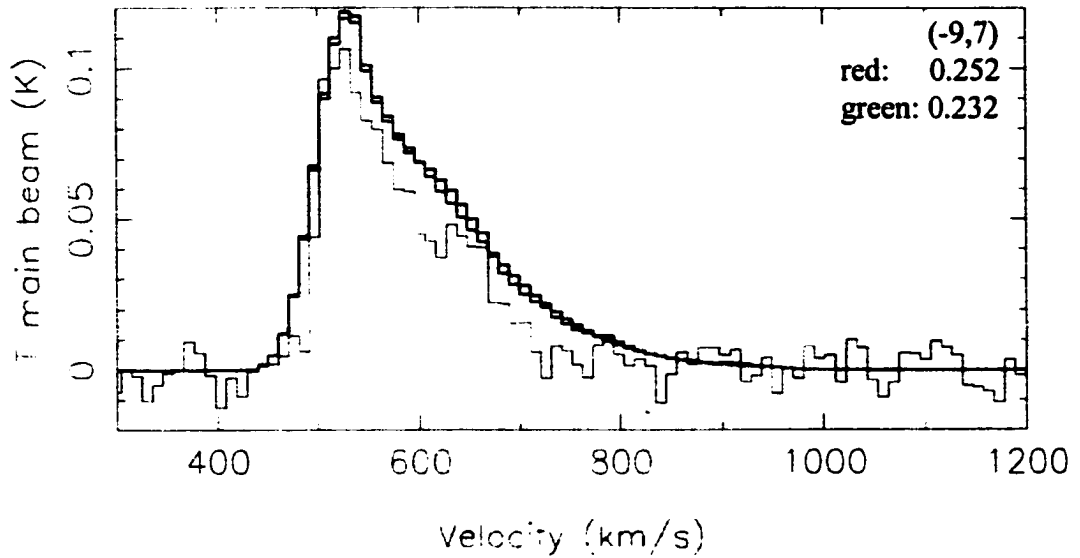
Figure 3.15 This and the following three figures illustrate how the addition of asymmetries to the plain Gaussian ring improve the model. The red and black lines are the same as in figures 3.11-3.14. The green line is the Gaussian ring model (ring radius = 15", FWHM = 15") with the asymmetries (as in Figures 3.2-3.10). The telescope pointing offset and the "goodness of fit" for each model is located in the upper right hand corner. The model offsets are 14".
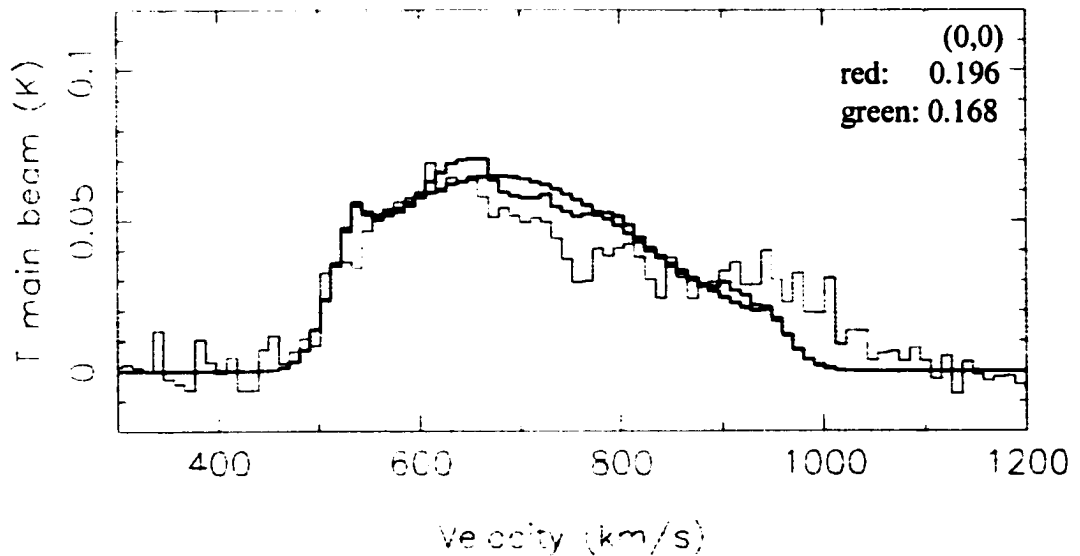
Figure 3.16 Same as Figure 3.15 except model offsets are 3".
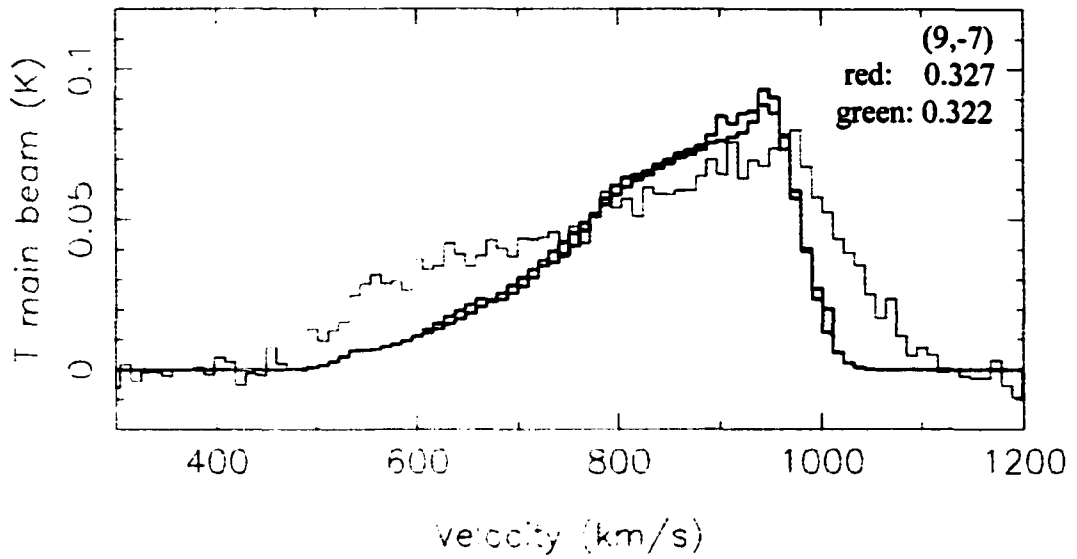
Figure 3.17 Same as Figure 3.15 except the model offsets are –8".
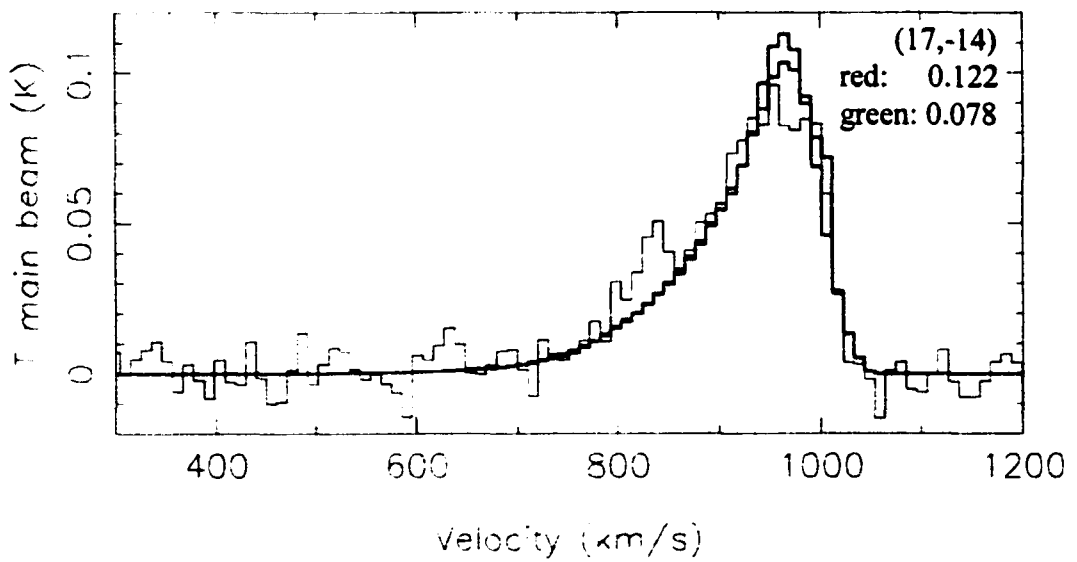
Figure 3.18 Same as Figure 3.15 except the model offsets are –19".

In an effort to further improve the model fit to the data, the edge-on, Gaussian ring was tilted from the line of beam pointings, thereby making the power pattern further away from the emitting ring for the outer pointings. Using different asymmetry distributions in the Gaussian ring, the tilted models could indeed improve the fit to the data slightly. The goodness parameter declined by only a few percent over the best fit model reported in table 3.3. If the molecular gas in NGC 5866 has been accreted from an external source, it is possible that it has not yet settled into the plane of the galaxy. Another possibility is that the molecular ring is not tilted but warped at larger radii. The tilted ring model would produce spectra that look the same as a warped disk or ring at large radii. Both would move the source further away from the power pattern beam and produce spectra with less power than expected. Figure 3.4 clearly shows the best fit model produces too much power but reproduces the same shape. A tilt or warp in the gas distribution would correct this. The tilted models were not adopted because they suggest that the molecular gas is not closely traced by the optical dust lane, a seemingly improbable result based on the well known, close association between molecular gas and dust in spiral galaxies.

3.2.2   The Kinematics

One of the most curious results is how the molecular gas appears to be rotating. The broad lines ($\sim$610 kms^{-1}) in the spectra and the constant position of the saw tooth shape in velocity space across the galaxy, shown in chapter 2, clearly reveal a large rotational velocity. Fisher (1997) published rotation curves of the stars and [O III] (5007 Å) based on line-of-sight velocity distribution data for 18 S0 galaxies, including NGC 5866. The data reveal that the stellar rotation curve rises linearly up to 200 kms^{-1} at a radius of about

30". The ionized gas, presumably the result of HII regions, rotates in two regimes, rising quickly to ~68 kms^{-1} at 2.5" and then again, showing a linear rise up to 200 kms^{-1} at 30". The curve appears to level out but there is no [O III] data past 30". Attempts to model the CO spectra with the observed stellar and [OIII] rotation curves from Fisher (1997) failed to reproduce the observations due to the fact that both rotation curves reach maximum values near 200 kms^{-1}. Figure 3.19 shows the stellar rotation curve from Fisher (1997) and the approximation to it used by COSPEC. Figure 3.20 shows Fisher's data together with the approximation used by the program. Figure 3.21 shows both the stellar and [OIII] data of Fisher along with a rotation curve needed to reproduce the CO observations. The molecular gas is rotating very rapidly. Within a radius of 10" the required rotation curve rises to 200 kms^{-1}; a stark contrast to the rotation of the stars and ionized gas found by Fisher (1997). At this radius the stars and the ionized gas are rotating at around 75 kms^{-1}. The molecular gas rotation curve continues to rise out to 30" where it peaks at 305 kms^{-1}. There might be evidence of the gas slowing down further out as the large offset pointings still show the "saw tooth" pattern at slightly shifted velocity bins. Figures 3.3-3.4 and 3.9-3.10 are examples of this.
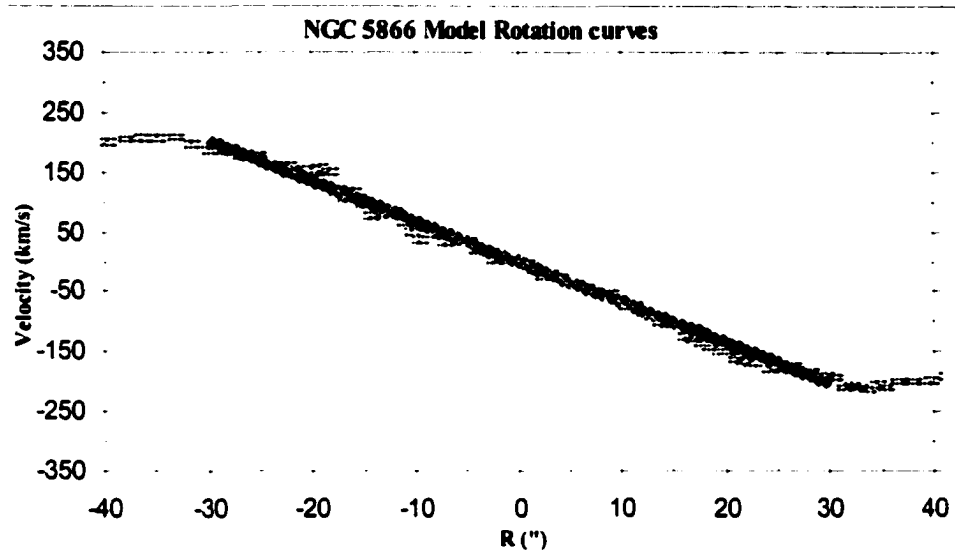
Figure 3.19 The Fisher (1997) stellar rotation curve data (yellow) and the approximation to it used by COSPEC (blue).
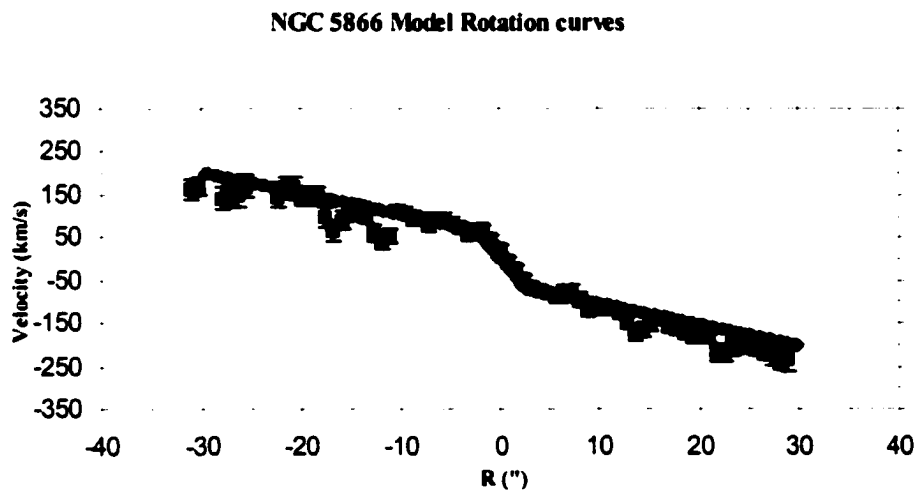
Figure 3.20 The Fisher (1997) [O III] rotation curve data (blue) and the approximation to it used by COSPEC (pink).
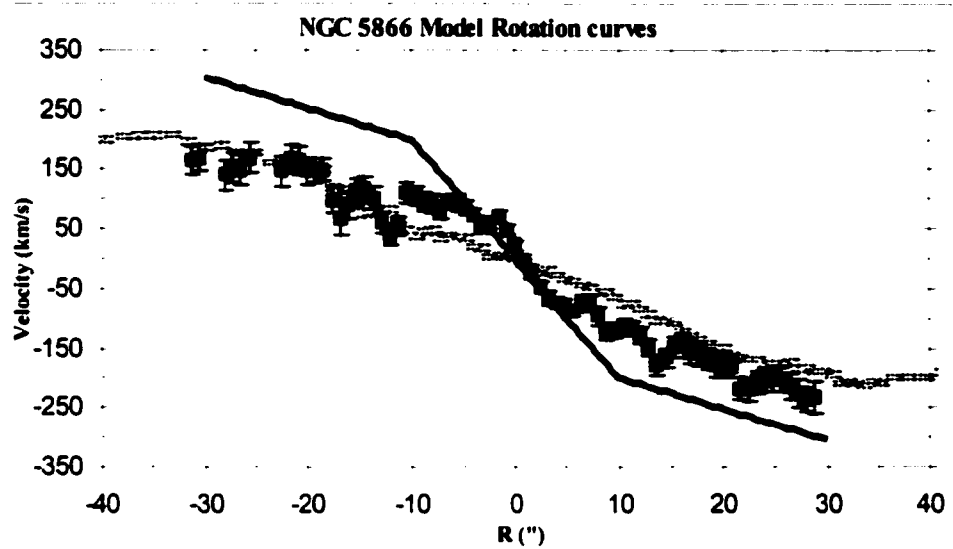
Figure 3.21 The Fisher (1997) stellar (yellow) and [O III] (blue) rotation curve and the best fit rotation curve used by COSPEC (red).

The large rotation speed implies that the molecular gas is decoupled from both the stars and the ionized gas. The bend in the rotation curve reveals that the gas rotates in two separate regimes.

The issue of why the CO line width is on the order of 200 kms^{-1} wider than that predicted by the [O III] rotation curve was addressed by running models which used the stellar and [O III] rotation curves found in Fisher (1997) along with a radially declining velocity dispersion component. These models test whether the large line width is due both rotation and velocity dispersion. In these models, the velocity dispersion is interpreted to be large scale motions of the CO and not a result of Doppler shifted signal from individual molecules. With velocity dispersion, the maximum rotation speed can be lower than when rotation is assumed to be the only factor which determines the line

width. Fisher (1997) finds that the [O III] velocity dispersion peaks in the centre at ~120 kms^{-1} and drops as the radius increases; this was assumed to be appropriate for the CO. The best fitting Gaussian ring intensity distribution (ring radius of 15" and a FWHM of 15") was used along with the stellar and [O III] rotation curves, both with and without velocity dispersion for comparison. The results are shown in figures 3.22-3.29. Figures 3.22-3.25 show the stellar rotation curve with and without velocity dispersion. Including a velocity dispersion improves the goodness of fit parameter for this model by ~20%, dropping the average value from 1.34 to 1.09. Figures 3.26-3.29 show the same thing only using the [O III] rotation curve. The [O III] rotation curve improves the fit over the stellar rotation curve regardless of velocity dispersion due to the slightly higher rotation speed and the faster rise out to ~2.5". The [O III] rotation curve still provides a poor fit, however. Again, velocity dispersion improves the fit, this time by ~30% with a goodness of fit parameter going from 1.17 to 0.897. Clearly, including a velocity dispersion does improve the fits, but does not reproduce the line width seen in the data. This suggests that the molecular gas is truly rotating more rapidly than the stars and the ionized gas.
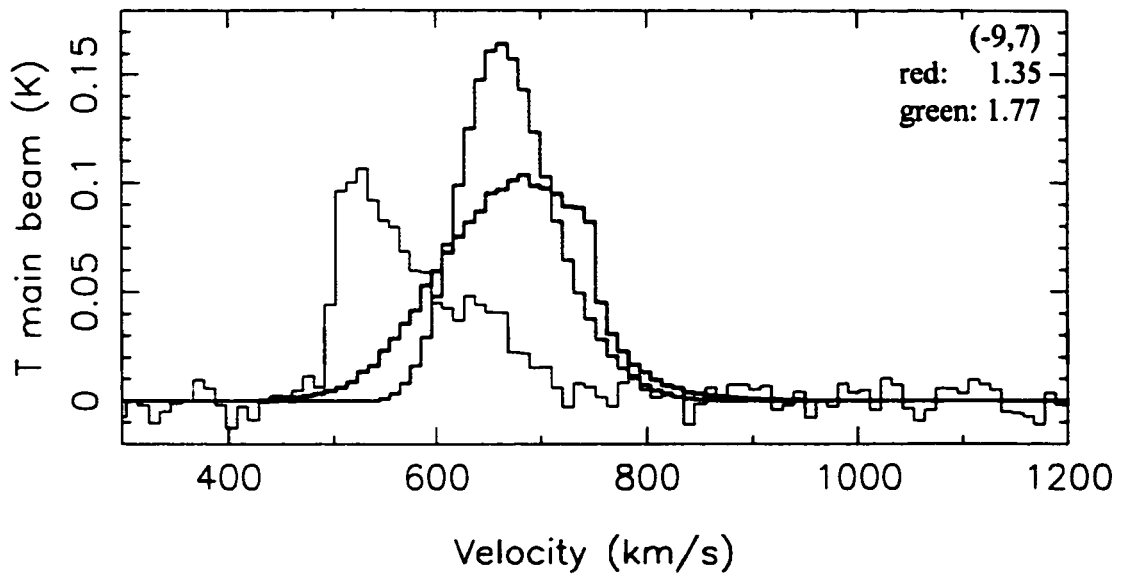
Figure 3.22 This and the following three figures show how the a Gaussian ring distribution using the stellar rotation curve, with and without velocity dispersion match the data. The green line is the Gaussian ring model (ring radius = 15", FWHM = 15") using the stellar rotation curve for NGC 5866 found in Fisher (1997), the red line is the same model with a velocity dispersion component. The telescope pointing offset and the goodness of fit for each model is recorded in the upper right hand corner. The model offsets are 14".
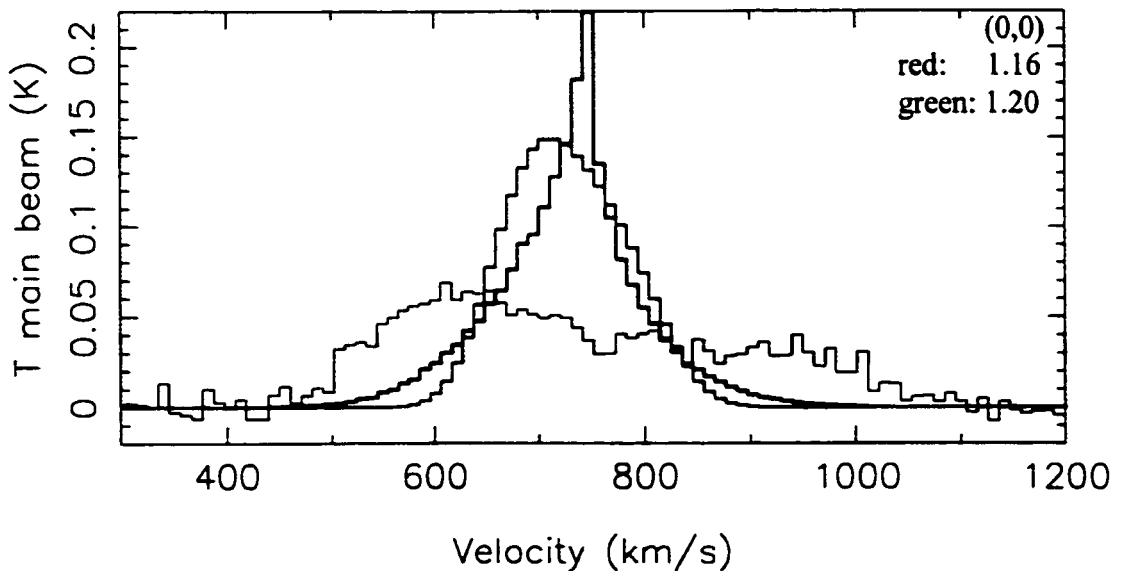
Figure 3.23 Same as Figure 3.22 except the model offsets are 3".
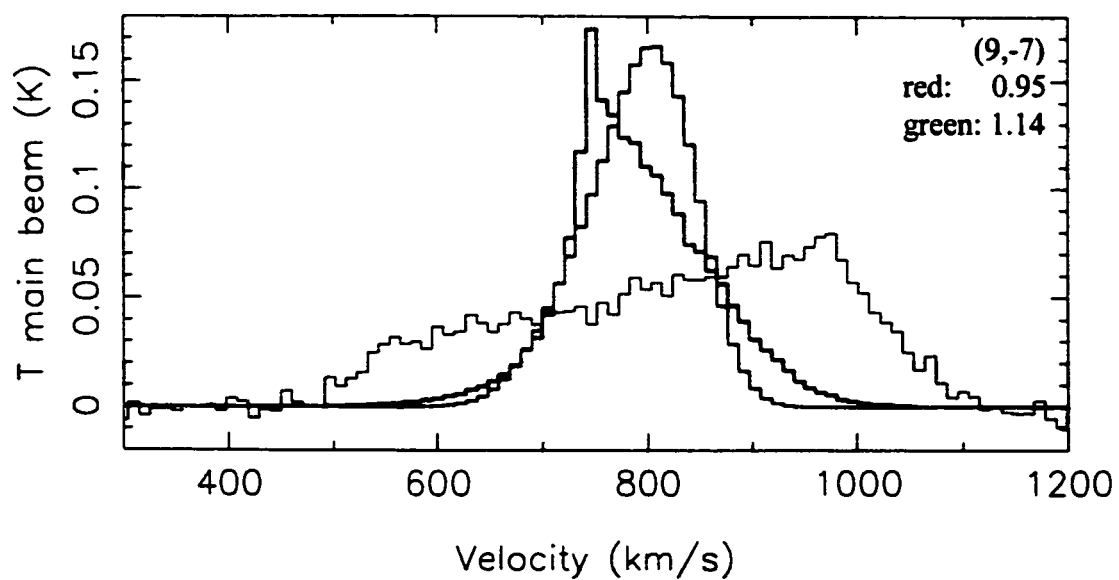
Figure 3.24 Same as figure 3.22 except the model offsets are -8".
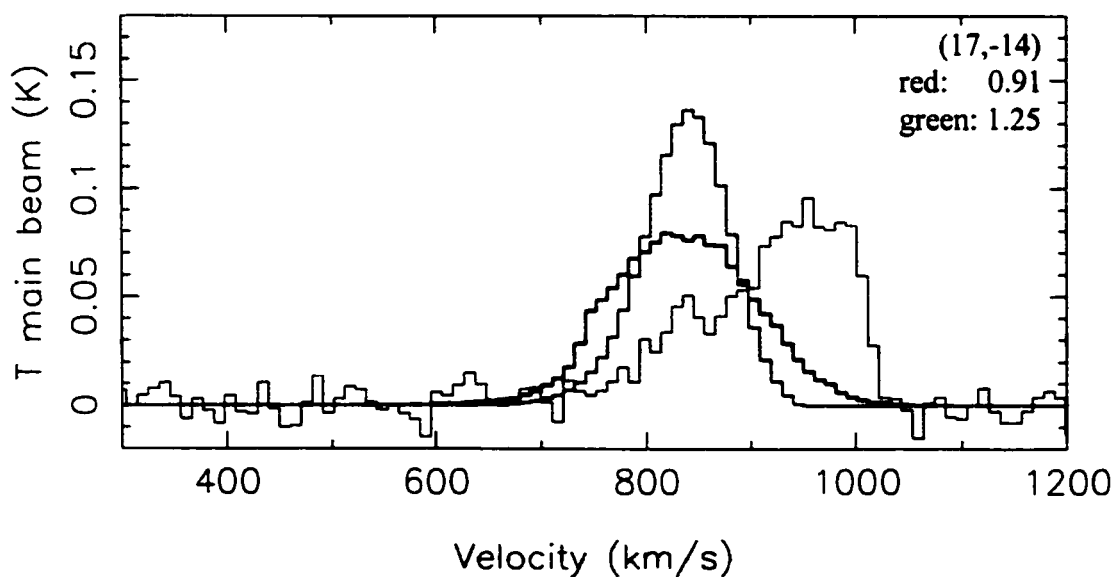
Figure 3.25 Same as Figure 3.22 except the model offsets are -19"
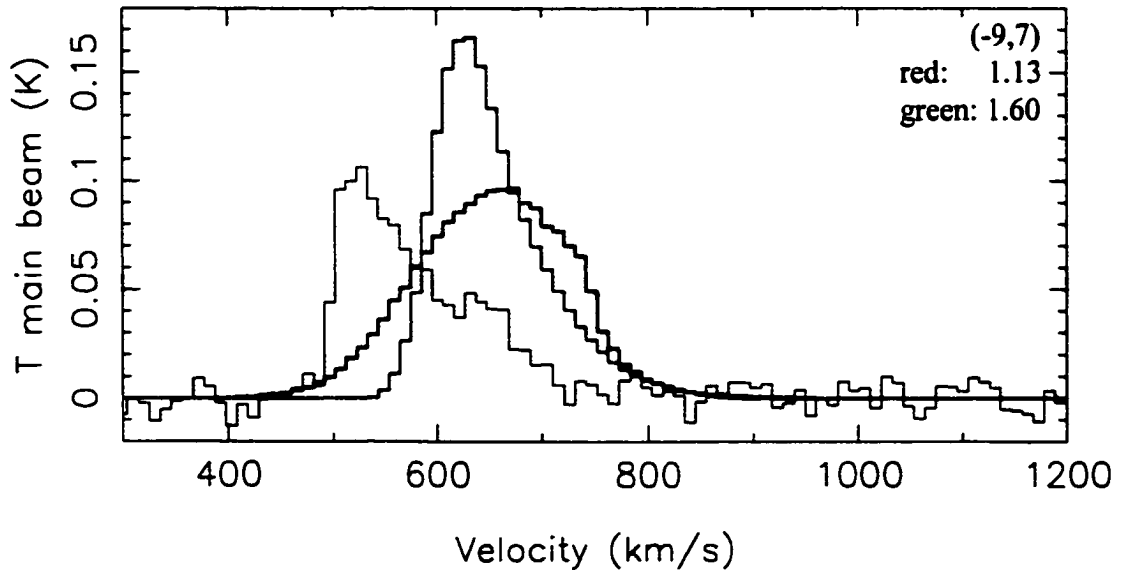
Figure 3.26 This and the following three figures show how the a Gaussian ring distribution using the [O III] rotation curve, with and without velocity dispersion match the data. The green line is the Gaussian ring model (ring radius = 15", FWHM = 15") using the [O III] rotation curve for NGC 5866 found in Fisher (1997), the red line is the same model with a velocity dispersion component. The telescope pointing offset and the goodness of fit for each model is recorded in the upper right hand corner. The model offsets are 14".
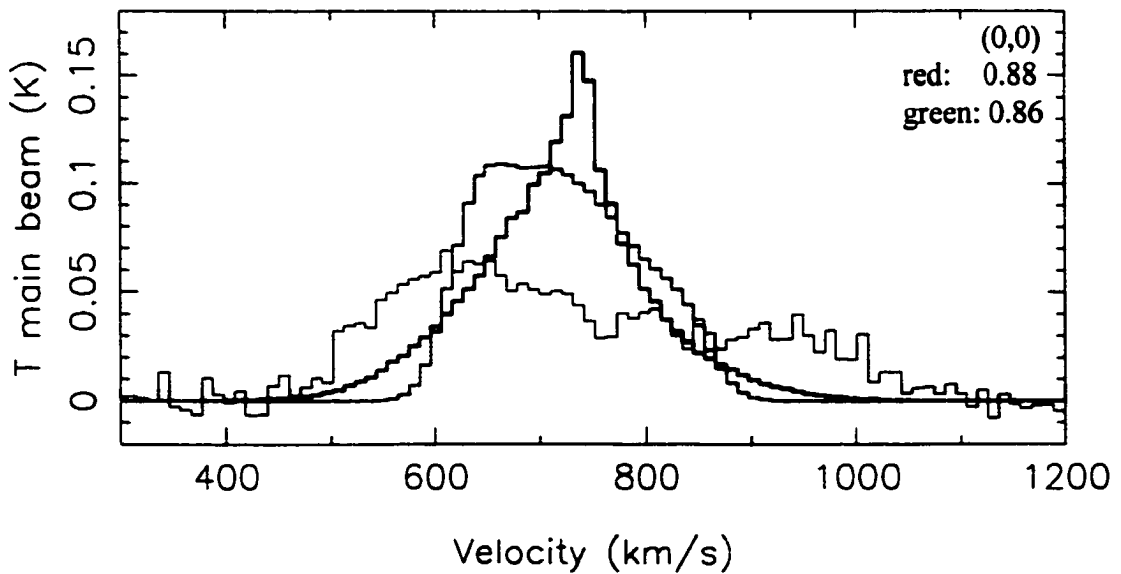
Figure 3.27 Same as Figure 3.26 except the model offset is 3".

(9,-7)
red: 0.79
green: 0.98
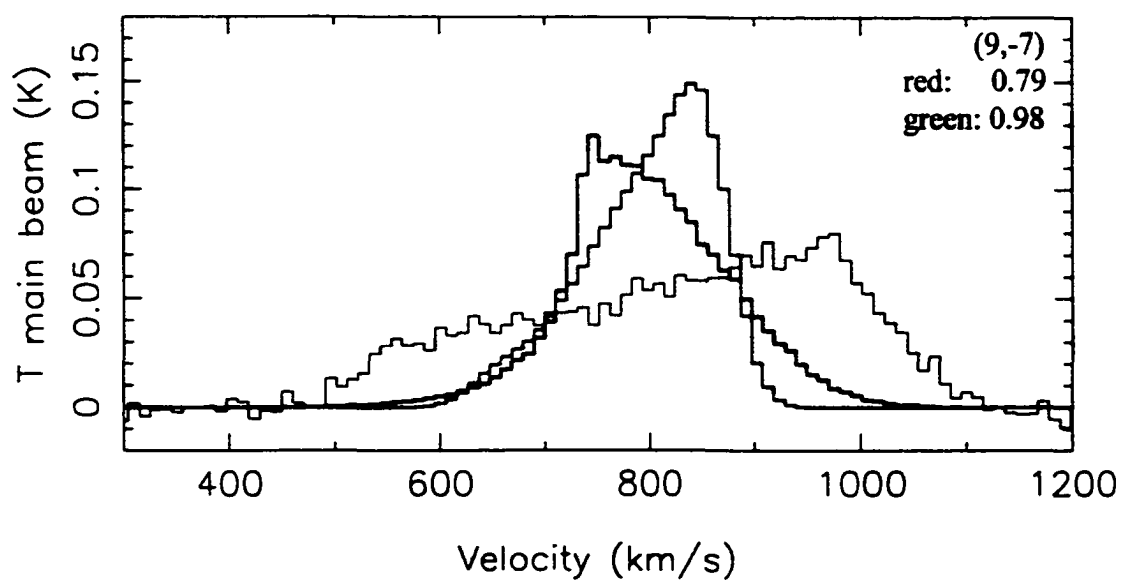
Figure 3.28 Same as Figure 3.26 except the model offsets are –8".

(17,-14)
red: 0.79
green: 1.23
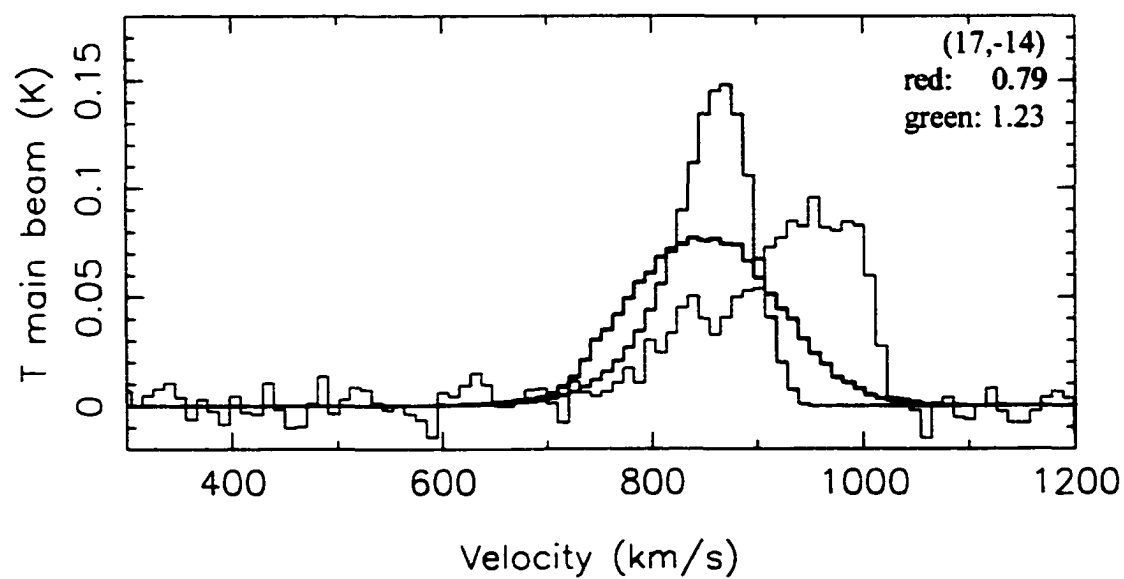
Figure 3.29 Same as Figure 3.26 except the model offsets are –19".

A velocity dispersion component was also added to the best fit model. Figures 3.30-3.33 show how the Gaussian ring distribution with asymmetries and the same model with velocity dispersion compare to the data. Since the best fitting model does not include a velocity dispersion, it is not surprising that it does not improve the fit (average goodness with velocity dispersion of 0.26 as opposed to 0.20 for the best fit without velocity dispersion). That is, the best fitting model was found by adding asymmetries to correct for deviations from a plain Gaussian ring and a rotation curve which allowed for a 610 kms^{-1} wide line. Velocity dispersion only smears these out the asymmetries and overextends the line at the saw tooth pointings. The only exception is ~10% improvement the 9,-7 pointing (figure 3.32) which was discussed in section 3.2.1.
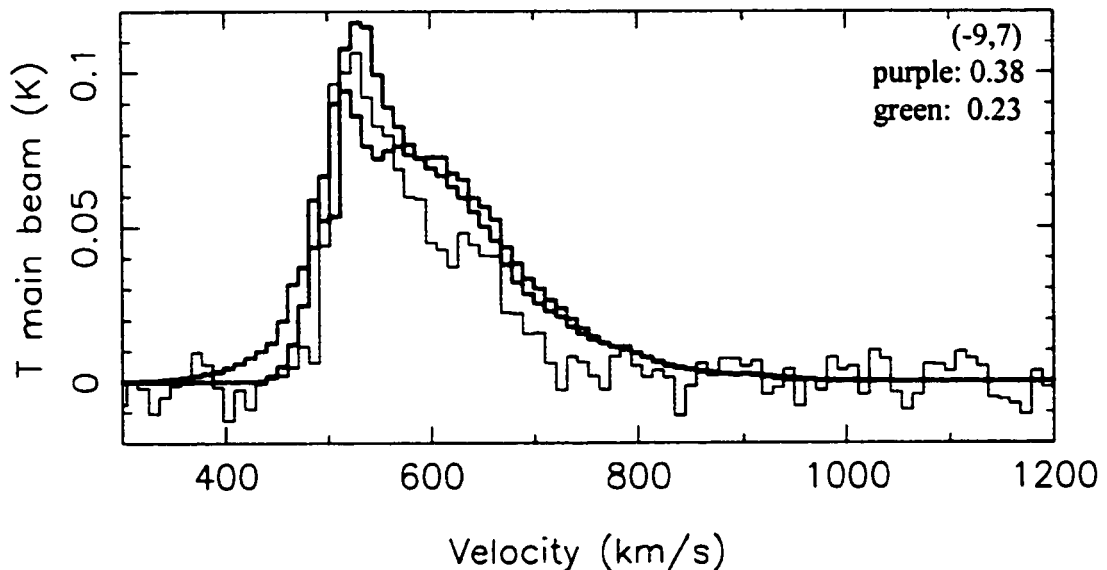
Figure 3.30 This and the following 3 figures illustrate the difference in the models when velocity dispersion is added to the best fit model. The green and black lines are the same are Figures 3.15-3.18. The purple line is the Gaussian ring model (ring radius = 15", FWHM = 15") with asymmetries and a velocity dispersion component. The telescope pointing in arcseconds and the goodness of fit for the two models is recorded in the upper right hand corner. The model offsets are 14".
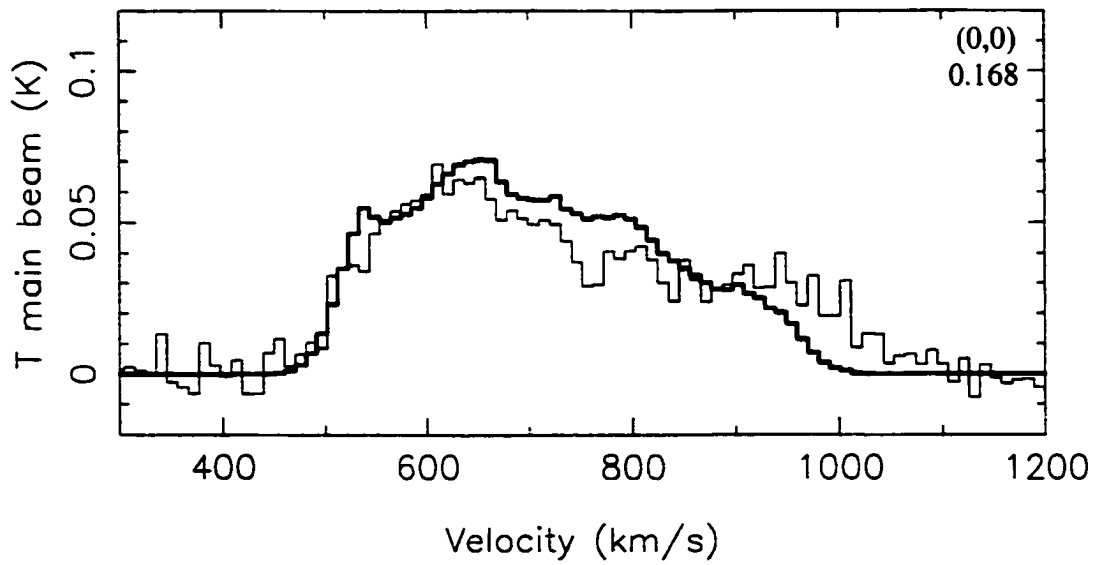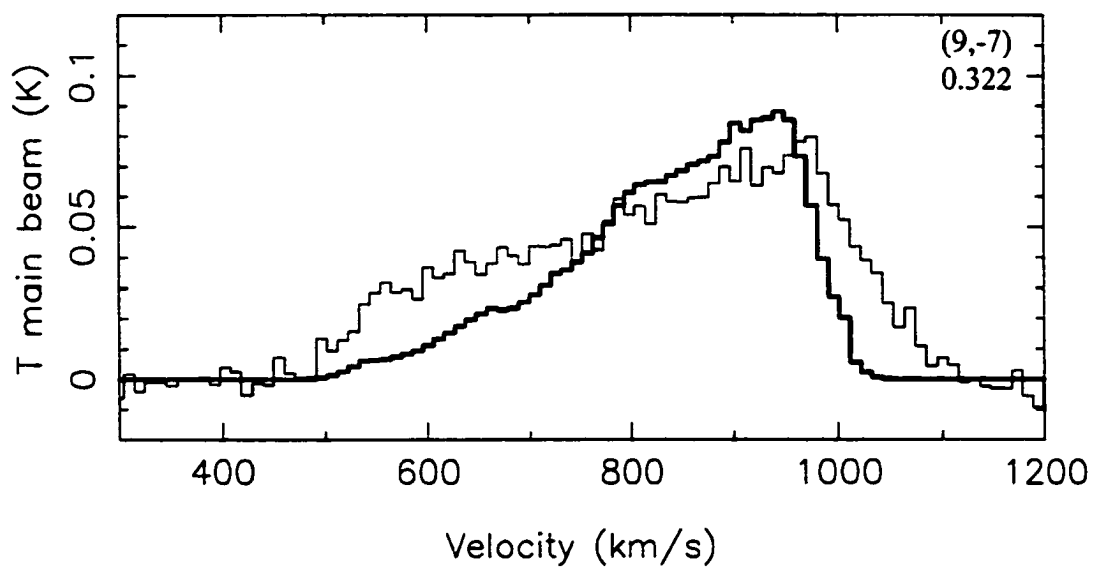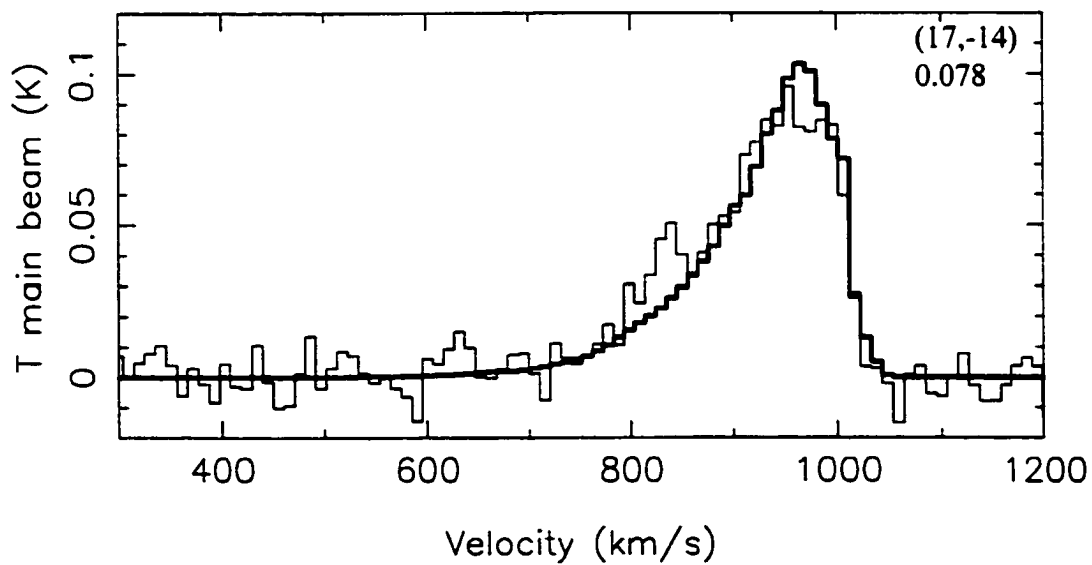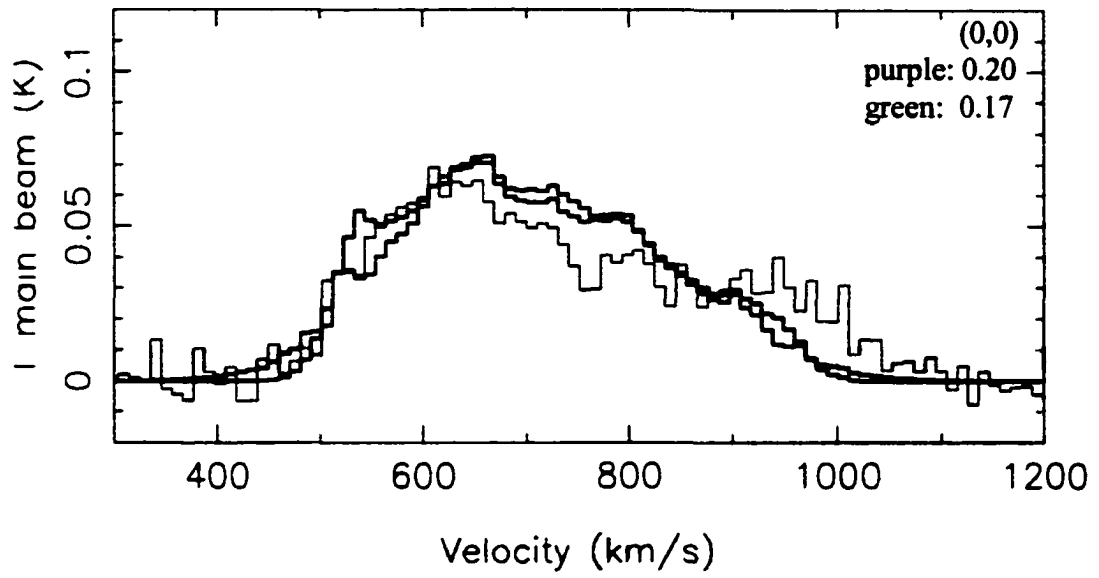
Figure 3.31 Same as Figure 3.30 except the model offsets are 3".
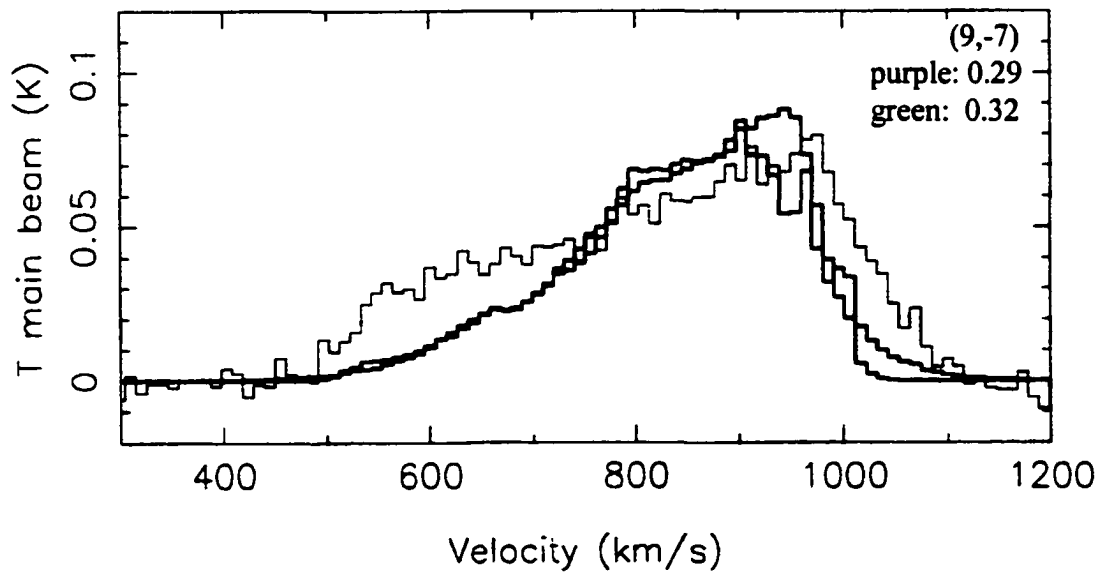
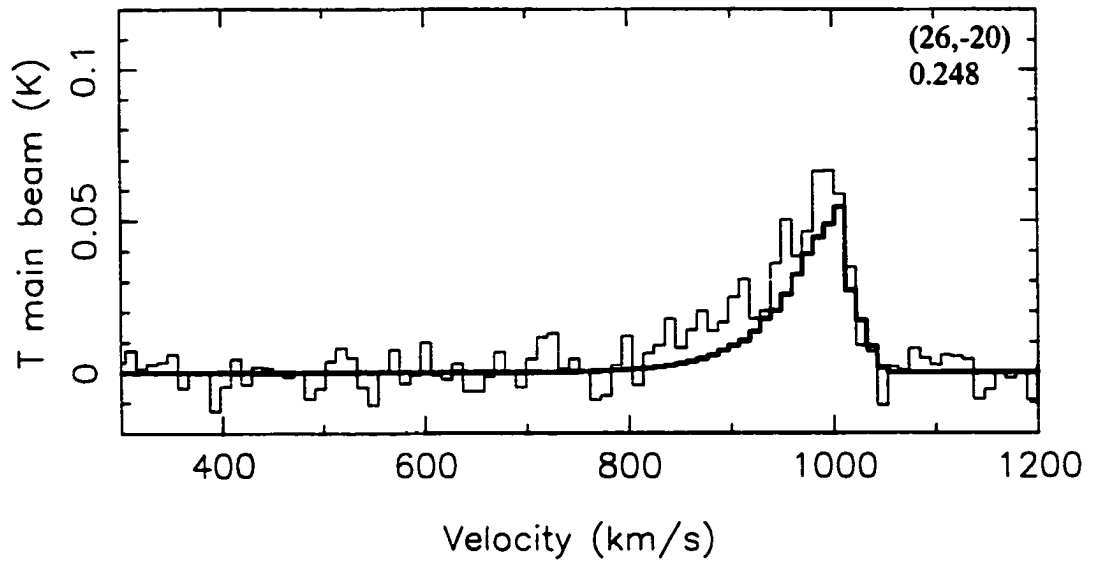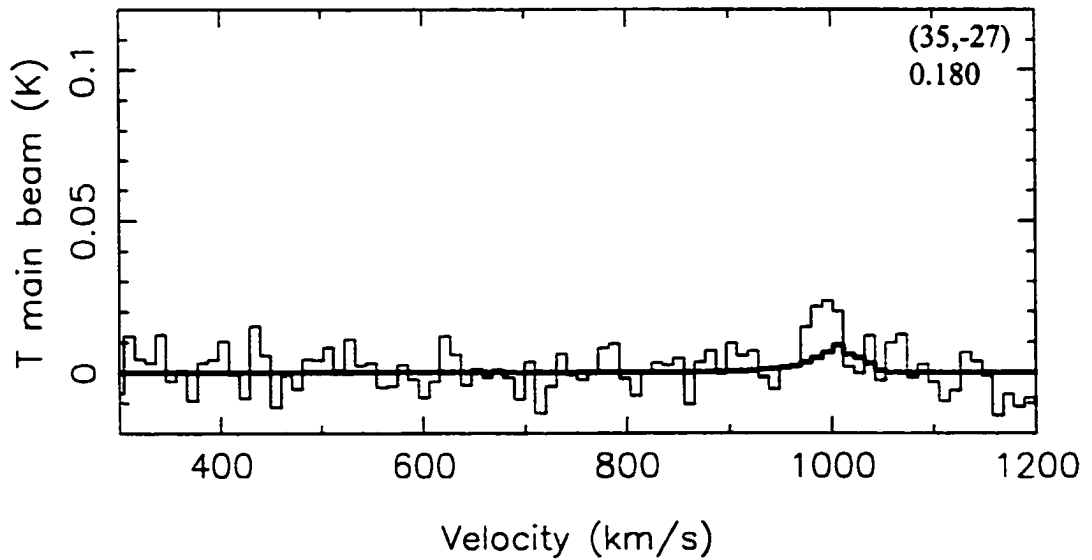**Figure 3.32** Same as Figure 3.30 except the model offsets are –8".

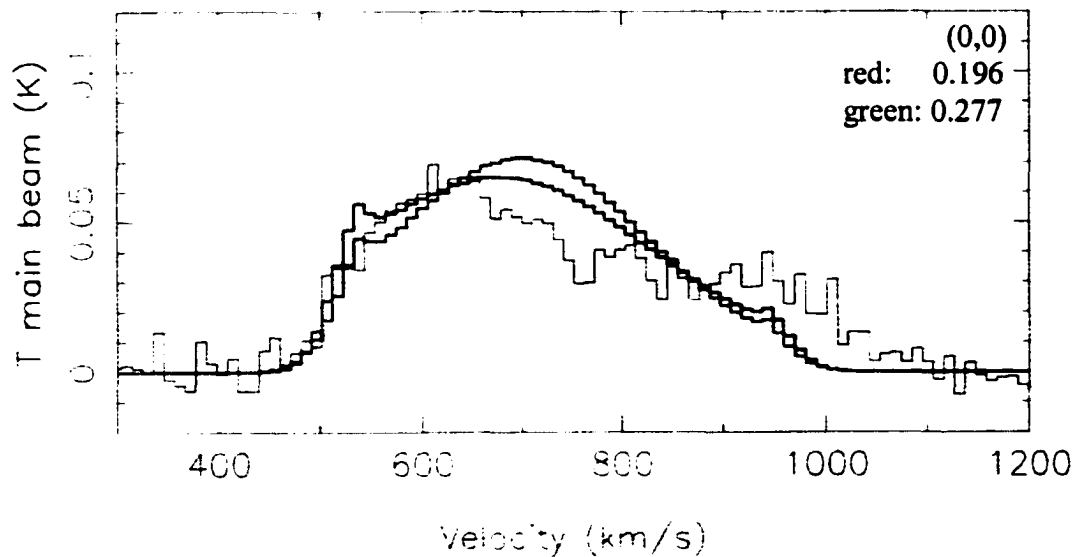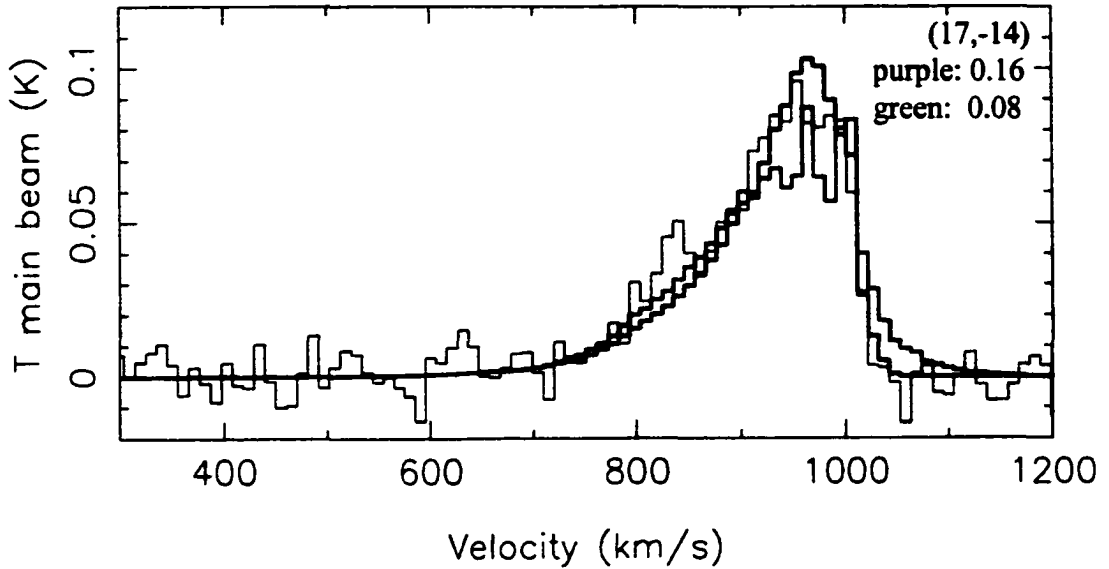**Figure 3.33** Same as Figure 3.30 except the model offsets are -19".

Despite the fact that velocity dispersion does slightly help reconcile the 9,-7 pointing model with the data, the assumption that the CO everywhere has the same velocity dispersion as the ionized gas is probably not a good one. The steep drop in intensity of the saw tooth line shapes seen in figures 3.5 and 3.8, for example, argue against a large velocity dispersion. This is clear when comparing the models with and without velocity dispersion (figures 3.30 and 3.33, for example). The power tapers off more slowly when velocity dispersion is included, showing slight power between 1040 and 1110 kms^{-1}.

Chapter 4

Discussion

4.1 Comparison to Other Early-Type Galaxies

4.1.1 The M_{H2}/M_{HI} Ratio

Henkel & Wiklind (1997) list 12 S0 galaxies with both H_2 and HI detections in their review of the cool ISM in early-type galaxies, within 25 Mpc, excluding Virgo cluster members. On average, $M_{H2}/M_{HI} = 0.44$ for this sub-sample of their work, whereas $M_{H2}/M_{HI} \geq 3.5$ for NGC 5866. The volume limited sub-sample of 7 S0 galaxies, again within 25 Mpc, again excluding Virgo cluster members, from Thronson *et al.* (1989) shows an average M_{H2}/M_{HI} of ~1.7. The volume-limited survey of Welch & Sage find an average $M_{H2}/M_{HI} = 0.23$ for 9 S0 with positive HI detections in their sample (Welch, 2001). For the 10 S0s with only HI upper limits, a median value of 0.85 is found, however, they list a M_{H2}/M_{HI} lower limit for NGC 5866 of 0.87 (Welch, 2001). This value scales to 2.61 when taking into account that the upper limits on the HI mass are at the 3 sigma level. Since no solid conclusions can be made when the amount of HI is

unknown it is difficult to assess the true nature of the M_{H2}/M_{HI} is NGC 5866. However, based on the comparison to galaxies with positive HI detections, it would seem that M_{H2}/M_{HI} is somewhat high in NGC 5866. The reader should be reminded that there have been no positive detections of atomic Hydrogen in NGC 5866 and so the ratio could indeed be much higher than 3.5.

The H_2 surface density is one measure which can test whether the molecular to atomic Hydrogen mass ratio is a result of an overabundance of H_2 or a lack of HI, when compared to similar galaxies. Following Sage & Wrobel (1989) the surface density, Σ_{H_2}, was calculated using equation 4.1:

$$\Sigma_{H_2} = M_{H_2} / (\pi D_{25}^2 / 4) \quad (M_\odot/pc^2) \tag{4.1}$$

In this equation D_{25} is defined as the diameter at 25th magnitude/arcsecond^2 isophote in blue light and is taken from the Tully *Nearby Galaxies Catalogue* (see table 4.1). One then finds $\Sigma_{H_2} \approx 0.6 \ M_\odot/pc^2$, which is essentially the same as the median value found by

Sage & Wrobel (1989) for their sample of S0s. This might imply that the large value of the M_{H2}/M_{HI} ratio is due to a lack of HI in NGC 5866 and not an excess of H_2, however, many of the S0s in Sage & Wrobel's (1989) sample also have no detected HI. Regardless, it would seem that NGC 5866 does have a normal H_2 abundance. The presence of H_2 and the lack of HI is not unique to NGC 5866. Knapp (1998) reports that 47% of S0s have H_2 (43 galaxies surveyed) while only 20% have HI detections (103 galaxies surveyed). These percentages are most likely biased by Virgo cluster members, however, the point that a solely molecular cool ISM is not unique remains. Elmegreen

(1993) showed that the molecular and atomic ISM is sensitive to changes in pressure. A slight increase in pressure is capable of converting entire HI regions into H_2. Self-shielding from ambient radiation inside gas clouds increases sensitively with pressure. A pressure change can be caused by a close passage of a companion, for example. This might not cause collapse of a gas cloud but only a phase change. Since the H_2 surface density in NGC 5866 is normal for an S0 galaxy, and the molecular to atomic hydrogen mass ratio is higher than average, this suggests that the HI is absent and not simply converted into molecular gas.

4.1.2 The Star Formation Rate

The interstellar medium seems normal in its star formation rate based on a sample of similar galaxies. Thronson *et al.* (1989) calculated SFR_{FIR} for 5 IRAS selected, X-ray emitting S0 galaxies, including NGC 5866, finding a $SFR_{FIR} = 1.3$ $M_\odot$/yr for NGC 5866, based on a distance of 11 Mpc (scaling to 15.3 Mpc gives 2.52 $M_\odot$/yr, virtually identical to the SFR presented in equation 3.16), while the average for the sample is $SFR_{FIR} = 1.25$ $M_\odot$/yr. Caldwell, Kennicutt & Schomer (1994) find an average $SFR_{H\alpha} = 4 \times 10^{-3}$ $M_\odot$/yr for a sample of 8 S0 galaxies within 40 Mpc ($H_o = 75$ kms^{-1}/Mpc), around 10 times lower than $SFR_{H\alpha} = 0.047$ $M_\odot$/yr found here for NGC 5866. Defining an average star formation rate is difficult due to the varied values obtained by the different methods of calculating SFR and the differing assumptions that go into each model. The results shown in the previous chapter seem to be average or slightly above for an S0 galaxy, based on the Thronson *et al.* (1989) results.

4.1.3 The CO Distribution

The kinematic model of NGC 5866 reveals that the molecular gas is most likely in a Gaussian ring distribution with large holes in the ring and several "hot" spots, mostly on one side. Molecular rings in spirals are fairly common (Pogge & Eskridge, 1993, Regan *et al.*, 2001). The Milky Way contains an inner molecular ring of radius ~190 pc (Oort, 1977, and references therein) and the CO line emission from this ring has approximately a Gaussian radial profile (Sumin, Fridman & Khaud, 1991). The Milky Way also has a ring of molecular clouds which span a radius range of 4 to 8 kpc and is peaked at 5.5 kpc < R < 6.5 kpc (Sanders, Scoville & Solomon, 1985). Pogge & Eskridge (1993) find 10 out of 14 S0 galaxies with HII disks (10 of 32 in the full S0 sample) have ring-like distributions of HII regions, implying that the molecular gas from which the newly formed stars which ionize the gas is also distributed in the same fashion. The ring radii vary between 0.24 kpc to 14.9 kpc having a median value of 2.32 kpc which is similar to the 1.1 kpc molecular ring assumed for NGC 5866 from the models. Lesch *et al.* (1990) propose that all spiral galaxies with rotation curves which change from rigid body to differential rotation at some transition radius, r_t, should have a gas ring. The physical mechanism is that angular momentum is carried out radially in the differential rotation regime causing gas to fall inward towards r_t due to viscosity. The NGC 5866 model rotation curve, however, does not contain a differentially rotating regime, nor is one suggested by Fisher's (1997) data until past a radius of 30". Gas rings might also arise through galaxy harassment (Icke, 1985) or a merger (Sofue, 1994). Therefore, it is not surprising to find a ring like distribution of molecular gas in NGC 5866 since rings can be produced by both internal and external mechanisms.

The simple kinematic model provides reasonable fits for all pointings except the 9,-7 offset (figure 3.7). The telescope was pointed toward the redshifted side of the galaxy but there is clearly excess signal compared to the model below the systemic velocity (745 kms^{-1}). This extra blueshifted intensity cannot be accounted for by a simple Gaussian ring or any of the attempted intensity profiles (see appendices B & C). The signal in the lower velocity bins could be the result of a pointing error, which, however, seems unlikely since it would imply a pointing error of ~5" for the one pointing only and various models with offsets between 0" and -8" failed to reproduce the spectrum width. It could also be that at the 9,-7 offset the telescope views gas whose kinematics differs from that assumed in the simple model. This could be a large amount of gas perturbed by a supernova event. Another possibility is a second, smaller disk or ring viewed by the 9,-7 pointing. The extra signal in the data compared to the model is on the redshifted side (~900-1050 kms^{-1}) when the model is pointed on the blueshifted side (+3", figure 3.6) and the opposite is seen when the convolving beam is pointed on the redshifted side (velocity bins ~495-745 when the model is pointed at -8", figure 3.7). It would seem that a secondary disk or ring of CO, rotating about a centre offset from that of the primary disk, could explain this result. The centres would need to be offset in order to ensure that the convolving beam "sees" the blueshifted gas when pointed on the redshifted side of the galaxy. There is other evidence for the necessity of a multi-component model for the CO in NGC 5866. Looking at figures 3.5 and 3.8, the "saw tooth" pointings, a secondary peak can be seen in both, located ~100 kms^{-1} from the systemic velocity of 745 kms^{-1}. These peaks could not be modelled by placing in clouds without producing large spikes in other pointing spectra. Since these secondary peaks correspond to a maximum rotation

rate of ~100 kms^{-1}, this cannot be the source of the extra signal seen in figures 3.6 and 3.7. Multiple concentric gas rings in galaxies are not uncommon (Buta & Crooker, 1993) and NGC 5866 may fall into this category. However, it is difficult to accept a second centre of rotation from basic dynamical considerations. An interferometric study of the centre of NGC 5866 is needed to address this issue.

4.1.4   The Molecular Gas Kinematics

The most intriguing feature of NGC 5866 presented in this work is the rapid rotation of the CO compared to the stellar and ionized gas. Kinematically decoupled gas and stars are not uncommon in early-type galaxies. Fisher's data shows >40% (at least 4 of 9) of the S0 galaxies detected in [O III] (5007 Å) have gas obviously decoupled from the stars.

Most theories to explain decoupled stars and gas involve some form of interaction with another galaxy, like the ones discussed in section 4.3 and 4.4 (Bertola *et al.* 1992, Fisher, 1997), but the differing rotation curves can be accounted for in some cases by a bar, warp or non circular motion (Fisher, 1997), all of which can form internally. The question of why there is an apparent difference between the kinematics of the molecular and ionized gas in NGC 5866 is harder to explain. Since the young stars that ionize the gas form from the molecular gas, it is hard to understand how the two gas components could rotate separately.

The rotation curve used in this work was not measured, but only suggested by the CO data. It is argued in section 3.2.1 that the adopted rotation curve is probably correct to

first order since the CO spectra suggest little velocity dispersion and models using the ionized gas and stellar rotation curves, with and without velocity dispersion, clearly fail to match the data (figures 3.22-3.29). Unpublished interferometry confirm that the CO rotates in excess of 300 kms^{-1} (Wang & Hui, 1994, private communication). Fisher cautions that the ionized gas may indeed be rotating faster than indicated by the [O III] measurements since the [O III] measurements along the major axis do not go out as far as the stellar measurements. Therefore, the [O III] data might not be reliable for modelling the CO kinematics. That fact would not be unprecedented. Prada et al. (1996) report Brγ (2.1661 μm) and H$_2$ 1-0 S(1) (2.1218 μm) observations of the highly inclined, late type spiral, NGC 253 motivated by an apparent discrepancy between the kinematics suggested by CO (Canzian, Mundy & Scoville, 1988) and optical [N II] (6584 Å) data (Ulrich, 1978). The CO rotation curve of NGC 253 is 7 times steeper than the optical rotation curve, much like that seen in figure 3.21 for NGC 5866. The assumption of Prada et al. is that the dust in NGC 253 is obscuring the optical radiation and producing a flattened rotation curve. Essentially, the extinction by the dust at optical wavelengths causes the line-of-sight velocity distribution to measure gas that is at large radii and at some azimuth instead of along the radius assumed from the major axis offsets. The near IR measurements confirm the CO data results (Prada et al., 1996). This effect has been seen in NGC 2146 (Prada et al., 1994) and in NGC 4565 (Sofue et al., 1998).

The [O III] emission from NGC 5866 probably suffers similar extinction due to its prominent dust lane. Near IR measurements might reconcile the ionized and molecular

gas kinematics. Even so, the gas is still rotating on the order of 100 kms^{-1} faster than the stars, and any theory for the origin of the gas in NGC 5866 needs to account for this.

4.2 An Internal Origin for the Cool Interstellar Medium

4.2.1 Interstellar Matter Mass Return and Consumption

The measured molecular gas mass of NGC 5866 is 4.55×10^8 M$_\odot$, which gives a cool ISM mass of $M_{ISM} = 6.4 \times 10^8$ M$_\odot$ after scaling by a factor of 1.4 to include Helium (10% by number). This value is essentially the same as that found by the mass return calculation (Faber & Gallagher, 1976, Peimbert, 1993), $\sim 10^9$ M$_\odot$, not factoring any star formation. The current star formation rate as derived from the Hα luminosity suggest that mass balance can be maintained, since no more gas is being used to form new stars than is being returned. From this standpoint it would seem that NGC 5866 has evolved as a closed box, retaining most of its returned gas.

In a closed box scenario the large value of M_{H_2}/M_{HI} might be due to the dust in NGC 5866. The large amount of dust, suggested by the low gas to dust ratio, provides the perfect environment to create H$_2$ out of a reservoir of HI since it acts as both a shield from UV radiation and catalyzes surface reactions which form the molecular phase. The relatively low SFR of NGC 5866 also means that the amount of dissociating radiation is low since there are not many young OB stars. On the other hand, a totally molecular ISM is not a clear sign of closed box evolution (Elmegreen, 1993) and looking at the H$_2$ surface density it seems that NGC 5866 has probably not converted all of its atomic

hydrogen into the molecular phase. Also, a mix of HI and dust does not necessarily produce H_2, but is only a requirement for creating the molecular gas.

4.2.2 Cooling Flows and Molecular gas

Other evidence is consistent with closed box evolution. NGC 5866 has an X-ray corona (Pellegrini, 1994). X-ray emission from galaxies can arise from point sources, such as X-ray binaries, or an extended hot ISM. Cooling flows are hot "streams" of returned gas from evolved stars which are trapped in the galaxy's potential well and cooled by X-ray emission. Once this material is cool enough it can form molecular gas. D'Ercole & Ciotti (1998) performed simulations in order to follow the evolution of gas initially heated to X-ray temperatures by type II supernovae explosions within an S0 galaxy. Simulations with a time decreasing type I supernova rate form gas flows which initially move outward but reverse in direction at the galactic polar regions as the supernova rate declines. Cold filaments, which form at the interface between outflowing and inflowing gas, eventually form cold disks in the galactic centre. If this is the case in NGC 5866 it might explain any off axis detections of gas, presumably from the polar regions, and why the gas is decoupled from the stars, and so close to the centre of the galaxy.

However, the cooling flow model presents a problem for the creation of molecular gas. X-ray radiation destroys the dust necessary to form H_2 and so the molecular gas can only form after the hot ISM has cooled below X-rays temperatures. Also, analysis of ROSAT data (Pellegrini, 1994) indicates that most of the X-ray emission from NGC 5866 mostly likely comes from a population of X-ray binaries rather than a hot ISM.

4.3 An External Origin for the Cool Interstellar Medium

There are several lines of evidence that do not support the closed box evolution theory. The present observations clearly show that the molecular ISM is rotating, but much more rapidly than the stars. Similar conclusions have been reached by Wang & Hui (1994) from unpublished interferometry. Has the gas been captured? If so, the fact that we have found almost as much gas as expected from stellar mass return would appear to be just an odd coincidence. The fact that NGC 5866 has a dust lane tilted by $5°$ with respect to its optical major axis (Bertola *et al.* 1992) is often quoted as evidence for a past interaction (Burbidge & Burbidge, 1960, Bertola *et al.*, 1992, Pellegrini, 1994). If, indeed, NGC 5866 interacted in the past, the kinematically decoupled gas and stars are potentially a result of this. Based on the number of galaxies which show counter-rotating gas, Bertola *et al.* (1992) claim that 40% of S0s have acquired their ISM. Counter rotating gas is hard to explain in a closed-box scenario, where most of the gas we see should have come from stars and therefore should share their angular momentum.

4.3.1 Interactions

A merger with one or more smaller satellites could have provided NGC 5866 with its gas. During the cannibalization process, the gas and the stars of the smaller galaxy are affected in different ways. Stars are only affected by the total gravitational field, since stellar collisions are unimportant. However, gas clouds suffer dissipational collisions which cause gas to accumulate in a disk near the centre of the larger galaxy (Ibata, 2001 for example). A merger, therefore, seems like a good option for explaining the molecular gas kinematics.

Another form of interaction is galaxy harassment. "Galaxy harassment" involves interactions between 2 galaxies but without the exchange of material, necessarily. The theory was developed as an alternative to ram pressure stripping for converting later type spirals into early-types within rich clusters. It is a more general mechanism since it doesn't require the presence of an intergalactic medium. Harassment occurs when two galaxies pass close to one another. It is a good candidate to describe the nature of the ISM in NGC 5866 since it predicts that the stars will be unaffected (Icke, 1985), explaining the difference in the gas and stellar kinematics.

Simulations have shown that the required minimum separation is ~20-50 kpc to be effective, depending on the mass of the intruder and the relative velocity (Icke, 1985, Moore *et al.* 1995). Moore *et al.* (1995) modelled a cluster environment with galaxies of equal mass in order to follow morphological changes over several billion years. They found that a spiral needs ≤ 5 high velocity interactions to force morphological evolution, but did not investigate the fate of the ISM. Icke (1985) investigated how the gas behaves in a flyby scenario, finding that, under the proper conditions, only one interaction was necessary to convert a normal spiral into an S0. An important requirement was that the encounter must boost the gas velocity above the sound speed, but not above the mean velocity of the stars (i.e. less than the stellar velocity dispersion plus the rotational speed). Icke (1985) modelled interactions between galaxies with various mass ratios and concluded that a mass ratio larger than 1/5 is needed at a minimum distance of 20 kpc to induce a shock in the gas without affecting the stars. Under these conditions the gas located between the subject galaxy's centre and the centre of mass of the two body

system migrated inward, while gas on the other side of the centre of mass drifted outward. Icke's work might explain why molecular gas is found near the centre of NGC 5866, whereas HI, which is more widespread in galaxy disks, has not been detected.

Icke's simulations show that the infrared luminosity produced by the star burst created by the shocked gas is on the order of that seen in galaxies observed by IRAS. This might present a problem for NGC 5866, since its present FIR luminosity implies SFR < 2.4 $M_\odot$/yr, much lower than the 40 $M_\odot$/yr predicted by Icke (1985). If the harassment took place ~1 Gyr ago then the star formation might have dropped to its present rate from a much higher initial value. The low L_{FIR}/L_B ratio is consistent with this kind of scenario. Another problem is the separation of the NGC 5907 group members. The projected distances of the NGC 5907 group and their relative velocities would seem to negate any chance of multiple interactions, if NGC 5866 was a spiral converted to an S0 via the Moore et al. (1995) mechanism. Perhaps a comparison of star formation histories of the NGC 5907 group galaxies might provide a clue as to whether any of them might have "harassed" NGC 5866 in the past. The minimum amount of time possible since an interaction with any of the larger 5907 group members is ~4 Gyr based on their projected distances and relative velocities. This does not eliminate the possibility of interaction with fainter, undetected nearby galaxies.

4.4 The Local Environment

Since NGC 5866 shows signs of a potential interaction in the past, it is useful to look at other group members in order to establish if, indeed, interactions can and do take place in

the local environment. Other group members may show similar signs of interaction or present more convincing evidence. If this is the case, then an external origin for the gas in NGC 5866 would seem more plausible.

4.4.1 The NGC 5907 Group

Most S0s are found in environments much denser than that of the NGC 5907 group. The local density is defined as the number of galaxies brighter than $M_v = -16$ within a volume 0.5 Mpc per side (Tully, 1988). For example, the local density near the S0 galaxy NGC 4710, a Virgo member found on the outskirts of the cluster, is 2.00 Mpc^{-3}, whereas that near NGC 5866 is 0.24 Mpc^{-3}. The M_{H_2}/M_{HI} mass ratio in NGC 4710 has a $M_{H_2}/M_{HI} \approx 30$ whereas for NGC 5866 $M_{H_2}/M_{HI} \approx 3.5$. It is not surprising to find higher M_{H_2}/M_{HI} mass ratios in higher density areas like rich cluster galaxies since they are in an environment which is known to remove gas either through tidal stripping by other galaxies or by ram pressure stripping (Kenney & Young, 1989, Gunn & Gott, 1972). Both processes raise the molecular to atomic Hydrogen ratio since the HI is more widely distributed within the galaxies and more easily stripped. Interaction and merging are more common in rich clusters due to the large number density of galaxies. Neither ram pressure nor tidal stripping seem likely for NGC 5866, however. The NGC 5907 group probably lacks a dense intra cluster medium like that in the Virgo cluster to strip the gas away, but the group does provide neighbours with which NGC 5866 could interact.

The possibility of galaxy interaction needs to be explored in a more appropriate context than rich galaxy clusters like Virgo or Coma. Table 4.1 gives a list of known galaxies in the NGC 5907 loose group.

Table 4.1 The NGC 5907 group of galaxies. All information is from the Tully *Nearby Galaxies Catalogue* (1988).

Name NGC	Type	R.A. h m	Dec ° '	V_h kms^{-1}	Distance Mpc	D_{25} '	log L_B $L_\odot$	log M_{HI} $M_\odot$
(1)	(2)	(3)	(4)	(5)	(6)	(7)	(8)	(9)
5907	Sc	15 14.6	56 31	666	14.9	11.2	10.41	10.14
5866	S0	15 5.1	55 57	692	15.3	7.3	10.22	-
5879	Sbc	15 8.4	57 12	775	16.8	4.5	9.98	9.35
U 9776	Im	15 11.7	57 10	830	17.4	1.1	-	8.46
U 9769	Sdm	15 10.7	55 59	844	17.7	2.9	9.01	9.23

col. (1) name, col. (2) Hubble type, col. (3) & (4) right ascension and declination (epoch 1950), col. (5) systemic velocity, col. (6) distance, col. (7) the diameter at 25th magnitude/arcsecond^2 isophote in blue light, col. (8) log of the blue luminosity, col. (9) log of the HI mass

4.4.2 NGC 5907: A Well Studied Neighbour

The most thoroughly studied member of the NGC 5907 group is NGC 5907 itself, a nearly edge on (inclination = 86.5°, Dumke *et al.*, 1997) Sc galaxy. This was the first external galaxy found to have a warped HI disk (Sancisi, 1976), at first considered to be caused by some form of interaction (Hunter & Toomre, 1969). The HI warp is not a definitive sign of interaction, however. Recent studies have shown that a warped disk can form internally through stellar random motions (Sellwood, 1996), differential precession of gas in a non-spherical halo potential (New *et al.*, 1998) or by out flow winds from X-ray binaries or active galactic nuclei (Quillen, 2001). However, despite these internal mechanisms, interaction is still an attractive candidate for producing warps

in galactic gas disks. Sancisi (1976) mentions NGC 5866 as a possible interactor with NGC 5907 but points out that the event would have happened ~4 × 10^9 yrs ago based on the projected separation and relative velocity of the two galaxies (84' and ~100 kms^{-1}, respectively). Sancisi used a distance of 18 Mpc for NGC 5907, but adapting 14.9 Mpc does not alter the minimum actual separation enough to significantly change the age of the hypothetical interaction, which is larger than the expected survival time of the warp (Sancisi, 1976, and references therein).

The dwarf galaxy PGC 54419 is only 11'.5 from the centre of NGC 5907 and is situated 3'.7 from the tip of the warped atomic gas (Shang et al., 1998). This object seems like a more plausible candidate than NGC 5866 for the cause of the warp. At a distance of 14.9 Mpc, PGC 54419 is located ~50 kpc away from NGC 5907 and only ~16 kpc in projection from the warp.

Other evidence suggests that NGC 5907 is a cannibal. Lequeux et al. (1998) report that the halo of NGC 5907 is redder than the disk, implying that it is more metal rich. This is unexpected because it is generally believed that halo objects are old and relatively metal poor, like the globular clusters of our own galaxy. Red colours indicate 2nd generation, metal rich stars of intermediate age, like our sun, or many, low mass (≤0.15 M$_\odot$), old, metal-poor stars, more than can be explained using standard IMFs. Lequeux et al. (1998) suggest that the red halo is the remnant of a small, low mass elliptical galaxy which merged with NGC 5907 around 2 Gyr ago. They support their claim with an N-body simulation of a disk galaxy of mass 307 × 10^9 M$_\odot$ interacting with a 30.7 × 10^9 M$_\odot$

spherical companion. The simulation starts with the galaxies 32 kpc apart and with the companion in a near circular orbit with a velocity of 200 kms^{-1}. After 1.9 Gyr the parent galaxy has a warped disk, slightly tilted to its original plane. The stars of the smaller galaxy became distributed throughout the parent halo.

Another, less obvious sign cannibalism is the discovery of a faint stellar ring surrounding NGC 5907 with an inclination of 45° to the plane of the galaxy (Shang *et al.*, 1998), the first of its kind in an external galaxy. Similar stellar streams have been observed in the Milky Way and, recently, a similar discovery has been made on M31 (Ibata *et al.* 2001), arguing that this phenomena may be common for large galaxies. The ring around NGC 5907, is approximately the same size as the major axis of NGC 5907, and lacks detected gas. The authors propose that the ring is the remnant of a dwarf spheroidal galaxy that has been tidally disrupted by NGC 5907. The lack of detected gas could mean that the former companion itself had little gas, or that the gas has been redistributed throughout the NGC 5907 halo therefore is too tenuous to be seen by the reported observations (Shang *et al.*, 1998). A third possibility is that the gas has been added to that already present in the NGC 5907 disk.

There is thus ample evidence that NGC 5907 has interacted with other galaxies, making it not unreasonable to assume that NGC 5866 has done so also. The interstellar media of NGC 5907 and NGC 5866 share properties which suggest similar histories. Sofue (1994) reports that the molecular gas in NGC 5907 is located predominantly in the central 5 kpc region, in a ring-like distribution, similar to the molecular rings of M31, and also NGC

5866. A CO study by Garcia-Burillo *et al.* (1997) of the nuclear region of NGC 5907 finds that the molecular gas is rotating at ± 180 kms^{-1} in the inner 10" and that the CO brightness distribution is asymmetrical. Both of these findings are similar to those found for NGC 5866 in this work. Garcia-Burillo *et al.* claim that a portion of the molecular gas may be counter rotating; could this be the missing gas from the stellar ring found by Shang *et al.* (1998)? Due to the kinematical similarities between NGC 5866 and NGC 5907, and along with other corroborating evidence, such as the tilted dust lane, it is plausible to assume that NGC 5866's paucity of HI and its molecular gas kinematics can be explained by previous interaction.

In summary, it seems likely that the bright members of the NGC 5907 group have experienced gravitational interactions in the past. Indeed, even our own galaxy exhibits many of the same features indicating interaction, such as an HI warp and streams of cannibalized stars. These events are probably quite common even in relatively low density environments, and NGC 5866 has not been immune to them.

4.5 Conclusions

NGC 5866 is a gas rich lenticular galaxy, having the majority of its cool interstellar medium in the form of molecular gas. The gas appears to occupy a broken ring structure with several hot spots similar in size and mass to the giant molecular clouds of the Milky Way. The overall picture presented by the data is that NGC 5866 has retained much of the gas returned by its stars. The most reliable star formation rate, inferred from the Hα luminosity, implies that the interstellar medium is in mass balance. The S0 galaxy class

exhibits wide ranging values for any measurable or inferred quantity and so, on the whole, NGC 5866 appears fairly typical. There are several areas which need further study in order to confirm the former statement. The strange features in the spectra which could not be synthesized by the simple model used here, such as the extra signal seen in the 0,0 and 9-7 pointings (figures 3.6 and 3.7) need to be looked at again. An interferometric study of the nuclear region of NGC 5866 would provide the necessary resolution to ascertain the true nature of these anomalies. Also, the rotation of the ionized and molecular gas needs to be reconciled; a near IR study of NGC 5866 would be useful for this purpose. If near IR observations confirm the ionized gas rotation curve then much more study needs to be done on this galaxy in order to understand how the two components could be separated.

It is interesting that NGC 5866 should have roughly the amount of gas predicted by simple mass return arguments, yet still show many signs which indicate that it has gained or lost gas. Although the mass balance found here is intriguing, the simple nature of the calculation does not allow for solid conclusions. The fact that the molecular gas appears to be kinematically decoupled from the stars, that the M_{H_2}/M_{HI} mass ratio is higher than average, and that the dust lane is tilted, lead one to believe that the molecular gas in NGC 5866 is of external origin. The major arguments for an external origin of the gas is the rapid rotation of the molecular gas compared to the stars and the tilted dust lane. Even if the ionized gas is rotating in the same fashion as the molecular gas, the fact that the gas is rotating faster then the stars still poses a problem for any internal origin theory. This is compounded by the statistical results showing that gas is accreted onto lenticulars in a

substantial fraction of the cases observed (Bertola *et al.*, 1992). The kinematics suggest that if some form of interaction took place, it most likely happened on the order of 1 Gyr ago based on the evidence of a higher SFR in the distant past and the fact that there is no smoking gun left over from the event like a clear morphological distortion.

A search for potential companions would be useful, since any smaller galaxy found nearby might provide clues to the origin of the ISM in NGC 5866, should the companion show signs of interaction. Since the stellar rotation curve of Fisher (1997) shows no sign of two kinematically distinct major stellar populations, a recent major merger with another galaxy does not seem plausible, but this does not rule out cannibalization of an intergalactic cloud or smaller companion such as a gas-rich dwarf. If an accretion event has taken place then NGC 5866 should show other signs like those found in NGC 5907. Since it is edge on it should not be difficult to perform a colour analysis of its halo to see if it too exhibits the same red colour of NGC 5907. Signs like stellar streams or shells are hard to find in a distant galaxy but it has been done for NGC 5907. Again, a detailed colour analysis of off axis regions may prove fruitful in finding an independent population of stars. The fact that the detected ISM is molecular discounts accretion from a companion since most dwarf galaxies, like our Magellanic clouds, appear to be HI rich. Another line of tests might be to take a closer look at the nuclear region of NGC 5866. A more detailed kinematic map of the molecular gas would surely provide more clues as to its origin. A high sensitivity search for HI might prove useful as well. Perhaps the HI kinematics could corroborate any origin theory for the cool ISM.

Given the local environment, galaxy harassment might be the best option, since it does not require a merger but only a close encounter. This scenario is the most compatible with the results. The harassment would have taken place ~1 Gyr ago, as argued above. The HI at larger radii was stripped away, raising the molecular to atomic hydrogen ratio and leaving the remaining gas perturbed, rotating faster than the unaffected stars. The perturbation left the gas in a ring-like structure and caused a starburst episode in which the star formation rate declined to the present rate consistent with the low present day FIR luminosity to blue luminosity ratio. Since the cool ISM mass is so close to the value obtained from mass return arguments this might mean that NGC 5866 did not have very much atomic hydrogen in the first place or that the harassment simply caused the atomic hydrogen to be converted into H_2 via a pressure increase. This scenario would leave other traces that could still be found today. During the starburst period, the star formation rate would be ~40 $M_\odot$/yr (Icke, 1985). Assuming a relatively long starburst episode of ~100 Myr, approximately 1% of the stars in NGC 5866 would be a result of this starburst period. Any stars formed at this time would not be decoupled from the molecular gas since the gas that they formed out of was already perturbed. A very careful search for this population might prove fruitful.

Chapter 5

Summary

In this work the cool ISM of NGC 5866 is investigated through the analysis of multiple

pointing ^{12}CO J=1-0 data. Several solid conclusions can be made about the molecular

ISM from these data. The results are summarized in point form below.

1. The molecular Hydrogen mass is found to be $4.55 \pm 0.43 \times 10^8$ M$\odot$ which reveals a

cool ISM mass of $\sim 6.4 \times 10^8$ M$\odot$ when the molecular gas mass is scaled up to include

Helium.

2. The molecular gas in NGC 5866 is distributed asymmetrically in a broken Gaussian

ring with a radius of ~ 1.1 kpc. Giant molecular clouds, analogous to those found in the

Milky Way are inferred to be located mostly on the redshifted side of the galaxy space.

3. The molecular gas is rotating rapidly with a maximum rotation speed of 305 kms^{-1}. This is on the order of 100 kms^{-1} faster than previously published rotation speed values for the stars and the ionized gas in NGC 5866 (Fisher, 1997).

4. The gas appears to be in mass balance based on a mass return rate of ~0.1 M☉/yr and a gas consumption rate via star formation of ~0.047 M☉/yr.

5. Several lines of evidence point to an external origin for the molecular gas. A high value of M_{H2}/M_{HI} = 3.5, kinematically decoupled stars and gas, evidence for a larger star formation rate in the past and the tilted dust lane all point to an external origin of, or at least influence on, the cool ISM.

6. The observed and inferred properties of the cool ISM can be consistently explained by a galaxy harassment event on the order of a billion years ago.

7. Future work should include an interferometric study of the nuclear region in order to pin down the source of the strange, unexplained spectral features along with near IR observations. The near IR observations are also needed to reconcile the molecular and ionized gas kinematics. Careful photometric study of the stars and a high sensitivity search for faint companions might also provide corroborating evidence to any external origin theory.

Appendix A

COSPEC Source Code

The following lists the COSPEC source code, written in FORTRAN. The line numbers were added to the code in this appendix in order to reference different parts of the code in appendix B. COSPEC was originally written by D. Welch and G. Welch for work on the lenticular galaxy, NGC 4710, and was later extensively modified by the author for work on NGC 5866. Many of the modifications were made to make the program universal an not exclusive to any one particular object. The only remaining parameter which needs to be changed in the source code for future work is the velocity dispersion relation to radius (lines 649 only). This relation is specific to NGC 5866. The continuous numbers aligned to the left are used a reference in appendix B. Numbers referred to in the body of the code are independent of the numbers to the left.

```
1          PROGRAM COSPEC      AUGUST 31 2001
2     C
3     C Written by: D. Welch in JAN 1993
4     C Modified by G. Welch in APR 1993 to incorporate up to 10 cloud
5     C complexes which are brighter than surrounding disk.  These
6     C complexes are referred to as "clouds".
7     C
8     C Modified by A. LeBlanc in 2000/2001. The program has been made
9     C more general for work on the S0 galaxy NGC 5866, but is not
10    C specific to it.  The program now allows for different sized
11    C disks or rings (input in ") with various different intensity
12    C profiles.  The 'IRAM 30m telescope' PP can be pointed anywhere
13    C along the major axis, or at an angle to the major axis for
14    C either the CO J=2-1 or CO J=1-0 transition.  Other additions
15    C include a graphing subroutine creates a spectra using pgplot,
16    C a variable rotation curve, multiple pointing data, variable
17    C cloud sizes and a velocity dispersion component.
18    C
19    C Purpose: To model the profile of CO emission line produced by
20    C an inclined rotating thin disk or ring.
21    C
22    C Comments:The disk has radius ROUTER, is viewed at angle TIP
23    C relative to its face.  It is assumed that the disk comprises a
24    C large number of optically thick CO clouds.  No cloud shadows
25    C another, so all clouds are seen regardless of the tip angle
26    C of the disk.
27    C
28    C UNITS: The internal distance unit is the "cu" = COSPEC unit.
29    C The radius of the disk is set at 100 cu.  Angles in degrees.
30    C
31    C INTENSITIES:The intensity unit is the central intensity of the
32    C disk.
33    C
34    C This program is called by typing:
36    C f77 -o 'currentname' pgplot, which displays
35    C the output. It must be complied 'currentname'.f -lpgplot -lX11
37    C
38    C ***************************************************************
39    C
40    C Array RINOBS will hold the intensity for each bin of DVEL km/s
41    C width for a total velocity range of + or - DVEL*200 km/s.
42    C
43          EXTERNAL TELSENS, FUNCTION1
44          REAL RINOBS (410), RVEL, RCLOUD(10,3), AZCLOUD(10,3)
45          REAL RINTCL(10), RVELG (410), RING
46          REAL FUNCTION1, CLEDGE(20)
47          REAL RINOBSG (410), RVELG2 (410), RINOBSG2 (410)
48          REAL CONV, ARCDISC, OFFSET, AZCE, TRUNC, TOP
49          REAL TURNVEL, TURNRAD, TURNRADCU, FWHM, GRR, LBASE, CLH
50          REAL SEED1, SEED2, GAUSSDEV, VDIS, NORM
51          REAL CLSIZE (10)
52          LOGICAL NOSHIFT, AZBACK, AZAHED, BEAM, TRANS21, DISK
53          LOGICAL VD, CLOUDS, RINGS, ROTCUR
54          CHARACTER NEXT, MODEL, DISKMOD, RINGMOD, PICPICK
55          CHARACTER*12 FILENAME
56          CHARACTER*80 TEXT
57          INTEGER*2 IRAD, I, J, IVEL, INUM, IFIRST, ILAST, ISTART
```

```
58          INTEGER IDC(10), IC(20), N, T, M, B, O, G
59    C
60    C Ask for input data.
61
62    C The following constitute the standard parameters:
63    C
64    C Note that the exponential scale length, DS, is expressed
65    C as a fraction of the disk radius, whereas the FWHM used in
66    C Gaussian profiles is expressed as a fraction of the disk
67    C diameter.
68    C
69    C
70          TIP = 90               ! 90 degrees for edge-on disk
71          TOP = 0    ! angle the PPcenter to the disk major axis
72          VELCON = 305      ! rotational velocity at disk edge (km/s)
73          VELOBJ = 745         ! systemic velocity (km/s)
74          CLOUDS = .FALSE.  ! including clouds or not, default in no
75          BEAM = .TRUE.     ! power pattern on or off, default is on
76          ARCDISC = 60         ! disk diameter (")
77          OFFSET = 0 !PP offset from the centre disk major axis (")
78          TRANS21 = .FALSE.   ! transition, default is CO J=1-0
79          TURNVEL = 200    ! the kink vel. in the rot. curve (km/s)
80          TURNRAD = 10     ! the kink radius in the rotation curve (")
81          DISK = .TRUE.       ! disk model? default is yes
82          RINGS = .FALSE.     ! ring model (R.M.)? default is no
83          DVEL = 10.4         ! spectrum bin size (km/s)
84          VD = .FALSE.        ! velocity dispersion default is off
85          DISKMOD = 'c' !what kind of disk model, default is constant
86          RINGMOD = 'c'        !this is the R.M. type
87          NORM = 22.1    ! area used to normalize the models (T km/s)
88          ROTCUR =.FALSE. ! display the rotation curve data or not
89
90    C the following standard parameters are included so that user
91    C can change the model type form a constant intensity disk
92    C and only recompile once.  The values below are included as an
93    C example. When changing the standard model from disk to ring
94    C DISK must = .FALSE. and RINGS must = .TRUE.  The opposite is
95    C true when changing the model back from a ring to a disk.
96    C
97    C
98          FWHM = .5  ! FWHM expressed as a fraction of the disk size
99          GRR = 15   ! Gaussian ring radius, "
100         DS = .45   ! scale length of (exponential) disk brightness
101         RING = 15  ! ring radius, constant intensity, "
102         TRUNC = 10 ! inner radius where Gaussian is truncated, "
103   C
104   C ensured that CONV is specified. All input in " rely on CONV to
105   C convert to computer units.
106   C
107         CONV = ARCDISC/200
108         TURNRADCU = TURNRAD/CONV
109         NCLOUD = 0
110   C
111   C
112   C  These lines ensure the proper values are written to the
113   C  screen when changing the standard input model from a constant
114   C  intensity disk.
```

```
115    C
116           IF (RINGS) THEN
117           FWHM2= FWHM*CONV*200
118           GRR2= GRR
119           TRUNC2 = TRUNC
120           END IF
121           IF ((DISK) .AND. DISKMOD .EQ. 'g') THEN
122           DS2= DS*ARCDISC/2
123           FWHM2= FWHM*CONV*200
124           END IF
125    C
126    C
127    C
128    C B, O are triggers, later in the code they may become 1 and a
129    C print is or is not longer called (they are for table headings)
130    C G is a counter.
131    C
132           B = 0
133           O = 0
134           G = 0
135    C
136    C the standard parameters are written to the screen and the user
137    C may change any of them, more than once (i.e. if a mistake is
138    C made, simply ask to change the value again) at run time.
139    C
140    C
141           PRINT*, ' '
142           PRINT*, '                ******************************'
143           PRINT*, '                * THE STANDARD PARAMETER SET *'
144           PRINT*, '                ******************************'
145    39     IF (O .EQ. 1) Then
146           PRINT*, ' '
147           PRINT*, '                ******************************'
148           PRINT*, '                * THE MODIFIED PARAMETER SET *'
149           PRINT*, '                ******************************'
150            ELSE
151            CONTINUE
152            END IF
153           PRINT*, ' '
154           IF ((DISK) .AND. DISKMOD .EQ. 'c') PRINT*, 'a) MODEL =
155           2 CONSTANT INTENSITY DISK'
156           IF ((DISK) .AND. DISKMOD .EQ. 'e') PRINT*, 'a) MODEL =
157           2 EXP DISK, SCALE LENGTH = ', DS2,' "'
158           IF ((DISK) .AND. DISKMOD .EQ. 'g') PRINT*, 'a) MODEL =
159           2 GAUSSIAN DISK, FWHM = ', FWHM2,'"'
160           IF ((RINGS) .AND. RINGMOD .EQ. 'c') PRINT*, 'a) MODEL =
161           2 CONSTANT INTENSITY RING Of RADIUS', RING, '"'
162           IF ((RINGS) .AND. RINGMOD .EQ. 'g') PRINT*, 'a) MODEL =
163           2 GAUSS RING, RADIUS = ', GRR2, '" FWHM =', FWHM2,'"'
164           IF ((RINGS) .AND. RINGMOD .EQ. 't') PRINT*, 'a) MODEL =
165           2 TRUNC. GAUSS RING   RADIUS = ',  GRR2, '" FWHM =',
166           2FWHM2, '"',' INNER TRUNC RAD = ', TRUNC2, '"'
167
168           PRINT*, ' '
169           IF (CLOUDS) THEN
170           PRINT*, 'b) CLOUDS? = YES'
171           ELSE
```

```
172        PRINT*, 'b) CLOUDS? = NO'
173        END IF
174        PRINT*, ' '
175        PRINT*, 'c) TIP = ', TIP, ' degrees
176        2The inclination on the sky'
177        PRINT*, ' '
178        PRINT*, 'd) TOP = ', TOP, ' degrees
179        2The angle with respect to the power pattern axis'
180        PRINT*, ' '
181        PRINT*, 'e) ARCDISC = ', ARCDISC, ' "   The disk diameter'
182        PRINT*, ' '
183            PRINT*, 'f) VELOBJ = ', VELOBJ, ' km/s  The systemic
184        2velocity'
185        PRINT*, ' '
186            PRINT*, 'g) VELCON = ', VELCON, ' km/s  The disk edge
187        2rotational velocity'
188        PRINT*, ' '
189        PRINT*, 'h) TURNRAD = ', TURNRAD, ' "  Regime change
190        2 radius in the rotation curve'
191        PRINT*, ' '
192        PRINT*, 'i) TURNVEL = ', TURNVEL, ' km/s  Regime change
193        2velocity in the rotation curve'
194        PRINT*, ' '
195            IF (BEAM) THEN
196            PRINT*, 'j) POWER PATTERN ON? = YES'
197            ELSE
198            PRINT*, 'j) POWER PATTERN ON? = NO'
199        END IF
200        PRINT*, ' '
201        PRINT*, 'k) OFFSET = ', OFFSET, ' "  Power pattern offset.
202        2 If no PP, this is ignored'
203        PRINT*, ' '
204        IF (TRANS21) THEN
205        PRINT*, 'l) CO transition : J=2-1'
206        ELSE
207        PRINT*, 'l) CO transition : J=1-0'
208        END IF
209        PRINT*, ' '
210        PRINT*, 'm) DVEL =', DVEL, ' km/s  the spectrum bin size'
211        PRINT*, ' '
212        IF (VD) THEN
213        PRINT*, 'n) VELOCITY DISPERSION ON? = YES'
214        ELSE
215        PRINT*, 'n) VELOCITY DISPERSION ON? = NO'
216        END IF
217        PRINT*, ' '
218        PRINT*, 'o) AREA USED FOR NORMALIZATION =', NORM, ' T km/s'
219        PRINT*, ' '
220        IF (ROTCUR) THEN
221        PRINT*, 'p) DISPLAY ROTATION CURVE DATA? = YES'
222        ELSE
223        PRINT*, 'p) DISPLAY ROTATION CURVE DATA? = NO'
224        END IF
225        PRINT*, ' '
226        PRINT*, ' '
227        PRINT*, '            You have made', G,' changes to the
228        2parameter set'
```

```
229        PRINT*, ' '
230        PRINT*, '     **********************************************
231   2**************'
232        PRINT*, '     * IF THIS IS FINE, TYPE LOWER CASE "y", IF
233   2NOT, INPUT THE *'
234        PRINT*, '     *LOWER CASE LETTER NEXT TO THE QUANTITY YOU
235   2WANT TO CHANGE*'
236        PRINT*, '     *
237   2                         *'
238        PRINT*, '     * ---> WARNING: If changing ARCDISC,
239   2do so first  <---  *'
240        PRINT*, '     ********************************************
241   2****************'
242        READ*, NEXT
243        IF (NEXT .NE. 'y') G = G + 1
244        IF (NEXT .EQ. 'a') GOTO 79
245        IF (NEXT .EQ. 'b') GOTO 12
246        IF (NEXT .EQ. 'c') GOTO 85
247        IF (NEXT .EQ. 'd') GOTO 84
248        IF (NEXT .EQ. 'e') GOTO 57
249        IF (NEXT .EQ. 'f') GOTO 83
250        IF (NEXT .EQ. 'g') GOTO 82
251        IF (NEXT .EQ. 'h') GOTO 86
252        IF (NEXT .EQ. 'i') GOTO 87
253        IF (NEXT .EQ. 'j') GOTO 50
254        IF (NEXT .EQ. 'k') GOTO 89
255        IF (NEXT .EQ. 'l') GOTO 88
256        IF (NEXT .EQ. 'm') GOTO 81
257        IF (NEXT .EQ. 'n') GOTO 77
258        IF (NEXT .EQ. 'o') GOTO 69
259        IF (NEXT .EQ. 'p') GOTO 76
260        IF (NEXT .EQ. 'y') GOTO 56
261
262   C
263   C The size of the disc is input in arcseconds (ARCDISC). This is
264   C then used to calculate the ratio of arcsecond to cu (computer
265   C units, see above). This ratio is CONV ("/cu). This ratio is
266   C used throughout in order to convert input value into thosethat
267   C can be understood by the program (i.e it puts everything into
268   C computer units, cu.This is paramount and is the reason for the
269   C warning atruntime thatif the disksize is going to be changed,
270   C change it first as many other quantities depend on the value of
271   C CONV which is dependent on the disk size. the OFFSET is the
272   C center position of the power pattern.  It is in input in
273   C arcseconds and is input as negative when on the side of the
274   C center of the disc which is rotating away from the line of
275   C sight (larger velocities) and is input as positive(center is 0)
276   C for an offset on the side ofthe disc which is rotating into the
277   C line of sight (lower velocities).  These values are used by the
278   C power pattern function, TELSENS for CO J=2-1 or TELSENS2
279   C for CO J=1-0.
280   C
281
282
283   57     PRINT *, 'input the disc size in arc seconds'
284          READ *, ARCDISC
285          CONV = ARCDISC/200
```

```
286        O = 1
287        GOTO 39
288   89   PRINT *, 'Set offset along the major axis in arcseconds'
289        READ *, OFFSET
290        O =1
291        GOTO 39
292   88   TRANS21 = .TRUE.
293        PRINT *, 'for CO J=1-0 type y, for CO J=2-1 type n'
294        READ *, NEXT
295        IF (NEXT .EQ. 'Y' .OR. NEXT .EQ. 'y') TRANS21 = .FALSE.
296          O = 1
297          GOTO 39
298   87   PRINT*, 'input the "kink" velocity (km/s) in the rotation
299        2curve'
300        PRINT*, 'for no kink input the max. rot. velocity'
301        READ*, TURNVEL
302        O = 1
303        GOTO 39
304   86   PRINT*, 'input the "kink" radius (") in the rotation curve'
305        PRINT*, 'for no kink input 1/2 the disk size in "'
306        READ*, TURNRAD
307        TURNRADCU = (TURNRAD/CONV)
308        O = 1
309        GOTO 39
310   85   PRINT *, 'Input disk inclination in degrees (0 is face-on)'
311        READ *, TIP
312        O = 1
313        GOTO 39
314   82   PRINT *, 'Input disk edge rotational velocity in km/s.'
315        READ *, VELCON
316        O = 1
317        GOTO 39
318   83   PRINT *, 'Input systemic velocity in km/s.'
319        READ *, VELOBJ
320        O = 1
321        GOTO 39
322   84   PRINT *, 'Input disk inclination in degrees with respect
323        2to the power pattern axis'
324        PRINT *, '0 = the power pattern axis and the major axis
325        2of the disk are aligned'
326        READ *, TOP
327        O = 1
328        GOTO 39
329   81      PRINT*, 'Input the desired bin size in km/s'
330        READ*, DVEL
331        O = 1
332        GOTO 39
333   69      PRINT*, 'Input the normalization area in T km/s'
334          READ *, NORM
335        O = 1
336        GOTO 39
337   76      PRINT*, 'Display the rotation curve data? (y/n)'
338          READ*, NEXT
339          IF (NEXT .EQ. 'y') THEN
340        ROTCUR = .TRUE.
341        O = 1
342        GOTO 39
```

```
343          ELSE
344          GOTO 39
345          END IF
346   C
347   C Ask about clouds.
348   C
349   12      CLOUDS = .FALSE.
350          PRINT *, ' Include clouds ("y" or "n")?'
351          READ *, NEXT
352          IF (NEXT .EQ. 'n' .OR. NEXT .EQ. 'N') THEN
353          NCLOUD = 0
354          GOTO 39
355          END IF
356          PRINT *, ' '
357          PRINT *, 'Read cloud parameters from disk file ("y"/"n")?'
358          READ *, NEXT
359          IF (NEXT .EQ. "y" .OR. NEXT .EQ. "Y") GOTO 20
360   C
361   C Accept cloud parameters from the console
362   C
363          PRINT *, ' '
364          PRINT *, ' NOW INPUT INFORMATION ON ANY CLOUDS PRESENT'
365          PRINT *, ' '
366          PRINT *, ' Number of clouds (1 - 10)?'
367          READ *, NCLOUD
368          IF (NCLOUD .EQ. 0) GOTO 12
369          IF (NCLOUD .GT. 1) PRINT*, 'ENTER IN CLOUDS IN ORDER OF
370          2INCREASING RADIAL POSITION'
371          Print*, ' '
372          DO 15 N = 1, NCLOUD
373          PRINT *, 'Radial position of cloud', N, ' as a fraction
374          2of disk radius?'
375          READ *, RCLOUD (N,1)
376          PRINT *, 'Azimuth of this cloud in degrees (0 - 360)?'
377          READ *, AZCLOUD (N,1)
378          PRINT*, ' Intensity of this cloud?' !centre has unit int.
379          READ *, RINTCL (N)
380          PRINT *, ' Input cloud size in cu.  Disk is 100 cu in
381          2radius'
382   15     READ *, CLSIZE (N)
383          GOTO 16
384   16     IF (NCLOUD .GT. 0) CLOUDS = .TRUE.
385          PRINT*, 'DISPLAY A PICTURE OF THE CLOUD POSITIONS? (y/n)'
386             READ*, PICPICK
387             IF (PICPICK .EQ. 'y') THEN
388             CALL CLOUDPIC(NCLOUD, CLSIZE, RINTCL, RCLOUD, AZCLOUD)
389             O = 1
390             GOTO 39
391             ELSE
392             O = 1
393             GOTO 39
394             END IF
395   C
396   C Read cloud parameters from existing disk file "clparam.dat"
397   C
398   C    Below is an example of how "clparam.dat" should be set up in
399   C order to work Assume that the Cs are the edge of the text box.
```

```
400   C
401   CNUMBER OF CLOUDS ON NEXT LINE
402   C 10
403   C  RCLOUD AZCLOUD RINTCL CLSIZE
404   C .5       91       0      10.0
405   C .5       79       0      10.0
406   C .18      0        2      12.0
407   C .1       180      2      6.6
408   C .28      180      7      7.0
409   C .72      180      3      9.0
410   C .9       139      0      20.0
411   C .9       221      0      20.0
412   C .5       139      0      9.0
413   C .5       221      0      9.0
414   C
415   C
416      20 FILENAME = 'clparam.dat'
417         OPEN (UNIT=8, FILE=FILENAME)
418         READ (UNIT=8, FMT=28) TEXT ! Read 1st LINE - not used
419         READ (UNIT=8, FMT=29) NCLOUD
420         READ (UNIT=8, FMT=28) TEXT ! Read column headings- not used
421         PRINT *, ' '
422         PRINT *, ' There are ', NCLOUD, ' clouds in this file'
423      28 FORMAT (A80)
424         PRINT *, ' '
425      29      FORMAT (2X, I2)
426         GOTO 33
427      33 DO 35 N = 1, NCLOUD
428         NCL = N
429         READ (8,*, END=35) RCLOUD(N,1), AZCLOUD(N,1),
430         2RINTCL(N), CLSIZE(N)
431      35 CONTINUE
432         GOTO 42
433
434   C After a successful read, print out the parameters
435   C
436      42 PRINT *, ' '
437         PRINT *, ' THE FOLLOWING CLOUD PARAMETERS WILL BE USED'
438         PRINT *, ' '
439         PRINT *, '  RADIUS  AZIMUTH  INTENSITY  SIZE'
440         PRINT *, ' '
441         DO 44, N = 1, NCLOUD
442      44 PRINT 45, RCLOUD(N,1), AZCLOUD(N,1), RINTCL(N), CLSIZE(N)
443      45 FORMAT (2X, F5.3, 4X, F4.0, 6X, F5.2, 4X, F5.2)
444         PRINT *, ' '
445         PRINT *, ' '
446         PRINT *, ' Use these clouds ("y" or "n")?'
447         READ *, NEXT
448         IF (NEXT .EQ. "n" .OR. NEXT .EQ. "N") GOTO 12
449         GOTO 16
450
451      50 PRINT *, ' '
452         PRINT *, ' Turn on tapering by telescope main beam?
453         2"y" or "n". Default is "y" '
454         READ *, NEXT
455         IF (NEXT .EQ. 'y' .OR. NEXT .EQ. 'Y') THEN
456         BEAM = .TRUE.
```

```
457           GOTO 39
458       ELSE
459       BEAM = .FALSE.
460       O = 1
461       GOTO 39
462       END IF
463   C
464   C
465   79  RINGS = .FALSE.
466       DISK = .FALSE.
467       PRINT*, 'model a disk (d) or a ring (r) ?'
468       READ*, MODEL
469       IF (MODEL .EQ. 'D' .OR. MODEL .EQ. 'd')   GOTO 51
470       IF (MODEL .EQ. 'R' .OR. MODEL .EQ. 'r') GOTO 52
471   51  DISK = .TRUE.
472       PRINT*, 'how do you want to model the disk int. profile?'
473       PRINT*, 'constant (c), exponential drop off (e),
474       2or Gaussian (g) ?'
475       READ*, DISKMOD
476       PRINT*, DISKMOD
477       IF (DISKMOD .EQ. 'e') THEN
478       PRINT*, 'Input a fractional scale length'
479       READ*, DS
480       DS2= DS*ARCDISC/2
481       O = 1
482       GOTO 39
483       END IF
484       IF (DISKMOD .EQ. 'c') GOTO 39
485           IF (DISKMOD .EQ. 'g') PRINT*, 'input the FWHM as a
486       2fraction OF the disk size'
487           PRINT*, 'of the disk size, e.g. 0.5'
488           READ*, FWHM
489           FWHM = FWHM*200
490           FWHM2 = FWHM*CONV
491           O = 1
492           GOTO 39
493   52      RINGS = .TRUE.
494       PRINT*, 'how do you want to model the ring int. profile? '
495       PRINT*, 'constant (c), Gaussian (g), or truncated
496       2Gaussian (t) ?'
497       READ*, RINGMOD
498       IF (RINGMOD .EQ. 'g') GOTO 53
499       IF (RINGMOD .EQ. 'c') GOTO 54
500           IF (RINGMOD .EQ. 't') GOTO 53
501   53  PRINT*, 'input the radius at which the Gaussian is
502       2centered in " '
503       READ*, GRR2
504       GRR = GRR2/CONV
505       PRINT*, 'input the FWHM as a fraction of the disk
506       2size e.g. 0.5'
507       READ*, FWHM
508       FWHM = FWHM*200
509       FWHM2 = FWHM*CONV
510       IF (RINGMOD .EQ. 't') GOTO 61
511       O = 1
512       GOTO 39
513   54  PRINT*, 'input the inner radius of the ring in " '
```

```
514        READ*, RING
515        O = 1
516        GOTO 39
517   61   PRINT*, 'input the inner radius where the Gaussian
518        2will be truncated in "'
519        READ*, TRUNC2
520        TRUNC = TRUNC2/CONV
521        O = 1
522        GOTO 39
523   C
524   C
525   77   VD = .FALSE.
526        PRINT*, 'Do you want to add a velocity dispersion
527        2component? (y/n)'
528        READ *, NEXT
529        IF (NEXT .EQ. "y" .OR. NEXT .EQ. "Y") then
530        GOTO 78
531        ELSE
532        GOTO 39
533        END IF
534   78   VD = .TRUE.
535        PRINT*, 'Enter a seed for the random number generator'
536           READ*, SEED1
537        PRINT*, 'Enter a 2nd seed for the random number generator'
538        READ*, SEED2
539        O = 1
540        GOTO 39
541   C
542   C
543
544   56   PRINT *, ' .  Busy crunching - be back in a moment.'
545
546   C Zero the array which holds summed intensity across line profile.
547   C
548        DO 60 I = 1, 410
549              RINOBS (I) = 0.0
550      60 CONTINUE
551   C Set values for parameters.
552   C DVEL is the velocity width of each bin in the profile.
553   C
554   C    DVEL = 10.4
555   C
556   CRVEL1 is the velocity associated with the first stored intensity.
557   C
558        IF (VELCON .GE. TURNVEL) RVEL1 = VELCON - DVEL * 200
559        IF (VELCON .LT. TURNVEL) RVEL1 = TURNVEL - DVEL * 200
560   C Outer radius of disk is 100 cu.
561   C
562        ROUTER = 100.0
563   C
564   C R0 is the disk scale length in cu.
565   C
566        R0 = -DS * ROUTER
567   C
568   C DANG is the angular increment, set to 0.1 degree and
569   C expressed in radians.
570   C
```

```
571         DANG = 0.00174533
572   C
573   C SINTIP is the sine of the disk inclination angle.
574   C
575         SINTIP = SIND (TIP)
576   C
577   C RIO is the intensity per unit area at the centre of the disk.
578   C
579         RIO = 1.0
580   C
581         BINAREA = 0
582   CFind radial locations in cu of inner, outer edges of all clouds.
583   C
584         IF(NCLOUD .EQ. 0) GOTO 71
585   C     PRINT*, 'cloud', NCLOUD
586         DO 70 N = 1, NCLOUD
587               RCENTR = RCLOUD (N,1) * ROUTER
588               RCLOUD (N,3) = RCENTR + 0.5 * CLSIZE(N)
589               RCLOUD (N,2) = RCENTR - 0.5 * CLSIZE(N)
590   70     CONTINUE
591   71    CONTINUE
592   80    CONTINUE
593   C
594   C
595   CChoose number of annulitomake velocity increment DVA times DVEL.
596   C
597         DVA = 0.5
598         IF (VELCON .GE. TURNVEL) FANN = ANINT (VELCON / (DVA*DVEL))
599             IF (VELCON .LT. TURNVEL) FANN = ANINT
600         2(TURNVEL / (DVA*DVEL))
601   C     PRINT*, FANN    , VELCON    ,DVA    , DVEL
602   C
603   CFunction ANINT finds nearest integer, then converts it to a REAL
604   C Make sure that annuli have correct width.
605   C
606         DR = ROUTER / FANN
607         NANN = FANN
608         PRINT *, ' '
609         PRINT *, NANN, ' annuli of width ', DR, ' in solid body
610         2part'
611         PRINT *, ' '
612   C
613   C Now sum up intensities in this part of disk.
614   C
615   C     call pgbegin (0,'?',1,1)          !sets up pgplot to plot
616   C     call pgenv (-250.,250.,-40.,0.,0,1)   !to plot the PP
617   C     call pglab ('Ang. Distance','Intensity
618   C     2(dB)','Power Pattern')
619         DO 300 IRAD = 1, NANN
620   C     Calculate the radius to centre of annulus.
621               RADIUS = IRAD * DR - DR / 2.0
622   C
623   C   The rotation curve is solid body with allowances for a kink
624   C
625
626         IF (RADIUS .LE. TURNRADCU) THEN
627         V = -(TURNVEL/TURNRADCU) * RADIUS
```

```
628           ELSE
629           V = (-((VELCON - TURNVEL)/(ROUTER-TURNRADCU)) * RADIUS) -
630           2(VELCON - (((VELCON-TURNVEL)/(ROUTER-TURNRADCU))*ROUTER))
631           END IF
632
633
634  99    IF (ROTCUR) THEN
635          IF (B .EQ. 0) PRINT*, ' RADIUS (") ', 'VELOCITY (km/s)'
636          B = 1
637          PRINT*, RADIUS*CONV   , V
638          ELSE
639          CONTINUE
640          END IF
641  C
642  C this line in the velocity dispersion function.  it gives the
643  C average value of the velocity dispersion at a given radius.
644  C This is work specific and should be changed and the code
645  C recompiled based on specific data.  The average velocity
646  C dispersion value is used in a Gaussian random number generator
647  C (see GAUSSDEV function)
648  C
649              VDIS = 118-(2.93*RADIUS*CONV)
650  C
651  C DAREA is the area of the present chunk of the current annulus.
652              DAREA = RADIUS * DR * DANG
653  C
654  CBelow are the 5 choices of intensity profile chosen at run time.
655  CFrom top to bottom the profiles are flat disk, exponential disk,
656  C Gaussian disk, flat ring, Gaussian ring.  FUNCTIONS 1-4 can be
657  C found at the end of the code.  They make a flat profile into
658  C the specified profile.  (note that flat disk has nothing done
659  C to it i.e. no FUNCTION)
660  C
661          IF (DISK) THEN
662              IF (DISKMOD .EQ. 'c') RINTNO = RIO
663              IF (DISKMOD .EQ. 'e') RINTNO = RIO *
664          2FUNCTION1(RADIUS, R0)
665              IF (DISKMOD .EQ. 'g') RINTNO = RIO *
666          2FUNCTION2(FWHM, RADIUS)
667          ELSE
668              IF (RINGMOD .EQ. 'c') RINTNO = RIO *
669          2FUNCTION3(RING, CONV, RADIUS)
670              IF (RINGMOD .EQ. 'g') RINTNO = RIO *
671          2FUNCTION4(FWHM,
672          2RADIUS, GRR)
673              IF (RINGMOD .EQ. 't') RINTNO = RIO *
674          2FUNCTION5(RADIUS, TRUNC, GRR, FWHM)
675          END IF
676
677  C Test for clouds.
678          IF (NCLOUD .EQ. 0) GOTO 115
679  C
680  C Identify clouds included in this annulus.  Use array IDC to
681  C store locations of any such clouds in arrays RCLOUD, RINTCL,
682  C AZCLOUD for later use.
683  C
684          NHERE = 0
```

```
685              DO 110 N = 1, NCLOUD
686                  IF (RCLOUD(N,2) .LT. RADIUS .AND. RADIUS .LE.
687         2            RCLOUD(N,3)) THEN
688                  NHERE = NHERE + 1
689                  IDC (NHERE) = N
690                  END IF
691     110          CONTINUE
692     C
693     C
694              IF (NHERE .GT. 0) GOTO 130
695     C
696     C No clouds found in this annulus.
697     115          CONTINUE
698     C    Loop through 3600 angular chunks of current annulus.
699                  DO 120 J = 1, 3600
700                  REALJ = FLOATI (J)
701     C  Find component of disk velocity along line of sight.
702     C
703     C this section of the code adds a velocity dispersion element to
704     C the velocity given by the rotation curve.  See comments in the
705     C GAUSSDEV function
706     C
707                  VDIS2 = VDIS * GAUSSDEV(VD, SEED1, SEED2)
708     C             PRINT*, VDIS2
709                  V2 = V+VDIS2
710                  VTOOBS = V2 * COSD (REALJ / 10.0) * SINTIP
711     C Find bin number for this velocity, to nearest integer.
712                  IVEL = ININT ((VTOOBS - RVEL1) / DVEL)
713     C
714     C Calculate intensity contributed by this chunk.  Factor in
715     C the telescope beam if this switch is on.  The transition is
716     C specified when the program is run.  The PP for the CO J= 2-1
717     C is factored in by the subroutine TELSENS and the CO J=1-0 is
718     C factored in by TELSENS2.  See comments in the subroutines.
719                  RINTEN = RINTNO * DAREA
720                  IF (TRANS21) THEN
721                  IF (BEAM) RINTEN= RINTEN * TELSENS(RADIUS,
722         2                REALJ, TIP, OFFSET, CONV, TOP)
723                  ELSE
724                  IF (BEAM) RINTEN= RINTEN * TELSENS2(RADIUS,
725         2                REALJ, TIP, OFFSET, CONV, TOP)
726                  END IF
727     C         Add it to the appropriate bin.
728                  RINOBS (IVEL) = RINOBS (IVEL) + RINTEN
729
730     120          CONTINUE
731              GOTO 300
732     C
733     C    Reintroduction of the cloud code.  1 of 2
734     C
735     C Deal with any clouds found in this annulus.  First find edges
736     C of all the clouds in azimuthal direction.
737     C
738     130      DO 140 NH = 1, NHERE
739                  LBASE = ABS((100*RCLOUD(IDC((NH)),1))-RADIUS)
740                  CLH = SQRT(ABS(((0.5*CLSIZE(IDC(NH)))*
741         2(0.5*CLSIZE(IDC(NH))))-(LBASE*LBASE)))
```

```
742              AZCE = ATAN(CLH/RADIUS)*57.296
743              AZCLOUD(IDC(NH),3) = AZCLOUD(IDC(NH),1) +
744         2            AZCE
745              AZCLOUD(IDC(NH),2) = AZCLOUD(IDC(NH),1) -
746         2            AZCE
747  C     PRINT *, ' AZCLOUD values for annulus ', IRAD
748  C     PRINT *, AZCLOUD (IDC(NH),2), AZCLOUD (IDC(NH),3)
749  C     PRINT *, ' '
750
751  C NOTE: This procedure treats clouds as having the same linear
752  C extent in azimuth across their radial extent; they are not
753  C "pie-shaped".
754  C
755              NN = 2*NH - 1
756              CLEDGE(NN) = AZCLOUD(IDC(NH),2)
757              CLEDGE(NN+1) = AZCLOUD(IDC(NH),3)
758     140          IC(NN) = IDC(NH)
759  C
760  C Last statement saves original location of this cloud for
761  C use in intensity calculation. Now sort contents of array
762  C CLEDGE to put its entries in order of increasing azimuth.
763  C This makes it easier to work around the annulus.  It is
764  C assumed that clouds do not overlap.
765  C
766          NOSHIFT = .TRUE.
767          IF (NHERE .EQ. 1) GOTO 151
768          DO 150 NH = 1, NHERE
769              NE = NHERE - 1
770              DO 145 N = 1, NE
771                  NN = 2*N - 1
772                  IF (CLEDGE(NN) .GT. CLEDGE(NN+2)) THEN
773                  T1 = CLEDGE(NN)
774                  T2 = CLEDGE(NN+1)
775                  IT3 = IC(NN)
776                  CLEDGE(NN) = CLEDGE(NN+2)
777                  CLEDGE(NN+1) = CLEDGE(NN+3)
778                  IC(NN) = IC(NN+2)
779                  CLEDGE(NN+2) = T1
780                  CLEDGE(NN+3) = T2
781                  IC(NN+2) = IT3
782                  NOSHIFT = .FALSE.
783                  END IF
784  C          PRINT *, ' Azimuths of edges in degrees are:'
785  C              DO 156 M = 1, NHERE
786  C156              PRINT 2011, CLEDGE(2*M-1), CLEDGE(2*M)
787  C 2011            FORMAT ( 10X, F8.3, 2X, F8.3)
788     145              CONTINUE
789              IF (NOSHIFT) GOTO 151
790     150      CONTINUE
791     151      CONTINUE
792  C
793  C Fill unused elements of array CLEDGE with large values.
794  C This enables later recognition of no-more-clouds during
795  C summation around annulus.
796  C
797          IF (NHERE .EQ. 10) GOTO 154
798          DO 153 M = 2*NHERE+1, 20
```

```
799     153      CLEDGE(M) = 990.0
800   C
801   C Test for a valid sequence of cloud edge locations in array
802   C CLEDGE.  The positions should monotonically increase, and
803   C no two should be the same.  Check for clouds which hang
804   C over the zero of azimuth.  First, does lowest-azimuth cloud
805   C extend across AZ = 0?
806   C
807     154      AZBACK = .FALSE.
808         IF (CLEDGE(1) .LT. 0.0) AZBACK = .TRUE.
809   C
810   C Now does highest-azimuth cloud hang over AZ = 0?
811   C
812         AZAHED = .FALSE.
813         IF (CLEDGE(2*NHERE) .GT. 360.0) AZAHED = .TRUE.
814   C Holler if array CLEDGE is not well-ordered.
815         MUP = 2*NHERE - 1
816         DO 160 M = 1, MUP
817          IF (CLEDGE(M) .GT. CLEDGE(M+1)) THEN !line change:GE to GT
818           PRINT *, ' Problems with cloud locations in annulus',
819          2 IRAD
820   C           PRINT *, ' Azimuths of edges in degrees are:'
821   C               DO 155 N = 1, NHERE
822   C 155                PRINT 2010, CLEDGE(2*N-1), CLEDGE(2*N)
823   C 2010             FORMAT ( 10X, F8.3, 2X, F8.3)
824             STOP  'THUD!'
825           END IF
826     160      CONTINUE
827         IF(AZBACK .AND. AZAHED) THEN
828         PRINT *, ' First and last clouds in annulus', IRAD,
829         2' seem to overlap'
830         STOP  'CRASH'
831         END IF
832   C
833   C If first cloud overhangs AZ=0 begin summation at its first
834   C edge, at AZ < 0.  Change from original code (NINT)
835   C
836         OFFSETCL = 0.0
837         IF (AZBACK) OFFSETCL = NINT(CLEDGE(1))
838   C
839   C the above change keeps the angular increments integer values
840   C like the annuli with no clouds.  Without it you get slightly
841   C different intensities on a bin by bin basis which should be
842   C the same. Instead of starting at 1 you start at some negative
843   C real angle (i.e. start -22.18, next increment -21.18 etc... )
844   C and so all intensities are slightly different.  Same applies
845   C for below
846   C
847   C If last cloud overhangs AZ=0 begin summation just beyond its
848   C trailing edge, at AZ > 0.
849   C
850          IF (AZAHED) OFFSETCL= NINT(CLEDGE(2*NHERE))-360.0
851   C
852   C Now enter loop to sum around this annulus.
853   C
854         NH = 1
855         DO 200 J = 1, 3600
```

```
856                REALJ = FLOATI(J) + OFFSETCL*10.0
857                VTOOBS = V * COSD(REALJ/10.0) * SINTIP
858                IVEL = ININT((VTOOBS - RVEL1) / DVEL)
859                IF (REALJ/10.0 .GE. CLEDGE(NH)) THEN
860                     IF (REALJ/10.0 .LT. CLEDGE(NH+1)) THEN
861                     RINT = RINTCL(IC(NH))
862                     GOTO 170
863                     ELSE
864                     RINT = RINTNO
865                     NH = NH + 2
866                     END IF
867              ELSE
868              RINT = RINTNO
869              END IF
870      170          RINTEN = RINT * DAREA
871              GOTO 171
872      171          IF (TRANS21) THEN
873                     IF (BEAM) RINTEN= RINTEN * TELSENS(RADIUS,
874        2                      REALJ, TIP, OFFSET, CONV, TOP)
875                     ELSE
876                     IF (BEAM) RINTEN = RINTEN *
877        2            TELSENS2(RADIUS, REALJ, TIP, OFFSET, CONV,
878          2 TOP)
879                     END IF
880              RINOBS(IVEL) = RINOBS(IVEL) + RINTEN
881      200      CONTINUE
882    C
883    C Program skips to Statement 300 if no clouds present in this
884    C annulus.
885    C
886    C
887      300      CONTINUE
888    C   call pgend
889    C
890      600      DO 620 I = 1, 410
891              ISTART = I
892    C         PRINT*, 'I'  , I  , 'RINOBS(I)'  , RINOBS (I)
893              IF (RINOBS (I) .NE. 0.0) GOTO 625
894      620      CONTINUE
895          PRINT *, 'Whoops, the model line profile is zero - TILT!!'
896          GOTO 800
897    C
898    C Loop through output bins to find where the intensity goes to
899    C zero.  RVEL holds the actual velocity represented by each bin.
900    C
901
902      625      IFIRST = ISTART
903          PRINT *, 'IFIRST = ', IFIRST
904          RV1 = RVEL1 + DVEL * FLOATI (IFIRST) + VELOBJ
905    C    PRINT*, RV1  , DVEL  ,FLOATI (IFIRST)  , VELOBJ
906      630      RMAX = 0.0
907          N=1
908    C
909    C The following calculates the spectra (i.e. puts the
910    C appropriate intensities in the appropriate velocity bins
911    C (lines 635-640).  This is first calculated based around an
912    C arbitrary maximum intensity (see above).  the area of this
```

```
913  C  graph is then normalized by the constant QWERTY where
914  C  QWERTY is the ratio between the computed area under the curve
915  C  and the area under the curve of the data.  The intensities
916  C  are rebined after being scaled appropriately (lines 646-647).
917  C
918        QWERTY = 1
919  635       DO 640 I = IFIRST, 410
920              IF (RINOBS (I) .GT. RMAX) RMAX = RINOBS (I)
921              RVEL = RVEL1 + DVEL * FLOATI (I) + VELOBJ
922              RVELG (N) = RVEL
923              RINOBSG (N) = RINOBS (I) * QWERTY
924              BINAREA = BINAREA + (RINOBSG (N) * DVEL)
925              N= N+1
926              IF (NEXT .EQ. 'P') PRINT *, RVEL, RINOBS (I)
927              ILAST = I
928              BIGV = (VELOBJ*2) - RVELG(1)
929              IF (RINOBS (I) .EQ. 0.0 .AND. RVEL .GT. (BIGV+50))
930        2 GOTO 645
931  640       CONTINUE
932  645       INUM = ILAST - IFIRST
933  646       IF (QWERTY .EQ. 1)  THEN
934        QWERTY = NORM/BINAREA
935        PRINT*, 'NORM COEFF. = ', QWERTY
936        PRINT*, 'if normalization is done input the real norm.
937        2coeff,'
938        PRINT*, 'if normalizing the input is listed above, reenter
939        2 it'
940        READ*, QWERTY
941        T = 1
942        DO 647 I = IFIRST, 410
943              IF (RINOBS (I) .GT. RMAX) RMAX = RINOBS (I)
944              RVEL = RVEL1 + DVEL * FLOATI (I) + VELOBJ
945              RVELG2 (T) = RVEL
946              RINOBSG2 (T) = RINOBS (I) * QWERTY
947  C           PRINT*, T , RINOBSG2 (T), RVELG2 (T)
948              T=T+1
949                BIGV = (VELOBJ*2) - RVELG2(1)
950
951                IF (RINOBS (I) .EQ. 0.0 .AND. RVEL .GT. (BIGV+50))
952        2 GOTO 645
953  647       CONTINUE
954        ELSE
955        CONTINUE
956        END IF
957  C
958        T=T-1
959        N=N-1
960        LASTN = N
961        PRINT *, 'LASTN= ', LASTN , ILAST , BINAREA
962        PRINT *, 'There are ', INUM, ' intensities of interest'
963        PRINT *, 'The maximum intensity is ', RMAX
964  C
965  800       PRINT *, ' '
966        PRINT *, 'SHOW VALUES/GRAPH MODEL (S),
967        2"GOODNESS"/GRAPH DATA&MODEL (G), DONE (D)'
968  810       READ *, NEXT
969  C   IF (NEXT .EQ. 'A' .OR. NEXT .EQ. 'a') GOTO 10
```

```
970          IF (NEXT .EQ. 'S' .OR. NEXT .EQ. 's') GOTO 820
971          IF (NEXT .EQ. 'G' .OR. NEXT .EQ. 'g') GOTO 819
972          IF (NEXT .EQ. 'D' .OR. NEXT .EQ. 'd') GOTO 1000
973          PRINT *, 'TRY AGAIN'
974          GOTO 810
975   C
976   C Show the velocities and intensities.
977   C
978    819 CALL RMSCALC (LASTN, RVELG2, RINOBSG2, BINAREA, DVEL)
979        GOTO 800
980    820    PRINT *, 'LASTN=   ', LASTN
981        CALL GRAPHX(LASTN, RVELG2, RINOBSG2, BINAREA, DVEL)
982        GOTO 800
983   C
984   C Write results to a file.
985   C
986    900       FILENAME = 'cospl.dat'
987    905       OPEN (UNIT=8, FILE=FILENAME, FORM='FORMATTED',
988        2STATUS='NEW', ERR=910, IOSTAT=IOS)
989        GOTO 930
990    910       IF (IOS .NE. 117) GOTO 920
991        PRINT *, 'A FILE OF THAT NAME ALREADY EXISTS'
992        PRINT *, 'INTENDED TO WRITE INTO cospl.dat, '
993        PRINT *, '   PLEASE INPUT ANOTHER FILE NAME'
994        READ *, FILENAME
995        GOTO 905
996    920       PRINT *, 'ERROR OPENING THE FILE, IOS = ', IOS
997        GOTO 800
998    930       RNUM = FLOATI (INUM)
999        WRITE (UNIT=8, FMT=932, ERR=935, IOSTAT=IOS)
1000        2RNUM, DVEL, RV1
1001   932       FORMAT (F6.2, F6.2, F8.2)
1002        WRITE (UNIT=8, FMT=933, ERR=935) TIP, FRACR, VELCON, VELOBJ
1003   933   FORMAT (F6.1, F6.2, F6.1, F8.1)
1004        GOTO 940
1005   935       PRINT *, 'ERROR WRITING FIRST DATA, IOSTAT = ', IOS
1006        GOTO 800
1007   940       DO 950 I = IFIRST, ILAST-1
1008        WRITE (UNIT=8, FMT=952, ERR=955, IOSTAT=IOS) RINOBS (I)
1009   950       CONTINUE
1010   952       FORMAT (F10.2)
1011        GOTO 960
1012   955       PRINT *, 'ERROR WRITING RINOBS DATA, IOSTAT = ', IOS
1013   960       CLOSE (UNIT=8)
1014   C
1015   C The program is finished.Get ready to return to main procedure.
1016   C
1017   1000       STOP 'COSPEC done'
1018        END
1019   C
1020   C - - - - - - - - - - - - -- - - - - - - - - - - - - - - - - - - -
1021   C
1022        REAL FUNCTION TELSENS (RADIUS, REALJ, TIP, OFFSET,
1023        2CONV, TOP)
1024   C
1025   C This subroutine calculates the projected distance of the
1026   C current disk chunk from the disk centre, then computes the
```

```
1027  Cvalue of the normalized main beam power pattern at this distance
1028  C from beam centre.
1029  C
1030  C For IRAM 30m CO (J=2-1), the main beam is a Gaussian with
1031  C FWHM = 10.5".  See Greve et al. 1998, A&ASS, 133, 271 for
1032  C details on PP calculation
1033  C
1034  C
1035  C
1036        X1 = RADIUS * COSD(REALJ/10)   !gives position in XY plane
1037        Y1 = RADIUS * SIND(REALJ/10)
1038        XPRIME = X1                    !gives position on plane of sky
1039        YPRIME = Y1*COSD(TIP)
1040        XNOT = OFFSET/CONV        !defines PP center in sky plane
1041        YNOT = 0
1042  C
1043        DIS = SQRT((XPRIME * XPRIME)+(YPRIME * YPRIME))
1044        IF (XPRIME .LT. 0) DIS = -DIS
1045        IF (XPRIME .EQ. 0) XANG = 0
1046        IF (XPRIME .NE. 0) XANG = ATAN(YPRIME/XPRIME)*57.296
1047        ANGLE = TOP + XANG
1048        XPRIME2 = DIS * COSD(ANGLE)
1049        YPRIME2 = DIS * SIND(ANGLE)
1050        XSIDE = XPRIME2 - XNOT !3 lines calc. dist. fr. PP centre
1051        YSIDE = YPRIME2 - YNOT
1052  C
1053        PPMAX = SQRT((XSIDE * XSIDE) + (YSIDE * YSIDE))
1054        ARCSQ = (PPMAX*CONV) * (PPMAX*CONV) !conv. to " and squares
1055        SIDEARC = 2.77237188 * ARCSQ ! (.53*pi)^2 * ARCSQ (see ref)
1056        SIDE1 = (EXP (-SIDEARC/15625)) * 0.005 !calc. contribution
1057        SIDE2 = (EXP (-SIDEARC/32400)) * 0.001 !from the error
1058        SIDE3 = (EXP (-SIDEARC/902500)) * 0.00009 !beams (see ref.)
1059        SIDES = SIDE1 + SIDE2 + SIDE3          !adds up error beams
1060        TELSENS = (EXP (-ARCSQ/39.76)) + SIDES   !calculates PP
1061        RETURN
1062        END
1063  C
1064  C------------------------------------------------------------------
1065  C
1066        REAL FUNCTION TELSENS2 (RADIUS, REALJ, TIP,
1067        2OFFSET, CONV, TOP)
1068  C
1069  C This subroutine calculates the projected distance of the
1070  C current disk chunk from the disk centre, then computes the
1071  C value of the normalized main beam power pattern at this
1072  C distance from beam centre.
1073  C
1074  C For IRAM 30m CO (J=1-0), the main beam is a Gaussian with
1075  C FWHM = 20.7".  See Greve et al. 1998, A&ASS, 133, 271
1076  C for details on PP calculation
1077  C
1078  C
1079        X1 = RADIUS * COSD(REALJ/10)   !gives position in XY plane
1080        Y1 = RADIUS * SIND(REALJ/10)
1081        XPRIME = X1                    !gives position on plane of sky
1082        YPRIME = Y1 * COSD(TIP)
1083        XNOT = OFFSET/CONV          !defines PP center in sky plane
```

```
1084        YNOT = 0
1085  C
1086        DIS = SQRT((XPRIME * XPRIME)+(YPRIME * YPRIME))
1087        IF (XPRIME .LT. 0) DIS = -DIS
1088        IF (XPRIME .EQ. 0) XANG = 0
1089        IF (XPRIME .NE. 0) XANG = ATAN(YPRIME/XPRIME)*57.296
1090        ANGLE = TOP + XANG
1091        XPRIME2 = DIS * COSD(ANGLE)
1092        YPRIME2 = DIS * SIND(ANGLE)
1093        XSIDE = XPRIME2 - XNOT !3 lines calc. dist. from PP center
1094        YSIDE = YPRIME2 - YNOT
1095  C
1096        PPMAX = SQRT((XSIDE * XSIDE) + (YSIDE * YSIDE))
1097        ARCSQ = (PPMAX*CONV) * (PPMAX*CONV)!conv. to ", squares
1098        SIDEARC = 2.77237188 * ARCSQ !(.53*pi)^2 * ARCSQ (see ref.)
1099        SIDE1 = (EXP (-SIDEARC/51529)) * 0.0009 !calc. contribution
1100        SIDE2 = (EXP (-SIDEARC/143641)) * 0.0003 !fromthe error
1101        SIDE3 = (EXP (-SIDEARC/3591025)) * 0.00004 !beams (see ref)
1102        SIDES = SIDE1 + SIDE2 + SIDE3           !adds up error beams
1103        TELSENS2 = (EXP (-ARCSQ/154.55)) + SIDES  !calculates PP
1104        RETURN
1105        END
1106  C
1107  C-----------------------------------------------------------------
1108  C
1109        SUBROUTINE GRAPHX (LASTN, RVELG2, RINOBSG2, BINAREA, DVEL)
1110  C
1111  C     This subroutine plots the spectra using pgplot.
1112  C
1113        INTEGER LASTN
1114        REAL RVELG2 (410), RINOBSG2 (410)
1115  C
1116  C
1117        call pgbeg (0,'?',1,1)
1118        CALL PGPAGE                                ! These 5 lines
1119        CALL PGVSIZ (1.5, 6.5, 1.5, 3.75) !set up the graph window
1120        CALL PGSWIN (300.,1200.,-0.02,0.12) !(axes, etc..) and
1121        CALL PGBOX ('BCNST', 0.0, 0, 'BCNST', 0.0, 0) !the labels
1122        call pglab ('velocity','intensity','Simulated CO Spectra')
1123        PRINT *, 'LASTN=  ', LASTN
1124        PRINT *, 'VELOCITY   INTENSITY  BIN AREA'
1125        DO 999 T= 1, (LASTN)
1126  C
1127  C     The next lines print out a list of the plotted values and
1128  C        creates the binned graph
1129  C
1130        PRINT *, RVELG2 (T), RINOBSG2 (T), ((RINOBSG2 (T)) * DVEL)
1131        call pgbin ((LASTN),RVELG2,RINOBSG2,1)
1132  999   CONTINUE
1133          call pgend
1134          RETURN
1135          END
1136  C
1137  C-----------------------------------------------------------------
1138  C
1139        SUBROUTINE RMSCALC (LASTN, RVELG2, RINOBSG2, BINAREA, DVEL)
1140  C
```

```
1141   C     This subroutine compares the model and data bin by bin and
1142   C     produces a measure of how well they match called the
1143   C     goodness of fit parameter, GOOD.  The user enters a range
1144   C     of velocities over which the comparison is done.
1145   C     The subroutine finds which bins are the same in the model
1146   C     and the data file (it can be another model the file is set
1147   C     up the same as the data files) and subtracts one intensity
1148   C     value from the other (same velocity bin) and squares
1149   C     this number.  The goodness of fit parameter takes the
1150   C     square root of the total of the intensities differences
1151   C     squared and subtracts off the uncertainty in the data
1152   C     (user input at run time, varies with pointing) and
1153   C     multiplies this new value by the velocity range covered
1154   C     and divides by the area under the observed data over the
1155   C     same velocity range.  A goodness of 0 is best as that
1156   C     would mean there were no differences between the data
1157   C     and the model.
1158   C
1159   C
1160
1161         REAL VELOCITY(500), INTENSITY(500), IGNORE(500), DIFF
1162         REAL RVELG2(410), RINOBSG2(410), RMS(500), HIGHV, LOWV, INT
1163         REAL VELOCITY2(500), INTENSITY2(500), MODLOW, MODHIGH, RMS1
1164         REAL RINOBSG3(500), GOOD, TOTINT, CLARMS
1165         CHARACTER VALUE
1166         CHARACTER*20 DATA
1167         INTEGER Q,Y,T,P,NUM,L
1168   C
1169   C       enter the data file name
1170   C
1171         PRINT*, 'Input the file name for the pointing in question'
1172         READ*, DATA
1173         OPEN (UNIT=01, FILE= DATA)
1174   C
1175   C     reads in the data from the file
1176   C
1177         Y=0
1178         DO 777 Q=1,500
1179              READ (01,*,END=779) VELOCITY(Q), INTENSITY(Q),
1180        2IGNORE(Q)
1181              Y=Y+1
1182   777 CONTINUE
1183   779    CONTINUE
1184   C
1185         NUM=LASTN-1
1186         ALL=Y
1187         P=ALL
1188         DO 333 Q = 1, ALL
1189         VELOCITY2(P) = VELOCITY(Q)
1190         INTENSITY2(P) = INTENSITY(Q)
1191         P=P-1
1192   333 CONTINUE
1193   C
1194   C the following lines match up the highest and the lowest
1195   C velocity bins and make sure they are within half the value
1196   C of the bin size of each other i.e. 440 km/s in the model
1197   C and 442 km/s in the data are considered the same bin since
```

```
1198  C the bin values will most likely never be the exact same.
1199  C
1200        MODLOW = RVELG2(1)
1201        MODHIGH = RVELG2(NUM)
1202        DIFF = DVEL
1203        DO 111 Q = 1,ALL
1204             DIFF = MODLOW - VELOCITY2(Q)
1205             Z=Q
1206             IF (ABS(DIFF) .LT. DVEL/2) GOTO 112
1207  111   CONTINUE
1208  112   DO 113 Q = 1,ALL
1209             DIFF = MODHIGH - VELOCITY2(Q)
1210             L=Q
1211             IF (ABS(DIFF) .LT. DVEL/2) GOTO 114
1212  113   CONTINUE
1213  114   RMS1 =0
1214  C
1215  C
1216  C    these next lines take the intensity differences
1217  C    for each velocity bin
1218  C
1219        DO 654 T=1,ALL
1220        IF ((T .LT. Z) .OR. (T .GT. L)) INT = 0.0
1221        IF ((T .GE. Z) .AND. (T .LE. L)) INT = RINOBSG2(T-Z+1)
1222        RINOBSG3(T) = INT
1223        RMS(T) = ((INT) - INTENSITY2(T))*((INT) - INTENSITY2(T))
1224             RMS1 = RMS1 + RMS(T)
1225  654   CONTINUE
1226        PRINT*, RMS1
1227        STD= SQRT(RMS1/(ALL))   !the whole velocity range
1228        PRINT*, STD
1229  C686 CONTINUE
1230        PRINT*, 'input the CLASS RMS value for this pointing'
1231        PRINT*, 'type 0 if the value is unknown'
1232        READ*, CLARMS
1233        PRINT*, 'input the lowest velocity which contains
1234        2useful data for your current pointing'
1235        READ*, LOWV
1236        PRINT*, 'input the highest velocity which contains
1237        2useful data for your current pointing'
1238        READ*, HIGHV
1239  C
1240        RMS1=0   !makes sure that the input vel. range matches the
1241        DO 211 Q = 1,ALL   !closest velocity bins in both the model
1242             DIFF = LOWV - VELOCITY2(Q)!and the data it is
1243             C=Q                       !similar to  the above
1244             IF (ABS(DIFF) .LT. DVEL/2) GOTO 212
1245  211   CONTINUE
1246  212   YLOW=  VELOCITY2(C)
1247        DO 213 Q = 1,ALL
1248             DIFF = HIGHV - VELOCITY2(Q)
1249             D=Q
1250             IF (ABS(DIFF) .LT. DVEL/2) GOTO 214
1251  213   CONTINUE
1252  214   YHIGH= VELOCITY2(D)
1253        NUMBER = D-C+1
1254        PRINT*, ' Q      V          INTDATA    INTMOD    RMS'
```

```
1255          TOTINT=0
1256          DO 353 Q=C,D
1257          PRINT*, Q,' ', VELOCITY2(Q), INTENSITY2(Q), RINOBSG3(Q),
1258          2RMS(Q)
1259          RMS1= RMS1+RMS(Q)
1260          TOTINT = TOTINT + (ABS(INTENSITY2(Q)*10.4))
1261   353    CONTINUE
1262          PRINT*, TOTINT
1263          STD= SQRT(RMS1/(NUMBER))
1264          PRINT*, 'the average uncertainty, sigma = ',STD
1265   C
1266   C this next line calculates the goodness of fit parameter
1267   C
1268          GOOD = ((STD-CLARMS)*(YHIGH-YLOW+10.4))/TOTINT
1269          PRINT*, 'the "Goodness" parameter, where 0 is best = ',
1270          2GOOD
1271          PRINT*, ' '
1272          PRINT*, 'type y to plot a graph of the model and the data,
1273          2type anything else to escape'
1274          READ*, VALUE
1275          IF (VALUE .EQ. 'Y' .OR. VALUE .EQ. 'y') GOTO 454
1276          GOTO 464
1277   454    CALL GRAPH2 (ALL, VELOCITY2, RINOBSG3, INTENSITY2)
1278   464    RETURN
1279          END
1280   C
1281   C
1282   C------------------------------------------------------------------
1283   C
1284          SUBROUTINE GRAPH2 (ALL, VELOCITY2, RINOBSG3, INTENSITY2)
1285
1286   C This subroutine plots the actual pointing data and the model
1287   C together using pgplot.A 3rd data set can also be added whether
1288   C it be actual data or another model provided the file is set up
1289   C in the same form as before
1290   C
1291          INTEGER RED, GREEN, BLACK, WHITE, CYAN, BLUE
1292          PARAMETER (RED=2)                  !sets up the colours
1293          PARAMETER (GREEN=3)                !see comments in
1294          PARAMETER (BLACK=1)                !CLOUDPIC subroutine
1295          PARAMETER (WHITE=4)
1296          PARAMETER (CYAN=5)
1297          PARAMETER (BLUE=6)
1298   C
1299          INTEGER Q,O
1300          REAL VELOCITY2 (500), RINOBSG3 (500)
1301          REAL INTENSITY2 (500)
1302          REAL VELEXTRA(500), INTEXTRA(500), IGNOREEXTRA(500)
1303          REAL VELEXTRA2(500), INTEXTRA2(500)
1304          CHARACTER*20 DATA2
1305          CHARACTER YES
1306          LOGICAL MORE
1307   C
1308          MORE=.FALSE.
1309          PRINT*, 'ADD ANOTHER DATA SET?'
1310          READ*, YES
1311          IF (YES .EQ. 'y') MORE=.TRUE.
```

```
1312          IF (MORE) THEN
1313          GOTO 867
1314          ELSE
1315          GOTO 879
1316          END IF
1317    867   PRINT*, 'type in the file name'
1318          READ*, DATA2
1319          OPEN (UNIT=02, FILE= DATA2)
1320    C
1321          O=0
1322          DO 877 Z=1,500
1323                READ (02,*,END=881) VELEXTRA(Z), INTEXTRA(Z),
1324          2IGNOREEXTRA(Z)
1325                  O=O+1
1326    877   CONTINUE
1327    C
1328    881   N=1
1329          DO 644 T=1,ALL
1330          COND = ABS(VELOCITY2(T) - VELEXTRA(N))
1331          IF (COND .GE. 5) THEN
1332          VELEXTRA2(T) = VELOCITY2(T)
1333          INTEXTRA2(T) = 0
1334          GOTO 644
1335          ELSE
1336          VELEXTRA2(T) = VELOCITY2(T)
1337          INTEXTRA2(T) = INTEXTRA(N)
1338          N=N+1
1339          END IF
1340    644   CONTINUE
1341    C
1342    879      CONTINUE
1343    C
1344          call pgbeg (0,'?',1,1)
1345          CALL PGSCI(BLACK)
1346          CALL PGPAGE                          !These 5 lines
1347          CALL PGVSIZ (1.5, 6.5, 1.5, 3.75)        !set up the graph
1348          CALL PGSWIN (300.,1200.,-0.02,0.18)      !window(axes, etc..)
1349          CALL PGBOX ('BCNST', 0.0, 0, 'BCNST', 0.0, 0) !and the
1350          call pglab (' ',' ', ' ')          !labels. See pgplot manual
1351          call pglab ('Velocity (km/s)',' T main beam (K)', ' ')
1352    C
1353          DO 868 Q = 1, ALL
1354
1355          CALL PGSCI(RED)
1356          CALL PGSLW (3)
1357          Call pgbin (125,VELOCITY2,RINOBSG3,1)      ! model
1358    868   CONTINUE
1359             DO 869 Q = 1, ALL
1360          CALL PGSCI(BLACK)
1361          CALL PGSLW (1)
1362          Call pgbin (125,VELOCITY2,INTENSITY2,1)   ! pointing data
1363    869   CONTINUE
1364             IF (MORE) THEN
1365             DO 889 Q = 1, ALL
1366          CALL PGSCI(GREEN)
1367          CALL PGSLW (3)
1368          Call pgbin (125,VELEXTRA2,INTEXTRA2,1)
```

```
1369   889    CONTINUE
1370          ELSE
1371          GOTO 890
1372          END IF
1373   890    call pgend
1374          RETURN
1375          END
1376   C
1377   C
1378   C-------------------------------------------------------------------
1379   C
1380          REAL FUNCTION FUNCTION1(RADIUS, R0)
1381   C
1382   C   intensity profile for an exponential disc
1383   C
1384          FUNCTION1 = 1 * (EXP (RADIUS/R0))
1385          RETURN
1386          END
1387   C
1388   C
1389   C-------------------------------------------------------------------
1390   C
1391   C
1392          REAL FUNCTION FUNCTION2 (FWHM, RADIUS)
1393   C
1394   C   intensity profile for a Gaussian disk
1395   C
1396          REAL FUNCTION2D, FUNCTION2E
1397
1398          FUNCTION2D = 1    !   (1/(2.50662827463 * ABS(FWHM/2.354)))
1399          FUNCTION2E = (EXP(-.5*((RADIUS/(FWHM/2.354))*
1400          2(RADIUS/(FWHM/2.354)))))
1401          FUNCTION2 = FUNCTION2D * FUNCTION2E
1402          RETURN
1403          END
1404   C
1405   C
1406   C-------------------------------------------------------------------
1407   C
1408          REAL FUNCTION FUNCTION3 (RING, CONV, RADIUS)
1409   C
1410   C   intensity profile for a flat ring
1411   C
1412          REAL RINGCU
1413
1414          RINGCU = RING/CONV
1415          IF (RADIUS .LE. RINGCU) THEN
1416          FUNCTION3 = 0
1417          ELSE
1418          FUNCTION3 = 1
1419          END IF
1420          RETURN
1421          END
1422   C
1423   C
1424   C-------------------------------------------------------------------
1425   C
```

```
1426    C
1427          REAL FUNCTION FUNCTION4 (FWHM, RADIUS, GRR)
1428    C
1429    C  intensity profile for a ring with the Gaussian centered at
1430    C  a specified radius within the ring.
1431    C
1432          REAL FUNCTION4D, FUNCTION4E
1433
1434
1435          FUNCTION4D = 1      ! (1/(2.50662827463 * ABS(FWHM/2.354)))
1436          FUNCTION4E = (EXP(-.5*(((RADIUS - GRR)/(FWHM/2.354))*
1437          2((RADIUS - GRR)/(FWHM/2.354)))))
1438          FUNCTION4 = FUNCTION4D*FUNCTION4E
1439          RETURN
1440          END
1441    C
1442    C-------------------------------------------------------------------
1443    C
1444    C
1445          REAL FUNCTION FUNCTION5 (RADIUS, TRUNC, GRR, FWHM)
1446    C
1447    C  intensity profile for a truncated ring with the Gaussian
1448    C  centered at a specified radius within the ring.
1449    C
1450          REAL FUNCTION5D, FUNCTION5E
1451
1452          IF (RADIUS .LE. TRUNC) THEN
1453          FUNCTION5 = 0
1454          ELSE
1455          FUNCTION5D = 1    !(1/(2.50662827463 * ABS(FWHM/2.354)))
1456          FUNCTION5E = (EXP(-.5*(((RADIUS - GRR)/(FWHM/2.354))*
1457          2((RADIUS - GRR)/(FWHM/2.354)))))
1458          FUNCTION5 = FUNCTION5D*FUNCTION5E
1459          END IF
1460          RETURN
1461          END
1462    C
1463    C --------------------------------------------------------------
1464    C
1465          SUBROUTINE CLOUDPIC(NCLOUD, CLSIZE, RINTCL, RCLOUD,
1466          2AZCLOUD)
1467
1468    C This subroutine generates a picture of the physical locations
1469    C of the added asymmetries using pgplot plot.The "hot" spots are
1470    C drawn in red and the "cold" spots are drawn in cyan. All sizes
1471    C are to scale based on the input disk size.
1472    C
1473          INTEGER RED, GREEN, BLACK, WHITE, CYAN, BLUE
1474          PARAMETER (RED=2)                  !sets up the colours
1475          PARAMETER (GREEN=3)                !not all colours are used
1476          PARAMETER (BLACK=1)                ! note "BLUE" looks purple
1477          PARAMETER (WHITE=4)                ! and "CYAN" looks blue
1478          PARAMETER (CYAN=5)
1479          PARAMETER (BLUE=6)
1480             INTEGER B
1481          REAL XCIR, YCIR, RCIR
1482          REAL RCLOUD(10,3), AZCLOUD(10,3)
```

```
1483        REAL CLSIZE(10)
1484        REAL RINTCL(10)
1485
1486        CALL PGBEG(0,'?',1,1)
1487    C
1488    C these lines set up the plot window. Their function is the
1489    C same as that stated in the graphing subroutines, although
1490    C their values may differ.
1491    C
1492        CALL PGPAGE
1493        CALL PGVSIZ (1.6, 9.1, 0.1, 7.6)
1494        CALL PGSWIN (0.,200.,0.,200.)
1495        CALL PGBOX ('BCNT', 0.0, 0, 'BCNST', 0.0, 0)
1496        CALL PGLAB('(X)','clouds in a galaxy far far away',
1497        2'clouds in a galaxy far far away')
1498    C
1499        call pgsfs (2)
1500        call pgsci (black)
1501        call pgcirc (100.0,100.0, 100.0) ! sets up the whole disk
1502    C
1503    C     call pgsci (green)
1504    C     call pgcirc (100.0, 100.0, 37.5) ! plots a ring
1505    C   call pgcirc (100.0, 100.0, 62.5) ! plots a ring
1506    C    these rings are for specific work and are commented out
1507    C
1508        call pgsci (black)
1509        DO 1262 B=1,NCLOUD
1510        RCIR = 0.5*CLSIZE(B) !gives the cloud radius to be plotted
1511        IF (RINTCL (B) .LT. 1) call pgsci (cyan)   !for holes
1512        IF (RINTCL (B) .GE. 1) call pgsci (red)    !for clouds
1513    C
1514    C  These next lines gives x and y coordinates for the center of
1515    C  the circle
1516    C
1517        XCIR = abs(RCLOUD(B,1)*100*COS((AZCLOUD(B,1)/180)*
1518        23.14159265359))
1519        YCIR = abs(RCLOUD(B,1)*100*SIN((AZCLOUD(B,1)/180)*
1520        23.14159265359))
1521    C
1522    C  These lines make sure the circles are drawn on the right
1523    C  side of the disk.
1524    C
1525        IF (AZCLOUD(B,1) .LE. 180) YCIR2 = YCIR+100
1526        IF (AZCLOUD(B,1) .GT. 180) YCIR2 = 100-YCIR
1527        IF (AZCLOUD(B,1) .LE. 90) XCIR2 = 100-XCIR
1528        IF (AZCLOUD(B,1) .GT. 90 .AND. AZCLOUD(B,1) .LE. 270)
1529        2XCIR2 = XCIR+100
1530        IF (AZCLOUD(B,1) .GT. 270) XCIR2 = 100-XCIR
1531        call pgcirc (XCIR2, YCIR2, RCIR)   ! plots the cloud or hole
1532   1262 CONTINUE
1533        CALL PGEND
1534        RETURN
1535        END
1536
1537    C-------------------------------------------------------------------
1538
1539            REAL FUNCTION GAUSSDEV (VD, SEED1, SEED2) ! Box-Mueller
```

```
1540   C
1541   C This function generates Gaussian deviates based on the
1542   C Box-Mueller algorithm found in Bevington and Robinson (1992),
1543   C Data Reduction and Error Analysis for the Physical Sciences,
1544   C 2nd Edition.
1545   C
1546   C The deviates are used in this work to simulate velocity
1547   C dispersion GAUSSDEV is multiplied by the velocity dispersion
1548   C average value at a given radius and is then added to the
1549   C velocity given by the rotation curve.  Naturally, The final
1550   C velocity dispersion value can be positive or negative.
1551   C
1552              REAL   RGD, FGD, z1GD, z2GD, SEED1, SEED2
1553              REAL   X1RanGauss, X2RanGauss
1554   C
1555          IF (VD) THEN
1556          GOTO 911
1557          ELSE
1558          GAUSSDEV = 0
1559          GOTO 912
1560              END IF
1561    911       RANDOM1=RAN(SEED1)
1562            RANDOM2=RAN(SEED2)
1563            z1GD = -1 + 2*RANDOM1
1564            z2GD = -1 + 2*RANDOM2
1565            RGD  = z1GD*z1GD + z2GD*z2GD
1566            if (RGD .GE. 1) goto 911
1567            FGD = SQRT(-2*Alog(RGD)/RGD)
1568          X1RanGauss = z1GD*FGD
1569          X2RanGauss = z2GD*FGD
1570          GAUSSDEV = X1RanGauss
1571    912   Return
1572          END
```

Appendix B

COSPEC and its Use for Work on NGC 5866

The basic COSPEC model simulates an inclined, infinitely thin disk with a given intensity profile distribution. The intensity given by a certain model can be convolved with an approximation to a telescope power pattern and a velocity spectrum is output. Several features can be added to any model in order to synthesize complicated features often seen in extra galactic observations. Such features include the addition of brighter or fainter regions sections to the chosen radial intensity profile and the addition of velocity dispersion in order to simulate more realistic physical conditions. By experimenting with the various parameters, solid conclusions about the nature and morphology of the molecular gas in a galaxy can be made.

B.1 An Overview of COSPEC

The COSPEC program was originally written to simulate a single JCMT observation of the edge-on lenticular galaxy, NGC 4710 located in the Virgo galaxy cluster. The program was extensively changed in order to simulate a disk or ring with various

intensity profiles and viewed with a representation of the IRAM 30m radio telescope for work on NGC 5866. Other features were also added to make the program more general for future use in synthesizing spectra from any galaxy in general. These changes include: a multi CO transition power pattern which can view the inclined disk anywhere along the major axis, a variable disk diameter, a user defined, 2 regime solid body rotation curve, a variable normalization area and the addition of a velocity dispersion component.

The program was designed to simulate the spectra taken by the IRAM 30m telescope by binning the "signal" collected by the power pattern subroutine while "observing" the rotating disk. The output is a spectrum, normalized to the data and binned to the same resolution as the actual data. The quality of the model is checked by comparing the simulated spectrum and the actual data on a bin by bin basis. COSPEC assumes that all of the intensity is seen by the power pattern (i.e. the specified intensity is not "radiated" isotropically). This also includes any asymmetries added to a profile. No "shadowing" is assumed so all clouds are seen regardless of geometrical location in the disk or disk inclination.

B.1.1 The Parameters

COSPEC has been designed to provide the user as many parameters as possible. At run time a list is presented of all the parameters and their standard values. The user is free to accept or change any number of these, any number of times, before continuing. A list of parameters and their function is presented in table B.1. Generally, the parameters control: The rotation curve (two regimes of solid body rotation, each one either rising or

falling), the intensity distribution (constant intensity disk or ring, Gaussian disk or ring, exponential disk or truncated Gaussian ring), the CO rotational transition as seen by the convolving beam (^{12}CO J=2-1, or ^{12}CO J=1-0), the inclusion of asymmetries in the intensity distribution (called "clouds" in this appendix, although they can be of higher or lower intensity than their surroundings), the disk size in arcseconds, the location of the power pattern centre with respect to the centre of the major axis of the disk, and the systemic and rotational speeds. The only parameter which would need to be changed in the source code itself is the velocity dispersion relation with respect to radius (line 649). The velocity dispersion function (GAUSSDEV), which actually generates the velocity dispersion values, is independent of the radial relation and so needs not be changed. Figure B.1 shows an example of the standard parameter set as it appears at run time. The reason for the warning about changing ARCDISC first is that the conversion factor (CONV) translates all arcsecond inputs into computer units (cu). The cu is the computer distance unit. All parameters of extension, distance or location which are entered in arcseconds are converted by the code to cus internally.

```
        ******************************
        *  THE STANDARD PARAMETER SET  *
        ******************************

a)  MODEL = CONSTANT INTENSITY DISK

b)  CLOUDS? = NO

c)  TIP =     90.0000 degrees  The inclination on the sky

d)  TOP =   0. degrees   The angle with respect to the power pattern axis

e)  ARCDISC =    60.0000 "   The disk diameter

f)  VELOBJ =    745.000 km/s  The systemic velocity

g)  VELCON =    305.000 km/s  The disk edge rotational velocity

h)  TURNRAD =    10.00000 "   Regime change radius in the rotation curve

i)  TURNVEL =    200.000 km/s  Regime change velocity in the rotation curve

j)  POWER PATTERN ON? = YES

k)  OFFSET =    0. "  Power pattern offset.  If no PP, this is ignored

l)  CO transition : J=1-0

m)  DVEL =    10.40000 km/s  the spectrum bin size

n)  VELOCITY DISPERSION ON? = NO

o)  AREA USED FOR NORMALIZATION =    22.1000 T km/s

p)  DISPLAY ROTATION CURVE DATA? = NO


          You have made   0 changes to the parameter set

    ****************************************************************
    * IF THIS IS FINE, TYPE LOWER CASE "y", IF NOT, INPUT THE *
    *LOWER CASE LETTER NEXT TO THE QUANTITY YOU WANT TO CHANGE*
    *                                                         *
    *  --->  WARNING: If changing ARCDISC, do so first  <---  *
    ****************************************************************
```

Figure B.1   An example of the prompt screen which appears at run time. Any of the standard parameters can be changed in the source code to appear as desired at run time or any change can be made from this screen.

Table B.1 The COSPEC standard parameters and their functions.

Parameter Name	Description
ARCDISC	disk diameter (")
TIP	90 degrees for an edge-on disk
TOP	angle of the power pattern center to the disk major axis
CLOUDS	including clouds or not, logical variable
NCLOUD	number of asymmetries to be placed in the intensity profile
BEAM	power pattern on or off, logical variable
OFFSET	power pattern offset from the centre disk major axis (")
TRANS21	transition, J=2-1 default, logical variable
VELCON	rotational velocity at disk edge (km/s)
VELOBJ	systemic velocity (km/s)
TURNVEL	the kink velocity in the rotation curve (km/s)
TURNRAD	the kink radius in the rotation curve (")
DISK	disk model, yes or no? logical variable
RINGS	ring model, yes or no? logical variable
DISKMOD	what kind of disk intensity distribution? constant, Gaussian or exponential
RINGMOD	what kind of ring intensity distribution? constant, Gaussian or truncated Gaussian
FWHM	FWHM expressed as a fraction of the disk size
GRR	Gaussian ring radius (")
DS	scale length of exponential disk brightness expressed as a fraction of the radius
RING	ring radius, constant intensity (")
TRUNC	inner radius where Gaussian is truncated (")
VD	velocity dispersion, yes or no? logical variable
NORM	area used to normalize the models (T km/s)
DVEL	spectrum bin width (km/s)

B.2 How the Code Operates

The following discussion preserves the names and format of the source code when discussing specific features and formulae. Once the parameter set has been initialized (rotation curve, profile, etc...) the code works by relating velocity to radius via the specified rotation curve and intensity to radius via the radial intensity distribution. There

is now a link between velocity and intensity. The code divides up the disk into a series of annuli and cuts each annulus into 3600 angular pieces, referred to in this work as a "unit area". Each unit area's intensity value is placed into the appropriate velocity bin based on the rotational velocity of the current annulus (given by the rotation curve), the unit area's azimuthal angle and the disk inclination. Figure B.2 illustrates this.
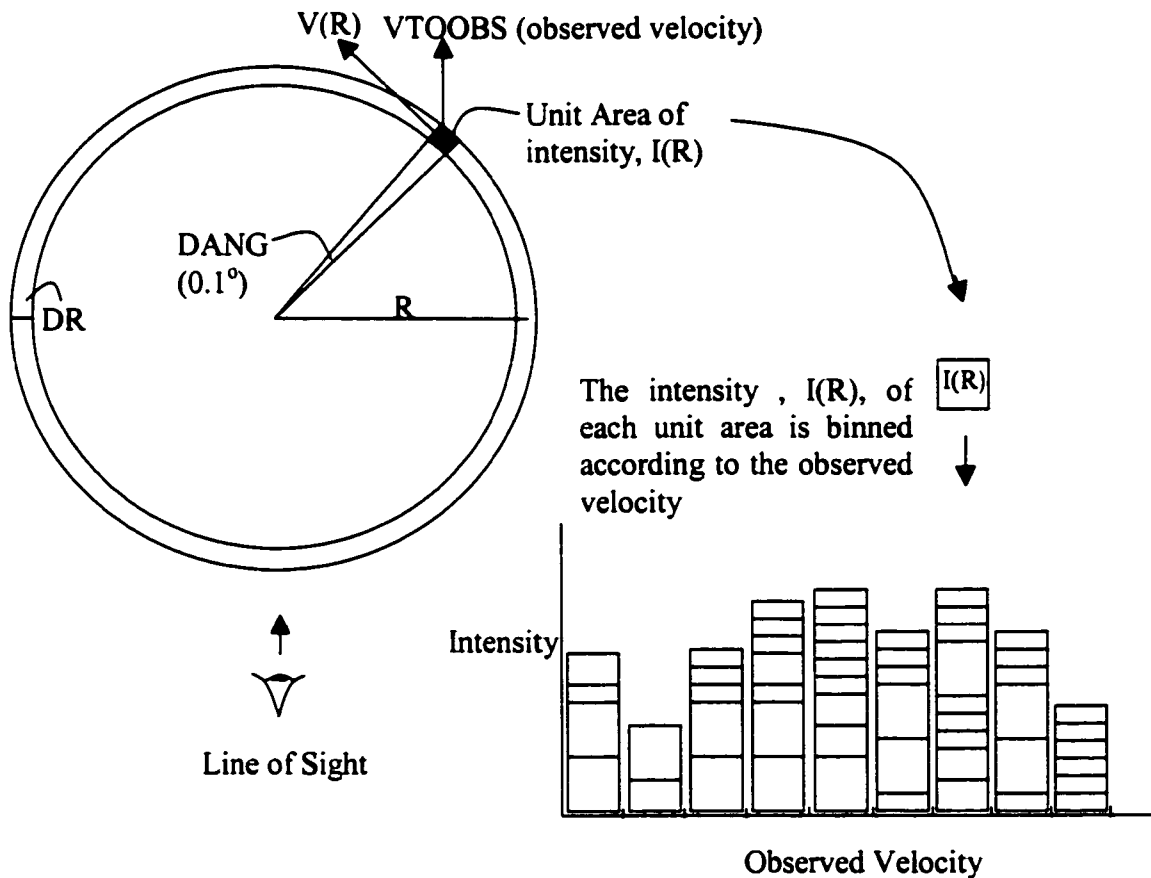
Figure B.2   This shows how COSPEC builds a spectrum. The program takes the intensity of each unit area and places it in the appropriate velocity bin based on the observed velocity of the unit area. The intensity of the unit area is given by the radial intensity distribution and weighted by the actual area of the unit area.

First, the code zeros an array which is used to store the intensities per velocity bin (RINOBS(I)). The velocity bin width is then stated in the code (10.4 km/s in this case). The velocity bin width is multiplied by 200 (arbitrarily, simply a reference point) and this value is subtracted from the systemic velocity to give a reference velocity value denoted RVEL1. RVEL1 is not the actual velocity of the first intensity but simply a reference from which the actual useful velocities are measured. Next, the program specifies the outer radius of the disk as 100 cu (ROUTER). The sine of the inclination angle is set so to correct the velocities with respect to inclination. RI0 is the intensity per unit area at the centre of the disk and is the reference by which all intensities are scaled whether it is due to the intensity distribution with radius, cloud intensity or normalization and is set to 1. The disk is broken up into several annuli which correspond to rings of equal velocity with respect to radius. The number of annuli used is a function of the maximum rotational velocity and the bin size of the spectra so that each annulus contains half a bin width of velocity so as not to undersample the disk. The increments of radius, DR, are consequently set by this procedure. Each annuli is observed over angular increments of 0.1 degree, expressed in radians, creating the unit area.

Lines 619 through 887 are the workhorse of the program. First the radius is specified by starting at one half the radius increment, DR (i.e. the middle of the first annulus) and the velocity is calculated from the rotation curve which was specified at run time. One the radius and velocity have been chosen the intensity at the given radius must be found by multiplying RI0 by a specific function listed as FUNCTIONS1-5. Table B.2 lists the functions and their associated radial intensity distributions.

Table B.2 The radial intensity distributions used by COSPEC.

Function name	Radial Intensity Profile
FUNCTION1	Exponential disk profile
FUNCTION2	Gaussian disk profile
FUNTCION3	Constant intensity ring profile
FUNCTION4	Gaussian ring profile
FUNCTION5	Truncated Gaussian ring profile

These functions specify the radial intensity distribution in the disk. No function is needed if the intensity profile is that of a constant intensity disk. FUNCTION 1 returns a value based on the radius and the scale length when an exponential disk is chosen by scaling the intensity by EXP(RADIUS/R0) where RADIUS is the current radial position and R0 is the scale length expressed in computer units (R0 $=$ DS*100cu, as found in the code). If a Gaussian disk is the chosen profile the value returned depends on the specified FWHM and the current radius. FUNCTION2 is the standard Gaussian shape:

$$FUNCTION2 = EXP[- \frac{1}{2}(RADIUS/(FWHM/2.354))^2] \qquad (B.1)$$

FUNCTION 3 is used for a constant intensity ring and makes the intensity 0 at all radii inside a specified ring radius. FUNCTION 4 is used in the case of a Gaussian ring. Here a ring radius, GRR, is specified which corresponds to the peak of a Gaussian distribution and falls off as dictated by the input FWHM.

$$FUNCTION4 = EXP[- \frac{1}{2}((RADIUS - GRR)/(FWHM/2.354))^2] \qquad (B.2)$$

Finally, FUNCTION 5 returns values for a truncated Gaussian disk. This ring is set up the same as FUNCTION4 but in this case a second radius is entered at run time for which

all intensity inside equals 0. Figures B.3-B.8 show the various how the various intensity distributions appear in velocity space.

Before the unit area's intensity value is placed in the bin the program first corrects its value based on its projected distance from the power pattern centre. The intensity is then binned accordingly and the program moves on to the next unit area and next annulus and so on. Next the program files through all velocity bins with data in them and calculates a total area under the spectrum, BINAREA. This area is normalized to specified area (NORM) and a normalizing factor is displayed on the screen (QWERTY). Lastly, the binned signal can be plotted to the same scale as the observations using PGPLOT. The spectrum is considered a good fit to the data when the sum of the difference between the simulated spectrum and the observed spectrum squared is close to zero.

B.3 Specific Features: Problems and Testing

The following section deals with the specific features of the code and how they are used.

B 3.1 The Clouds

Asymmetries, or "clouds", can be placed in the intensity profile by making a section of any given diameter more or less bright than the surrounding area. This feature of the code allows the user to synthesize complex structure in the observed spectrum by placing clouds in the appropriate geometrical place. At run time the program prompt the user for a choice on including clouds or not. Each cloud is specified by its: radial distance from the centre of the disk, azimuth, intensity as a multiple of the standard reference intensity,

and its diameter. No clouds may overlap in azimuth and radius, without crashing the code. To ensure that no clouds are overlapping when setting up the parameter set, a figure can be created with the circular clouds plotted on it to check for any overlap before continuing, similar to that shown in figure 3.1. Once the clouds have been characterized, the program finds the cloud centre and calculates the radial extend of the edges from the radial position and the diameter. Now that the program knows which annuli the clouds lie in it must find out at which angles the clouds encompass in order to adjust the intensity in the right velocity space. This is done by finding the edges in the azimuthal direction once an annulus has been identified as having part of a cloud somewhere in it. The program can deal with clouds which overlap azimuth = 0 and 360 but no cloud may be placed in the centre (i.e. encompassing AZ = 0 through 360 degrees), as the program does not recognize a negative radial distance. The program has located each cloud with respect to radius and azimuthal angle so when running through each annulus the intensity value changes accordingly when a section of cloud in an annulus is reached.

The code was tested to ensure the cloud portions were working correctly. When the program located a section of cloud inside an annulus it was instructed to return the edge azimuth and the radial position along with the base length (LBASE) and the cloud height (CLH). These values can easily be checked to ensure they are correct for a cloud of given size and position. The intensity of each cloud was checked by printing the intensity versus the radial extent without the effects of the power pattern or normalization on a constant intensity disk. When a section of annulus with a piece of cloud in was encountered, the intensity changed by the specified factor. Finally, the simulated spectra

bins were checked to ensure that the proper bins were receiving the proper change in intensity. This was done by comparing the spectrum of a non-normalized model, bin by bin, against the same model containing a cloud at a specified location.

B 3.2 The Rotation curve

The rotation curve can contain up to 2 solid body regimes. Either solid body regime may rise or fall with their own independent slope. The "kink" velocity and radius (TURNVEL and TURNRAD, respectively) are specified when defining the parameter set. Currently the rotation curve is designed to give negative velocities with positive radius. The direction of rotation is only important when adding asymmetries to the intensity profile so that the synthesized spectra gets changed in the appropriate velocity bins.

Testing the code is facilitated by the fact that the rotation curve should affect the synthesized spectrum in specific ways. An obvious test is to make sure that the simulated line width is 2 times the maximum rotational velocity. The term "line width" is defined here as the range of velocity space which has clear signal. Another simple check is to see where the data end up if there is no rotation. Naturally the bin which contains the systemic velocity should be the only non zero intensity. Also, when dealing with a kink in the curve, the spectra should exhibit "horns" at the bins where the velocity changes regimes, as the intensity is now distributed differently in velocity space.

B 3.3   The Intensity Distributions

COSPEC allows the user a choice of 6 radial intensity distributions throughout the disk (a

ring is considered to be a special case of a disk). These include a constant intensity disk

or ring, an exponential disk, a Gaussian disk or ring and a Gaussian ring in which the

central hole has zero intensity. The distributions are easily checked by plotting intensity

versus radius. The distributions all affect the output spectra in various ways. Plotting

the spectra with the power pattern off, and with a single regime, solid body rotation curve

to keep the spectra simple, differences can be seen. A flat distribution gives a spectrum

that is greatest at the centre bin and drops off after that, shown in figure B.3. This is

consistent with looking through less and less of a solid disk as the radius increases.

Simulated CO Spectra
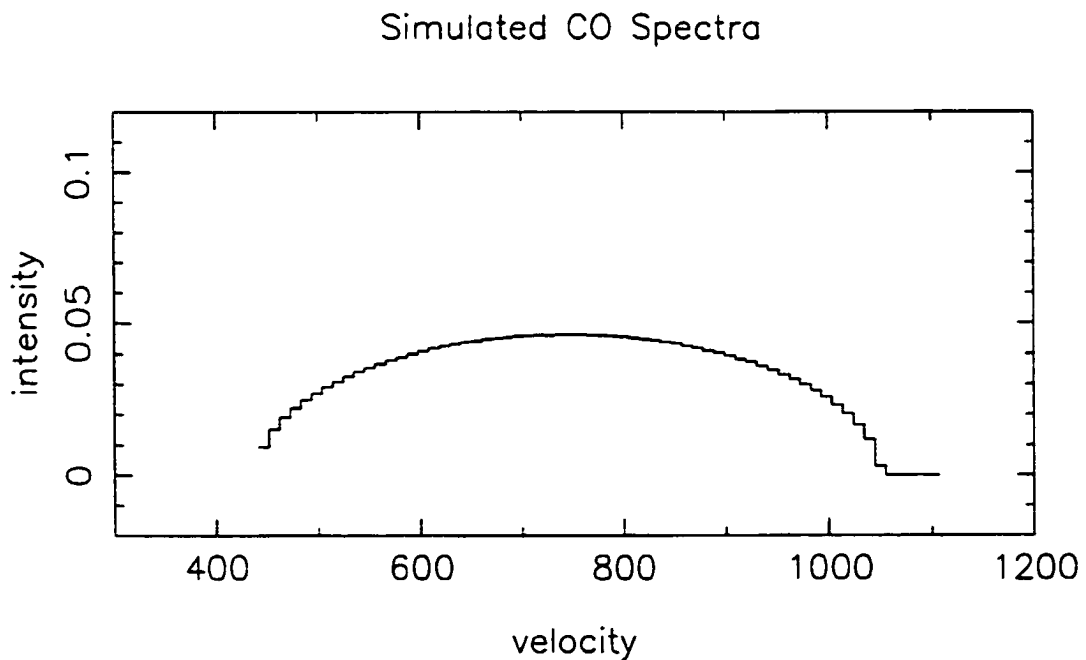
Figure B.3   A constant intensity disk model spectra with no power pattern. The maximum rotational velocity is 305 kms^{-1}, here and in the next 5 figures. Velocity is in kms^{-1} here and in the next 5 figures.

The exponential disk simulated spectrum looks similar but drops off much quicker as one is not only looking through less disk, the intensity is also weaker at larger radii. This is shown in figure B.4. A similar spectrum is generated with a Gaussian disk distribution, shown in figure B.5.

Simulated CO Spectra
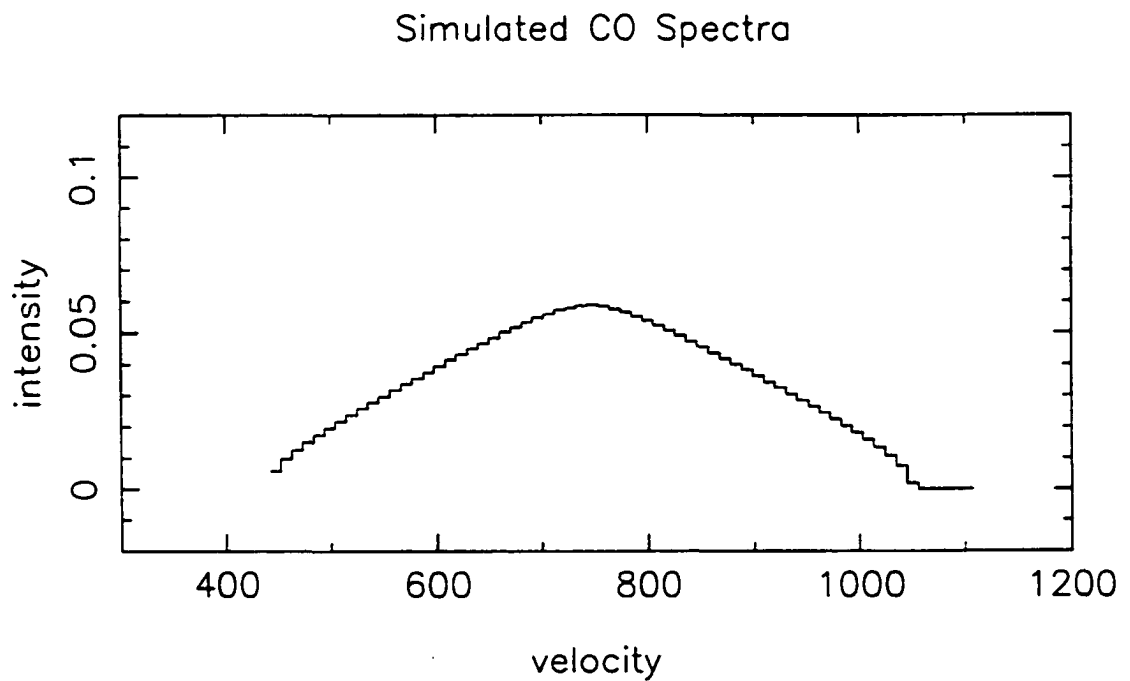
Figure B.4   The exponential disk intensity profile spectrum.   The scale length was arbitrarily chosen as 22.5".

Simulated CO Spectra
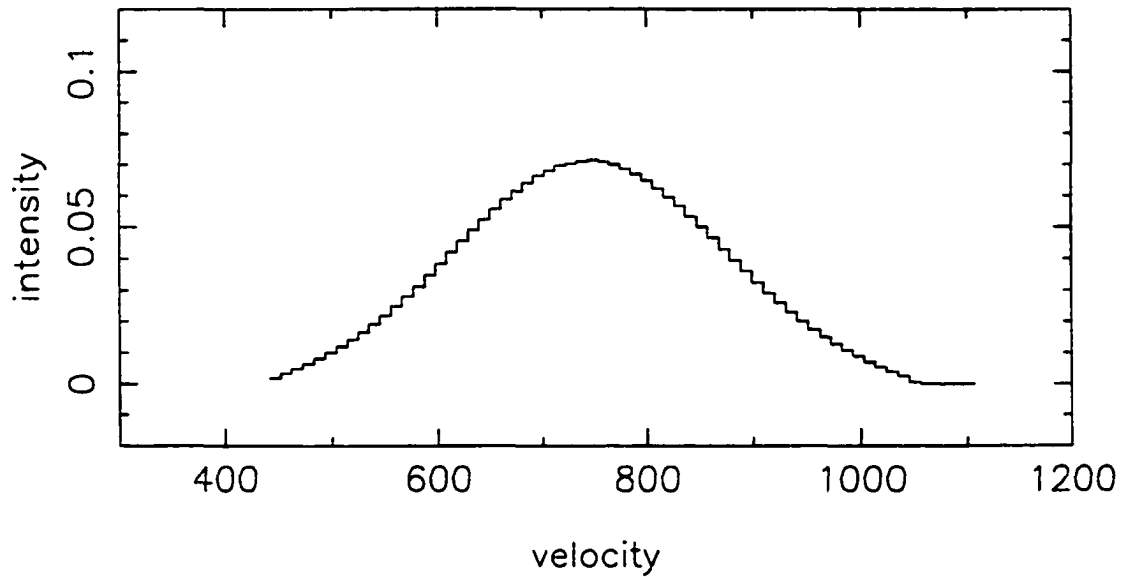
Figure B.5 The Gaussian disk intensity profile spectrum. The FWHM was arbitrarily chosen as 30".

Rings produce slightly more complicated spectra. For a large constant intensity ring, the maximum intensity appears in velocity bins further from the systemic velocity. When the hole is small, the spectrum produced looks similar to the flat disk model with less power. Figure B.6 shows the constant intensity ring.

Simulated CO Spectra
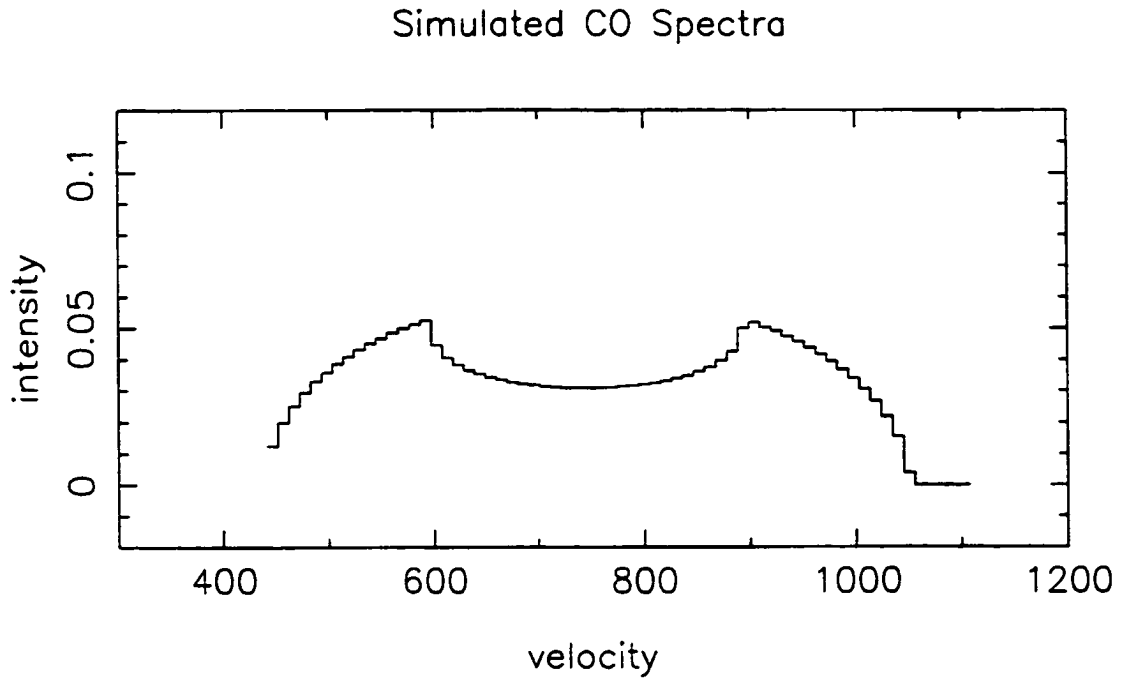
Figure B.6   The constant intensity ring spectrum. The radius is 15".

A Gaussian ring looks similar to the flat ring with less power a the high and low velocity ends and more in the mid velocity range as the hole intensity is not zero but dictated by the centre of the ring radius and the FWHM of the Gaussian. This is shown in figure B.7. Finally, a truncated Gaussian looks the same as the Gaussian ring with less power around the systemic velocity as in this case the intensity is indeed zero in the centre, shown in Figure B.8.

Simulated CO Spectra
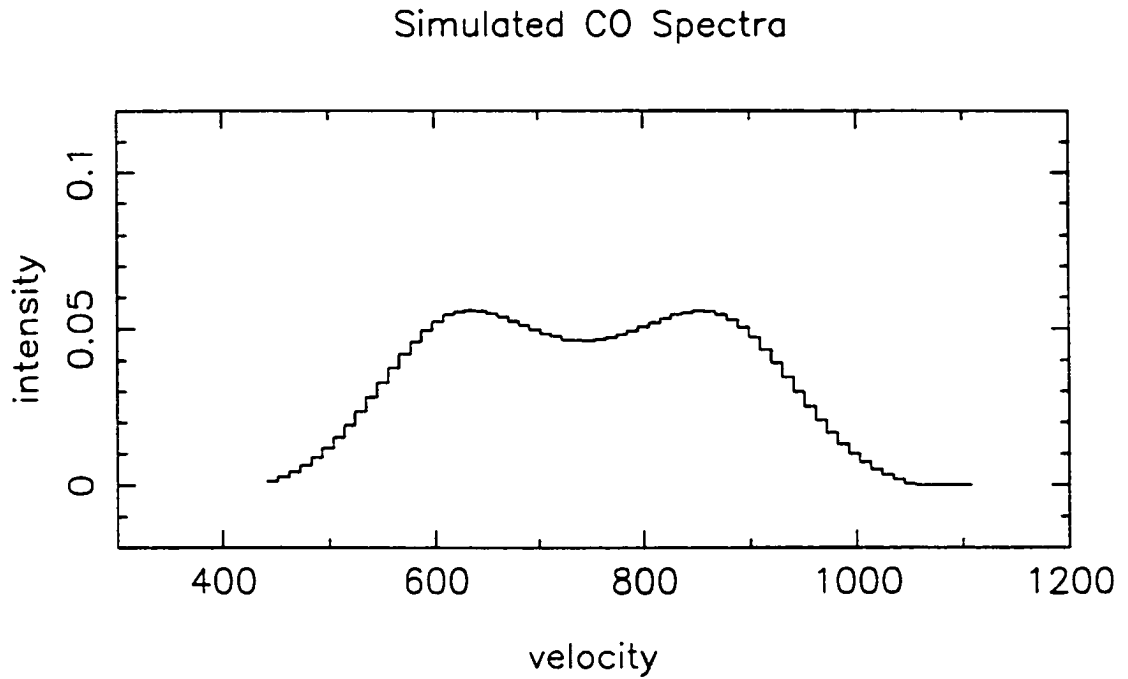
Figure B.7 The Gaussian ring spectrum. The radius is 15" and the FWHM is 15".

Simulated CO Spectra
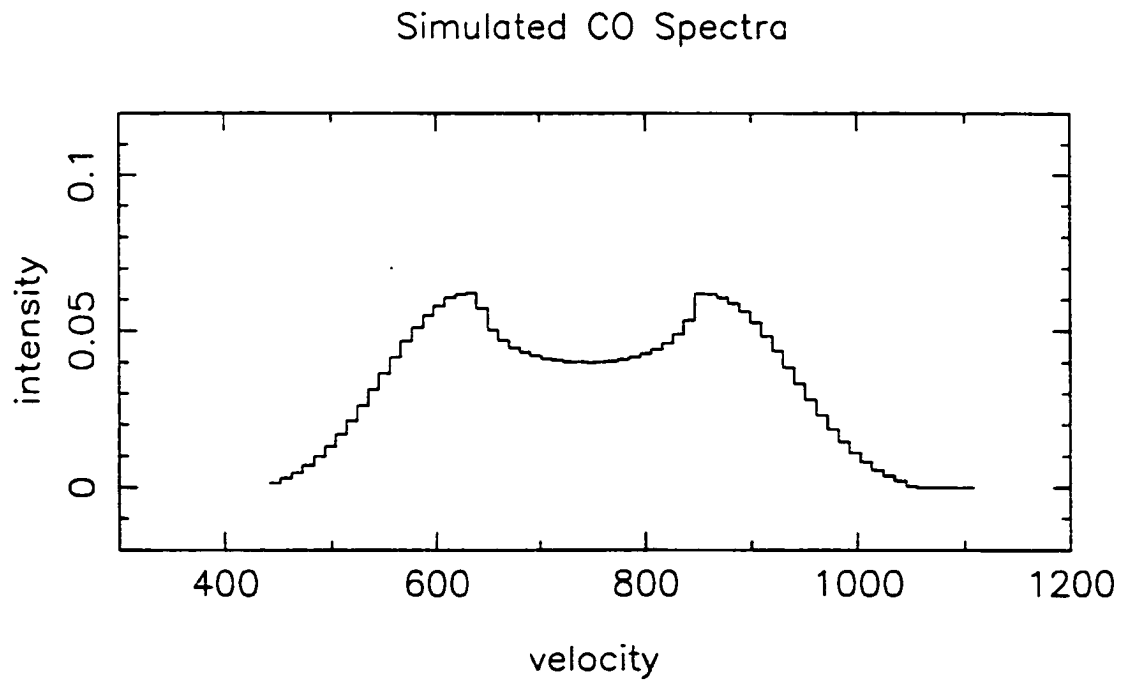
Figure B.8 The truncated Gaussian ring spectrum. The Gaussian peak radius is 15" and the FWHM is 15" and the truncated radius is 10".

B 3.4   Normalization

In the case of the work on NGC 5866, the simulated data are normalized to the 0,0 offset pointing data. The reduced zero offset data spectrum is integrated in order to get the area under the line. The program integrates the un-normalized synthetic spectrum and then divides by the specified area. The resulting ratio is displayed on the screen and is synthesizing the pointing the pointing from which the normalizing area was taken from. Naturally, there is a danger here since the ratio returned by the program is only useful when the user is simulating the pointing used for normalizing. Other pointing simulations produce useless ratios and so, the original normalization factor for that model should be entered when the program prompts the user for the value. This means that when running the same model for multiple pointings, the pointing data which were used for the normalizing area, NORM, must be simulated first in order to get a meaningful normalization factor for use on the other pointings. The normalization factor can be checked by running the same model with no normalization and multiplying the area under the area under the simulated line by the previously found normalizing factor. The result will be the same as the area under the observed spectrum.

B 3.5   The IRAM 30m Power Pattern Approximation

This work uses an approximation of the IRAM 30m telescope power pattern presented in Greve, Kramer & Wild (1998). Those authors used scans of the new and full moon to derive the parameters for the power pattern empirically. Scans were done for wavelengths between 0.8-3 mm, which encompass the ^{12}CO J=2-1 and ^{12}CO J=1-0 transitions. The work was done in late 1997, roughly a year prior to the NGC 5866

observations but after adjustments to the telescope surface which were made in July of 1997.

Greve, Kramer & Wild (1998) give the degraded power pattern as a Gaussian with corrections for the error beams written as:

$$F(\theta) = EXP[-(\sigma_r)^2]A_T(\theta) + \Sigma_i a_{ei} EXP[-(\pi\theta L_i / 2\lambda)^2]$$ (B.3)

where σ_r is the rms value of the wavefront deformation, $A_T(\theta)$ is the Airy-type pattern (diffraction beam) , a_{ei} is the amplitude of the ith error beam, L_i is the correlation length of the error distribution (for small scale random deformations in the reflector), λ is the wavelength and θ is the angular distance from the centre of the power pattern. This can be simplified by ignoring the small scale RMS errors ($\sigma_r = 0$) and writing the diffraction beam, A_T, as an approximate Gaussian:

$$A_T = EXP(-(2\sqrt{\ln 2}\theta / \theta_b)^2)$$ (B.4)

where θ_b is the FWHM equivalent of the diffraction beam. The side lobes can be simplified by using the expression:

$$\Sigma_i a_{ei} EXP[-(\pi\theta L_i / 2\lambda)^2 = \Sigma_i a_{ei} EXP[-(0.53\pi\theta / \theta_{ei})^2$$ (B.5)

Where the correlation length, L_i, equals $2*0.53\lambda/\theta_{ei}$, as given by standard tolerance theory (Greve, Kramer & Wild, 1998, and references therein), and θ_{ei} is the FWHM equivalent of the error beam. This gives a final relationship for the telescope power pattern with respect to θ as:

$$F(\theta) = EXP[-(\theta / .60\theta_b)^2] + \Sigma_i a_{ei} EXP[-(.53\pi\theta / \theta_{ei})^2]$$ (B.6)

where $1/(2\sqrt{\ln2})$ ≈ 0.60. The values of θ_b, a_{ci} and θ_{ci} are given in Greve, Kramer & Wild (1998) for the J=2-1 transition. The parameters for the J=1-0 were found by interpolating from their figure 5 data.

The power pattern subroutine works by adjusting the "observed" intensity unit area by unit area. The subroutine first translates the polar coordinates used in the spectral bin assignment part of the program to Cartesian coordinates and then gives it an XY position on the sky. The intensity of each unit is modified based on the projected distance from the power pattern centre and then rebinned in the appropriate velocity bin.

The power pattern was tested by making the model disk very small (.00001" across) to simulate a point source. The intensities were normalized to the 0,0 offset pointing and the model inclination was set to 0 (face on) so that all of the signal fell into the same velocity bin. For the J=1-0 transition the FWHM of the beam is 20.9". Stepping the beam across the disk produced a map of the power pattern. The same was done for the J=2-1 transition, FWHM of 10.5". Figure B.9 shows the approximation to the IRAM 30m power pattern from equation B.6 for the J=1-0 transition (as seen in lines 1098-1103 in the code) and the test results plotted on top.
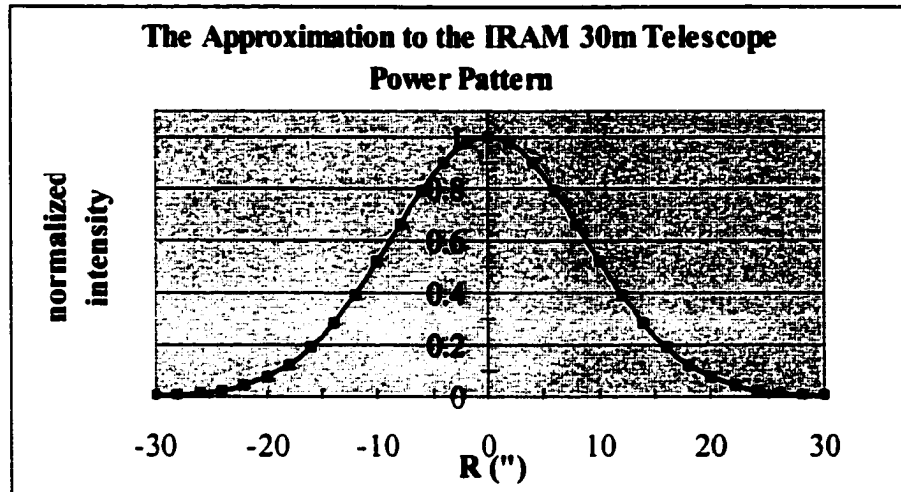
Figure B.9 The solid blue line shows the approximation to the IRAM 30m telescope from equation B.6 for the J=1-0 transition. The pink squares outline the test points obtained by making the disk 0.00001 " in diameter and moving the COSPEC power pattern offset in increments of 2".

B 3.6 Plotting

Plots are generated using the PGPLOT software package. The simulation is plotted as a spectrum with bins of a specified width. The velocity value of each bin is at its the centre.

When the observations and a model are plotted together the program needs to know how to match up the model and the data velocity bins since each has a slightly different velocity value. The program calls two bins the same only if the difference between the two velocity values is less than half of the bin width value. This ensures only one bin from each are considered the same and compared. This also ensures that the synthesized spectra and the data can be plotted on top of one another for visual comparison.

B.3.7 The "Goodness of Fit" parameter

The "Goodness" parameter was used as a measure of how well a particular model fit the data and is computed in the RMSCLAC subroutine. The idea is to compare bin by bin the synthesized spectra and the pointing data. The measure involves comparing the intensity value of each velocity bin from the model and the same velocity bin from the data. The differences between the intensity values for the same velocity bin are squared and the average uncertainty found (STD in the code). The average uncertainty then has the CLASS RMS value, the uncertainty associated with the observed data, subtracted from it in order to not count the intrinsic scatter in the signal and this corrected uncertainty is then multiplied by the value of the velocity range, in kms^{-1}, and divided by the total area under the data line. If the model is a perfect match then the goodness of fit parameter will return 0. To test this, real data from an actual pointing was sent through the subroutine as a substitute for model data. The Goodness parameter returned values on the order of zero to the 10th decimal place.

B.3.8 Velocity Dispersion

The average velocity dispersion value at a given radius is specified in the code (line 649). This value is sent to the GAUSSDEV function which uses it as the most probable value returned by a Gaussian random number generator (a Monte Carlo simulation based on the Box-Mueller algorithm, Bevington & Robinson, 1992). The Gaussian random number returned can either be positive or negative and is added to the velocity of the current unit area given by the rotation curve. In this fashion, the final observed velocity of any unit area can be higher or lower or the same as that given by the rotation curve and therefore

potentially placed in a different velocity bin then would have been otherwise. This feature was added in order to try and widen the simulated line width without having to raise the maximum rotation speed beyond that seen in the stars and the ionized gas.

The GAUSSDEV function was tested by running the same average velocity dispersion value (50 kms^{-1}) through the function and adding it to the same velocity that would be given by rotation (100 kms^{-1}) 5000 times. The result was a Gaussian distribution centred on 100 kms^{-1}.

B 3.9 Problems

Several limitations of the code have already been discussed. One of the problems intrinsic to the way the code works is in the binning procedure. When running a completely symmetric model where the centre velocity bin is exactly centred on the systemic velocity and the maximum and minimum velocities are evenly divisible by the bin widths, equal bin numbers away from the centre should have equal intensity values. The bin number is assigned by (line 712):

$$IVEL = ININT ((VTOOBS- RVEL1)/DVEL) \qquad (B.7)$$

where IVEL is the bin number, VTOOBS is the observed velocity, RVEL1 is the reference velocity and DVEL is the bin width. ININT is the FORTRAN function which converts a real number into an integer. To illustrate the problem imagine the case where the central bin is bin number 139. In this case equal velocity widths away from the centre bin should have the same intensity values, that is bin number 134 and bin number 144 should have equal intensity. However if the velocity, VTOOBS is a half integer value,

i.e. 22.5 kms^{-1}, then the bin number is not going to be symmetric.   For example:

IVEL = ININT ((-22.5 – -695)/5), IVEL = ININT(134.5) = bin number 135, or in the 20

kms^{-1} from the centre bin. On the other side, (22.5 - -695)/5 = 143.5 = ININT(143.5) =

144, or the 25 kms^{-1} from the centre bin. Fortunately this only happens when VTOOBS

falls on an half value and only creates an error of ~0.1%.

Another bug in the code is that when the value of the maximum and minimum rotation

velocities are not evenly divisible by the bin width, the lowest velocity bin gets the left

over intensity, making it artificially large. Fortunately that bin is usually suppressed by

the power pattern produces a negligible error.

B.4   The COSPEC Data Fitting Experiments for NGC 5866

This section is a short description of the methodology used in running the COSPEC

experiments for synthesizing the spectral data from NGC 5866. The quantitative details

of the bit fit results can be found in chapter 3 and details of the other experiments are

presented in appendix C. The modelling philosophy was to start with the simplest model

and build on the successes and failures of that until a model which most satisfactorily fit

the data was found.   The following outlines the successive iterations and gives a

qualitative description of each.

Often it was very easy to improve the fit to only one pointing so that the model matched

almost perfectly.   However, using the same model but pointing the power pattern at

another offset, resulted in a dramatic worsening of the model fit to the data. The goal

was to synthesize all of the pointing data with just one model. The overall "goodness of fit" for a model was judged on the basis of how well the model fit the four centremost pointings. This is somewhat subjective as averaging the goodness parameter for the 4 centremost pointings can often smear out widely varying matches for different pointing but the same model and often it was left to the eye to be the final judge. The criteria, then, is a low average goodness for the 4 centremost pointings and consistency in how well each pointing was matched with the data.

The model consisted of a 60" diameter, constant intensity disk with the observed stellar rotation curve as given by Fisher (1997) for NGC 5866. The obvious failure of this model is that the data suggest that the maximum rotational velocity is about 100 km/s higher than the observed stellar rotation curve allows. The telescope was centred at 745 km/s and the 0,0 offset spectrum data clearly show emission out to ~1100 km/s on the redshifted side and signal out to ~440km/s on the blueshifted side. Only a higher model rotational velocity can reproduce the observed line width. This problem is seen in all of the pointings. By having a maximum rotational velocity of 200 km/s at 30" the velocity range seen by the power pattern is too narrow. This model produces Gaussian shapes for the signal at all offset and cannot make the "saw tooth" pattern seen in the data for the outer pointings (i.e. -9,7, 9,-7, and 17,-14 offsets)

Fisher (1997) also gives a rotation curve defined by the ionized gas, as delineated by the [O III] line. This rotation curve also does not extend to sufficiently high velocities to reproduce the observed CO line width. However, some improvement is achieved because

of the fact that the [O III] data show two solid body regimes. The first regime features a rapid rise in velocity up to 68 km/s at 2.49", which is followed by a more gradual rise up to 203 km/s at 30". By having larger velocities at smaller radii, this rotation curve puts a larger range of velocities inside the power pattern (at the centre pointing) compared to the stellar rotation curve, and so produces a wider spectrum. Unfortunately the [OIII]-based rotation curve only improves the model slightly; the simulated line is still too narrow by about 200 km/s. One major improvement is that the offset pointing simulations reproduce the saw tooth shape seen in the data, only at the wrong velocity positions. The overall "goodness of fit" is not much different than that of the stellar rotation curve but the fact that the [O III] rotation curve can reproduce the observed shape of the spectra suggests what the actual rotation curve for the CO might be like qualitatively.

How should the optical rotation curves be modified to provide significantly better fits to the CO data? The first step in answering this question was to try a rotation curve which rose to 300 km/s at 30". This gave the immediate improvement in that the line width could now be ~600 km/s in theory. The main problem with this model is that too much of the high velocity is not seen by the 20.9" FWHM power pattern. To reduce this problem, several rotation curves were examined with kinks at various velocities and radii, like that seen in the ionized gas rotation curve. The most successful of these curves rose to 200 km/s at 10", and then to 305 km/s at 30". This rotation curve not only reproduced the observed line widths, irrespective of radial intensity distribution, for all pointings, but also displayed the saw tooth pattern at the appropriate velocities and produced "horns" seen in the 0,0 pointing data. This provides a closer match to the centre pointing data

since they clearly show a dip in the centre. The constant intensity disk model using this rotation curve provided reasonable fits although the outer pointings has too much power.

Once a rotation curve had been found that could reasonably reproduce the observed line width, various intensity distributions were tried using the best rotation curve. COSPEC allows the user to choose between 6 different intensity distributions. Following the methodology of before, the simplest distribution was modelled first and subsequent models of greater complexity introduced when the simpler model failed.

The first intensity distribution modelled after the constant intensity disk was an exponential disk. Various scale lengths were tried in order to assess how well this distribution would work. Fractional scale lengths below ~0.5 produce less satisfactory models than the constant intensity disk: The synthesized line widths are too narrow and integrated intensities at offset pointings are too small. Larger scale lengths (> 0.5) produce slightly better models than the constant intensity disk. The centre pointing remains about the same but the offsets are a little weaker and match the data better but on the whole unacceptable.

The Gaussian disk model results are comparable to the exponential disk models. This is not surprising since there is little difference in the nature of these models. Both peak at the centre and fall off at a characteristic rate defined by either the scale length for the exponential disk or the FWHM for the Gaussian disk. Small Gaussian FWHM fail to improve on the constant intensity disk model (FWHM < 0.5) while the larger FWHM (>

0.5) improve the model in the same fashion as the larger scale length exponential disk. No improvement over the exponential disk is found.

After trying the various disk models the next logical choice was to try various ring models for the intensity distribution. This seemed like the logical next step since the 0,0 offset pointing shows a clear dip in intensity around the systemic velocity. This can be interpreted as a hole in the centre of the intensity profile. As before, a constant intensity distribution was chosen first. The constant intensity ring model is the same as the constant intensity disk, only with zero intensity within a given radius. Using various different hole radii none of the flat ring models proved better than any previous model. These models predict too much power in the offset pointings, and generate synthetic lines broader than observed. The centre pointing can be improved slightly however.

The Gaussian ring models worked the best. These models take power out of the centre and distribute it further out while still dropping the intensity at large radii, so that predicted integrated intensities at outer offset pointings are not unacceptably large as in the flat ring models. Several peak intensity radii and Gaussian FWHM were tried. Varying the radius and the FHWM led to either too much power in the centre and not enough at large radii or vice versa. Through trial and error a balance which produced the best results was found. This was a radius of 15" and a FWHM of 15".

The final intensity distribution tried was the truncated Gaussian ring. These models did not improve on the Gaussian ring model enough to warrant its use. The centre pointing was improved but the offsets were given too much power. Overall these models worked

as well as the Gaussian ring but not better. Arguing for simplicity the Gaussian ring was chosen over the truncated Gaussian ring as the best intensity distribution to model NGC 5866.

Naturally, all of the varying intensity distribution might be improved by fine tuning the rotation curve which was chosen using the constant intensity disk model. The major problem in synthesizing the data was reproducing the observed line width. This could only be solved through the choice of an appropriate rotation curve and not intensity distribution. For this reason and simplicity sake, the best fitting rotation curve was assumed to be independent of intensity profile.

The final stage in the modelling was to incorporate asymmetries into the Gaussian ring profile in order to further match the data. These clouds were introduced at several locations inside the disk in order to create the proper effect on the spectrum at the proper velocities. Their spatial locations in the model do no represent anything physical as there is no unique placement that will produce a unique spectrum. Broad statements such as what side of the disk they need to be placed on can be made, however. The main areas where the Gaussian ring failed are that the velocity bins around the systemic velocity in the 0,0 offset data have too much power and the redshifted side in the of the line Gaussian ring model is too weak. This was corrected by placing "hot" and "cold" clouds in the ring profile, through trial and error, until a reasonable fit was reached.

After a best fit model had been found (see table 3.3) other mechanisms were suggested to account for the large line width and often weak outer pointing with respect to the models. In order to reconcile the CO line width and the predicted line width of both the stellar and ionized gas rotation curves, velocity dispersion was added to the models which used these rotation curves. The idea was that velocity dispersion would necessarily cause some "spill over" from the highest and lowest velocity bins given by the rotation curve and widen the line. The velocity dispersion relation to radius was taken from Fisher's (1997) data and a Gaussian random number generator was used to produce velocity dispersion values. Even with velocity dispersion, these models still could not widen the synthesized line width enough to be considered satisfactory.

Since many of the models reveal simulated spectra that are too powerful at the outer pointings, a tilt between the major axis of the disk and the line of power pattern pointings was introduced (this angle is not in the plane that determines whether the disk is face on or edge on). It was hoped that a small enough angle which could be blamed on pointing error might improve the fit. Large angles (10-20°) did improve the overall fit by ~10% over the best fit model but were not considered due to the implied unphysical nature of the CO distribution in NGC 5866. This would mean that the CO is not associated with the visible dust lane and so these models were disregarded.

Appendix C

COSPEC Experiment Results

The following tables list the results of the various trial and error experiments using COSPEC as described in appendix B and chapter 3. All model with less than 4 pointings simulated were clearly not going to fit the data and so abandoned. Table C.1 lists the rotation curve experiments using a constant intensity (flat) disk. Table C.2 shows various intensity distribution experiments and table C.3 shows the unused models, which had the major axis tilted with respect to the line of power pattern pointings. Note that for the Gaussian ring models, the quoted normalization factor will no longer work in the version of COSPEC presented here. If running these models, the new normalization factor which can be founded by simulating the 0,0 pointing will still produce the same goodness of fit value.

Table C.1 Constant intensity disk model with varying rotation curves.

systemic velocity (km/s)	745		pointing (")	offset (code) (")	CLASS RMS (K)
Transition	J=1-0		(")	(")	(K)
disk size (")	60		0,0	3	5.17E-03
tip (degrees)	90		-9,7	14	6.53E-03
			9,-7	-8	4.32E-03
			17,-14	-19	6.92E-03

mod. type	max r.V. (km/s)	kink V (km/s)	kink R (")	norm.co	pointing (")	Goodness	ave good
flat disk	200	200	30	1.52285E-04	0,0	1.23E+00	1.28E+00
Fisher					-9,7	1.63E+00	
1997					9,-7	1.08E+00	
stellar					17,-14	1.18E+00	
flat disk	203	68	2.49	1.52286E-04	0,0	8.97E-01	1.12E+00
Fisher					-9,7	1.49E+00	
1997					9,-7	9.32E-01	
[OIII]					17,-14	1.18E+00	
flat disk	320	300	10.5	1.52297E-04	0,0	2.25E-01	-
					-9,7	9.37E-01	
flat disk	320	200	10.5	1.52297E-04	0,0	2.89E-01	-
					-9,7	4.12E-01	
flat disk	260	220	10.5	1.52293E-04	0,0	3.18E-01	3.53E-01
					-9,7	3.52E-01	
					9,-7	3.60E-01	
					17,-14	3.82E-01	
flat disk	305	215	10.5	1.52296E-04	0,0	2.62E-01	3.04E-01
					-9,7	4.02E-01	
					9,-7	2.80E-01	
					17,-14	2.72E-01	
flat disk	305	215	10	1.52296E-04	0,0	2.50E-01	3.05E-01
					-9,7	4.10E-01	
					9,-7	2.71E-01	
					17,-14	2.89E-01	
flat disk	305	210	10	1.52296E-04	0,0	2.59E-01	2.96E-01
					-9,7	3.85E-01	
					9,-7	2.86E-01	
					17,-14	2.54E-01	

Table C.1 continued

mod. type	max r.V. (km/s)	kink V (km/s)	kink R (")	norm.co	pointing (")	Goodness	ave good
flat disk	305	200	5	1.52296E-04	0,0	1.86E-01	3.00E-01
					-9,7	4.31E-01	
					9,-7	2.46E-01	
					17,-14	3.36E-01	
flat disk	305	210	5	1.52296E-04	0,0	1.84E-01	3.28E-01
					-9,7	4.95E-01	
					9,-7	2.30E-01	
					17,-14	4.02E-01	
flat disk	305	200	15	1.52296E-04	0,0	4.69E-01	3.69E-01
					-9,7	4.71E-01	
					9,-7	4.50E-01	
					17,-14	8.72E-02	
flat disk	305	210	15	1.52296E-04	0,0	4.31E-01	3.43E-01
					-9,7	4.31E-01	
					9,-7	4.14E-01	
					17,-14	9.71E-02	
flat disk	305	220	15	1.52296E-04	0,0	3.96E-01	3.34E-01
					-9,7	4.14E-01	
					9,-7	3.78E-01	
					17,-14	1.48E-01	

Table C.2 COSPEC results for the morphology of the molecular gas in NGC 5866 using various intensity distributions. A full description of each parameter and how they were used can be found in appendix B.

max. rotational velocity (km/s)	305		(")	(")	(K)
Transition	J=1-0		0,0	3	5.17E-03
disk size (")	60		-9,7	14	6.53E-03
kink vel. in rot. curve (km/s)	200		9,-7	-8	4.32E-03
kink radius in rot. curve (")	10		17,-14	-19	6.92E-03
tip (degrees)	90				

mod. type	norm.co	sc. length frac. disk	ring rad. (")	FWHM frac. Disk	pointing (")	Goodness	ave good
falt disk	1.52272E-04	-	-	-	0,0	2.82E-01	2.89E-01
					-9,7	3.66E-01	
					9,-7	3.16E-01	
					17,-14	1.93E-01	
exp.disk	1.03707E-03	0.23	-	-	0,0	4.41E-01	4.56E-01
					-9,7	4.50E-01	
					9,-7	4.40E-01	
					17,-14	4.93E-01	
exp.disk	2.92856E-03	0.12	-	-	0,0	7.62E-01	7.95E-01
					-9,7	8.27E-01	
					9,-7		
					17,-14		
exp.disk	4.21134E-04	0.5	-	-	0,0	3.17E-01	2.72E-01
					-9,7	2.50E-01	
					9,-7	3.52E-01	
					17,-14	1.71E-01	
exp.disk	3.08441E-04	0.75	-	-	0,0	2.98E-01	2.50E-01
					-9,7	2.55E-01	
					9,-7	3.35E-01	
					17,-14	1.11E-01	
exp.disk	2.76349E-04	0.9	-	-	0,0	2.93E-01	2.50E-01
					-9,7	2.66E-01	
					9,-7	3.31E-01	
					17,-14	1.11E-01	
gauss disk	3.66070E-02	-	-	0.5	0,0	2.93E-01	2.87E-01
					-9,7	2.40E-01	
					9,-7	3.61E-01	
					17,-14	2.55E-01	

Table C.2 continued

mod. type	norm.co	sc. length frac. disk	ring rad. (")	FWHM frac. Disk	pointing (")	Goodness	ave good
gauss disk	5.11014E-02	-	-	0.25	0,0	5.25E-01	6.22E-01
					-9,7	7.20E-01	
					9,-7		
					17,-14		
gauss disk	3.70821E-02	-	-	0.75	0,0	2.76E-01	2.37E-01
					-9,7	2.43E-01	
					9,-7	3.31E-01	
					17,-14	9.97E-02	
gauss disk	3.95771E-02	-	-	0.9	0,0	2.76E-01	2.42E-01
					-9,7	2.70E-01	
					9,-7	3.25E-01	
					17,-14	9.87E-02	
flat ring	2.50979E-04	-	15	-	0,0	3.06E-01	5.34E-01
					-9,7	7.77E-01	
					9,-7	3.09E-01	
					17,-14	7.46E-01	
flat ring	1.61810E-04	-	5	-	0,0	2.35E-01	3.00E-01
					-9,7	4.11E-01	
					9,-7	3.14E-01	
					17,-14	2.41E-01	
flat ring	7.83385E-04	-	25	-	0,0	4.74E-01	7.91E-01
					-9,7	1.11E+00	
					9,-7		
					17,-14		
gauss ring	1.92533E-02	-	15	0.5	0,0	2.42E-01	2.53E-01
					-9,7	3.22E-01	
					9,-7	3.13E-01	
					17,-14	1.37E-01	
gauss ring	1.38360E-02	-	15	0.25	0,0	1.96E-01	2.24E-01
					-9,7	2.53E-01	
					9,-7	3.27E-01	
					17,-14	1.22E-01	

Table C.2 Continued

mod. type	norm.co	sc. length frac. disk	ring rad. (")	FWHM frac. Disk	pointing (")	Goodness	ave good
gauss ring	2.63565E-02	-	15	0.75	0,0	2.67E-01	2.72E-01
					-9,7	3.45E-01	
					9,-7	3.14E-01	
					17,-14	1.64E-01	
gauss ring	1.25393E-02	-	15	0.1	0,0	2.15E-01	3.67E-01
					-9,7	3.77E-01	
					9,-7	4.33E-01	
					17,-14	4.43E-01	
gauss ring	2.16626E-02	-	25	0.5	0,0	2.70E-01	3.79E-01
					-9,7	5.31E-01	
					9,-7	3.05E-01	
					17,-14	4.10E-01	
gauss ring	1.64336E-02	-	25	0.25	0,0	3.18E-01	5.59E-01
					-9,7	8.12E-01	
					9,-7	3.11E-01	
					17,-14	7.94E-01	
gauss ring	2.81339E-02	-	25	0.75	0,0	2.71E-01	3.28E-01
					-9,7	4.41E-01	
					9,-7	3.09E-01	
					17,-14	2.90E-01	
gauss ring	2.64582E-02	-	5	0.5	0,0	2.67E-01	2.40E-01
					-9,7	2.10E-01	
					9,-7	3.40E-01	
					17,-14	1.45E-01	
gauss ring	2.49370E-02	-	5	0.25	0,0	3.26E-01	4.51E-01
					-9,7	4.64E-01	
					9,-7	4.31E-01	
					17,-14	5.83E-01	
gauss ring	3.12108E-02	-	5	0.75	0,0	2.71E-01	2.39E-01
					-9,7	2.67E-01	
					9,-7	3.24E-01	
					17,-14	9.60E-02	

Table C.2 Continued

mod. type	norm.co	Trunc Rad. (")	ring rad. (")	FWHM frac. Disk	pointing (")	Goodness	ave good
Trunc.G.R.	2.61155E-04	3	15	0.25	0,0	1.92E-01	-
					-9,7	2.56E-01	
Trunc.G.R.	2.60685E-04	2.5	15	0.25	0,0	1.93E-01	-
					-9,7	2.54E-01	
Trunc.G.R.	4.40449E-04	5	7	0.25	0,0	2.03E-01	3.31E-01
					-9,7	2.96E-01	
					9,-7	4.02E-01	
					17,-14	4.24E-01	
Trunc.G.R.	2.65145E-04	5	15	0.25	0,0	1.85E-01	2.29E-01
					-9,7	2.70E-01	
					9,-7	3.31E-01	
					17,-14	1.31E-01	
Trunc.G.R.	2.78537E-04	7.5	15	0.25	0,0	1.84E-01	2.49E-01
					-9,7	3.14E-01	
					9,-7	3.37E-01	
					17,-14	1.60E-01	
Trunc.G.R.	2.61797E-04	3.5	15	0.25	0,0	1.90E-01	2.25E-01
					-9,7	2.58E-01	
					9,-7	3.29E-01	
					17,-14	1.24E-01	

Table C.3 Models run with the power pattern line of observations titled to the major axis

systemic velocity (km/s)	745		pointing	offset (code)	CLASS RMS
max. rotational velocity (km/s)	305		(")	(")	(K)
Transition	J=1-0		0,0	3	5.17E-03
disk size (")	60		-9,7	14	6.53E-03
kink vel. in rot. curve (km/s)	200		9,-7	-8	4.32E-03
kink radius in rot. curve (")	10		17,-14	-19	6.92E-03
tip (degrees)	90				

mod. type	tilt	norm.co degrees	ring rad. (")	FWHM frac. Disk	pointing (")	Goodness	ave good
gauss ring	3	2.59955E-04	15	0.25	0,0	1.96E-01	2.23E-01
					-9,7	2.49E-01	
					9,-7	3.27E-01	
					17,-14	1.21E-01	
gauss ring	5	2.60020E-04	15	0.25	0,0	1.96E-01	2.21E-01
					-9,7	2.43E-01	
					9,-7	3.26E-01	
					17,-14	1.18E-01	
gauss ring	10	2.60324E-04	15	0.25	0,0	1.96E-01	2.12E-01
					-9,7	2.17E-01	
					9,-7	3.24E-01	
					17,-14	1.11E-01	
gauss ring	20	2.61498E-04	15	0.25	0,0	1.95E-01	2.07E-01
					-9,7	1.51E-01	
					9,-7	3.19E-01	
					17,-14	1.61E-01	
gauss ring	15	2.60821E-04	15	0.25	0,0	1.95E-01	2.04E-01
					-9,7	1.82E-01	
					9,-7	3.21E-01	
					17,-14	1.20E-01	
gauss ring	17	2.61071E-04	15	0.25	0,0	1.95E-01	2.04E-01
					-9,7	1.68E-01	
					9,-7	3.20E-01	
					17,-14	1.32E-01	

Table C.3 Continued

mod. type	tilt	norm.co degrees	ring rad. (")	FWHM frac. Disk	pointing (")	Goodness	ave good
gauss ring	16	2.60943E-04	15	0.25	0,0	1.95E-01	2.04E-01
					-9,7	1.75E-01	
					9,-7	3.21E-01	
					17,-14	1.25E-01	
gauss ring	18	2.61207E-04	15	0.25	0,0	1.95E-01	2.04E-01
					-9,7	1.62E-01	
					9,-7	3.20E-01	
					17,-14	1.40E-01	
gauss ring	16.5	2.61006E-04	15	0.25	0,0	1.95E-01	2.04E-01
					-9,7	1.71E-01	
					9,-7	3.20E-01	
					17,-14	1.28E-01	

References

Balkowski, C. & Chamaraux, P., 1983, *A&ASS*, **51**, 331

Bertola, F., Buson, L.M. & Zeilinger, W.W., 1992, *ApJ*, **401**, L79

Bevington, Philip R. & Robinson, D. Keith, 1992, *Data Reduction and Error Analysis for the Physical Sciences, 2nd Edition*, McGraw-Hill, Inc., Toronto

Bica, E. & Alloin, D., 1987, *A&A*, **181**, 270

Bloemen, Hans, 1989, *ARA&A*, **27**, 469

Bothun, Gregory D., Romanishin, W., Strom, S.E., Strom, K.M., 1984, *AJ*, **89**, 1300

Burbidge, E. Margaret & Burbidge, G.R., 1960, *ApJ*, **131**, 224

Buta, R. & Crocker D.A, 1993, *AJ*, **105**, 1344

Caldwell, Nelson, Kennicutt, Robert & Schommer, Robert, 1994, *AJ*, **108**, 1186

Canzian, B., Mundy, L.G., & Scoville, N., 1988, *ApJ*, **333**, 157

Casoli, F. *et al.*, 1998, *A&A*, **331**, 451

Dame, T.M., Hartmann, Dap & Thaddeus, P., 2001, *ApJ*, **547**, 792

De Jong, T. *et al.*, 1984, *ApJ*, **278**, L67

D'Ercole, A. & Ciotti, L., 1998, *ApJ*, **494**, 535

Dressler, Alan, 1980, *ApJ*, **236**, 351

Dressler, Alan *et al.*, 1997, *ApJ*, **490**, 577

Dumke, M., Braine, J., Kraus, M., Zylka, R., Wielebinski, R. & Guelin, M., 1997, *A&A*, **325**, 124

Elmegreen, B.G., 1993, *ApJ*, **411**, 170

Faber, S.M. & Gallagher, J.S., 1976, *ApJ*, **204**, 365

Fisher, David, 1997, *AJ*, **113**, 950

Gallagher, J.S., Faber, S.M. & Balick, B., 1975, *ApJ*, **202**,7

Garcia-Burillo, S., Guelin, M. & Neininger, N., 1997, *A&A*, **319**, 450

Greve, A., Kramer, C. & wild, W., 1998, *A&ASS*, **133**, 271

Gunn, James E. & Gott III, J. Richard, 1972, *ApJ*, **176**, 1

Hamabe, Masaru, Kodaira, Keiichi, Okamura, Sadanori & Takase, Bunshiro, 1979, *Publ. Astron. Soc. Japan*, **31**, 431

Haynes, Martha P., Giovanelli, Riccardo, 1984, *AJ*, **89**, 758

Haynes, M.P., Herter, T., Barton, A.S. & Benensohn, J.S., 1990, *AJ*, **99**, 1740

Helou, George, Khan, Iffat R., Malek, Ladan & Boehmer, Lisa, 1988, *ApJSS*, **68**, 151

Henkel, C. & Wiklind, T., 1997, *SSRev*, **81**, 1

Hopkins, A.M., Connolly, A.J., Haarsma, D.B., & Cram, L.E., 2001, *AJ*, **122**, 288

Hubble, Edwin, 1936, *The Realm of the Nebulae*, Yale University Press, New Haven

Hunter, C. & Toomre, Alar, 1969, *ApJ*, **155**, 747

Ibata, Rodrigo, Irwin, Micheal, Lewis, Ferguson, Annette & Tanvir, Nial, 2001, *Nature*, **412**, 49

Icke V., 1985, *A&A*, **144**, 115

Jablonka, P., Martin, P., & Arimoto, N., 1996, *AJ*, **112**, 1415

Kenney, Jeffrey D.P. & Young, Judith S., 1989, *ApJ*, **344**, 171

Kennicutt, Jr., Robert C., 1998a, *ApJ*, **498**, 541

Kennicutt, Jr., Robert C., 1998b, *ARA&A*, **36**, 189

Knapp, Gillian R., 1998, Star Formation in Early Type Galaxies, eds. P. Carral & J. Cepa, ASP Conference Proceedings

Knapp, G.R. & Gunn, J.E., 1982, *AJ*, **87**, 1634

Leitherer, Claus & Heckman, Timothy, 1995, *ApJSS*, **96**, 9

Lequeux, J., Combes, F., Dantel-Fort, M., Cuillandre, J.C., Fort, B. & Mellier, Y., 1998, *A&A*, **334**, L9

Lesch, H., Biermann, P.L., Crusius, A., Reuter, H.P., Dahlem, M., Barteldrees, A & Wielebinshi, R., 1990, *MNRAS*, **242**, 194

Malhotra, S. *et al.*, 2000, *ApJ*, **543**, 634

Mathews, William G. & Baker, James C., 1971, *ApJ*, **170**, 241

Miller, Glenn E. & Scalo, John M., 1979, *ApJSS*, **41**, 513

Moore, Ben, Katz, Neal, Lake, George, Dressler, Alan & Oemler, Jr., Augustus, 1995, *Nature*, **379**, 613

New, Kimberly C.B., Tohline, Joel E., Frank, Juhan & Vath, Horst M., 1998, *ApJ*, **503**, 632

Oort, J.H., 1977, *ARA&A*, **15**, 295

Peimbert, Manuel, 1993, IAU Symp. 155, Planetary Nebulae, eds. R. Weinberger & A. Acker (Vardrecht, Kluwer) pg. 523

Pellegrini, S., 1994, *A&A*, **292**, 395

Pogge, Richard W. & Eskridge, Paul B., 1987, *AJ*, **92**, 291

Pogge, Richard W., & Eskridge, Paul B., 1993, *AJ*, **106**, 1405

Prada, F., Beackman, J.E., Castles, J., McKeith, C.D. & Greve, A., 1994, *ApJ*, **423**, L35

Prada, F., Manchado, A., Canzian, Blaise, Peletier, R.F., McKeith, C.D. & Beckman, J.E., 1996, *ApJ*, **458**, 537

Quillen, A.C., 2001, *ApJ*, in press

Regan, Michael W. *et al.*, 2001 *ApJ*, in press

Sage, L.J., 1993, *A&A*, **272**, 123

Sage, L.J. & Wrobel, J.M., 1989, *ApJ*, **344**, 204

Salpeter, Edwin E., 1955, *ApJ*, **121**, 161

Sancisi, R., 1976, *A&A*, **53**, 159

Sandage, Allan, 1961, *The Hubble Atlas of Galaxies*, Carnegie Institution of Washington, Washington, D.C.

Sandage, Allan, Freeman, Kenneth C. & Stokes, N.R., 1970, *ApJ*, **160**, 831

Sandage, Allan, Sandage, Mary & Kristian, Jerome eds., 1975, *Galaxies and the Universe*, The University of Chicago Press, Chicago

Sanders, D.B., Scoville, N.Z. & Solomon, P.M., 1985, *ApJ*, **289**, 373

Sellwood, J.A., 1996, *ApJ*, **473**, 733

Shang, Zhaohui *et al.*, 1998, *ApJ*, **504**, L23

Shields, Joseph C., 1991, *AJ*, **102**, 1314

Sofue, Yoshiaki, 1994, *Publ. Astron. Soc. Japan*, **46**, 173

Sofue, Yoshiaki, 1997, *Publ. Astron. Soc. Japan*, **49**, 17

Sofue, Yoshiaki, Tomita, Akihiko, Tutui, Yoshinori, Honma, Mareki & Takeda, Yoichi, 1998, *Publ. Astron. Soc. Japan*, **50**, 427

Spitzer, Jr., Lyman & Baade, Walter, 1951, *ApJ*, **113**, 413

Strong, A.W. *et al.*, 1988, *A&A*, **207**, 1

Sumin, A.A., Fridman, A.M., Khaud, U.A., 1991, *Sov. Astron. Lett.*, **17(5)**, 329

Taniguchi, Yoshiaki *et al.*, *AJ*, **108**, 468

Taylor, Christopher L., Kobulnicky Henry A., Skillman, Evan D., 1998, *AJ*, **116**, 2746

Telesco, C.M. & Gatley, Ian, 1984, *ApJ*, **284**, 557

Thronson Jr., Harley A. & Telesco, C.M., 1986, *ApJ*, **311**, 98

Thronson Jr., Harley A., *et al.*, 1989, *ApJ*, **344**, 747

Tully, R. Brent, 1988, *Nearby Galaxies Catalog*, Cambridge University Press, Cambridge, UK

Ulrich, M.H., 1978, *ApJ*, **219**, 424

Van den Bergh, Sidney, 2000, *PASP*, **112**, 529

Wang & Hui, 1994, AAS meeting ,184, #49.02

Wang, Zhong, 2001, private communication

Welch, G.A., 2001, private communication

Welch, G.A. & Sage, L.J., 2001 in preparation

Wiklind, T. & Henkel, C., 1989, *A&A*, **225**, 1

Wiklind, T. & Henkel, C., 1990, *A&A*, **227**, 394

Wilson, Christine D., 1994, *ApJ*, **434**, L11

Wilson, Christine D., 1995, *ApJ*, **448**, L97

Wrobel, J.M. & Kenney D.P., 1992, *ApJ*, **399**, 94

Young, J.S. & Scoville, N.Z., 1991, *ARA&A*, **29**, 581

Young, Judith S., *et al.*, 1995, *ApJSS*, **98**, 219

Andrew LeBlanc

218 Centennial Drive
Moncton, NB, E1E 3Y2
(506) 389-9511 (Home)

EDUCATION:

1999-2001
M.Sc. in Astronomy, October 2001, Saint Mary's University, Halifax, NS

1994-1998
B.Sc. in Physics, minor in Philosophy, May 1998, Mount Allison University, Sackville, NB

1991-1994
High School Diploma, Honours, Moncton High School

RELEVANT EXPERIENCE:

2001
Senior lab instructor for the physics component of the Forensics program at Saint Mary's university. This included preparing and overseeing the labs, coordinating the lab demonstrator, ensuring the safety of the students and lecturing when the course professor was absent.

2000-2001
Tutorials for the first year physics class, Saint Mary's University. This involved preparing problems from the text book and presenting them to the students in a way that would allow them to gain a better understanding of the course material. This was a part time faculty position.

2000
Coordinated an internet based astronomy class at Saint Mary's University along with other graduate students. Responsibilities included overseeing and marking tests and exams along with handling any problems that came up during the course because the class professor teaches at the University of Hawaii.

1999-2001

Telescope tour guide for the public at the Burke-Gaffney Observatory, Saint Mary's University.

First year physics lab demonstrator, Saint Mary's University.

Canadian Astronomical Society (CASCA) graduate student representative for Saint Mary's University.

1998-1999

Research assistant for Dr. Bob Hawkes at Mount Allison University. Responsibilities included equipment preparation, data reduction and analysis.

Junior Physics lab technician. Responsibilities include setting up labs, coordinating lab demonstrators and ensuring that the labs are run smoothly and safely.

1998

Prepared and delivered several first year Astronomy lectures at Mount Allison University.

Researcher at Bubble Technology Industries, Chalk River, ON. This position was funded through the Deep River Science Academy and involved taking on 2 honours high school students to supervise and grade in the research for 6 weeks in order to give them a better understanding of what "science in the real world" is like. The students prepared a report, a presentation for professional research scientists and a poster presentation for the general public. The students received Ontario high school credits in a co-op program.

1995-1998

Physics lab demonstrator at Mount Allison University. Several classes were covered including: first year physics, 3rd year biophysics and introductory Astronomy.

PUBLICATIONS:

Full Refereed Journal Articles

LeBlanc, A.G., Murray, I.S., Hawkes, R.L., Campbell, M.D., Brown, P., Worden, S.P., Jenniskens, P., Correll, R.R., Montague, T., Babcock, D.D., 2000, *Monthly Notices of the Royal Astronomical Society*, 313, L9-L13, "Evidence for Transverse spread in Leonid Meteors"

Campbell, M.D., Brown, P.G. , LeBlanc, A.G., Hawkes, R.L., Jones, J., Worden, S.P. and Correll, R.R., 2000, *Meteoritics and Planetary Science*, 35, 1259-1268, "Electro-Optical Results from the 1998 Leonid Shower: I. Atmospheric Trajectories and Physical Structure"

Fisher, A.A., Hawkes, R.L., Murray, I.S., Campbell, M.D., and LeBlanc, A.G., 2000, *Planet. Space Sci.*, 48, 911-920, "Are most meteoroids really dustballs?"

Brown, P., Campbell, M.D., Ellis, K.J., Hawkes, R.L., Jones, J., Gural, P., Babcock, D.D., Barnbaum, C., Bartlett, R.K., Medard, M., Bedient, J., Beech, M., Brosch, N., Clifton, S., Connors, M., Cooke, B., Goetz, P., Gaines, J.K., Gramer, L., Gray, J., Hildebrand, A.R., Jewell, D., Jones, A., Leake, M., LeBlanc, A.G., Looper, J.K., McIntosh, B.A., Montague, T., Morrow, M.J., Murray, I.S., Nikolova, S., Robichaud, J., Spondor, R., Talarico, J., Theijsmeijer, C., Tilton, B., Treu, M., Vachon, C., Webster, A.R., Weryk, R., and Worden, S.P., 2000, *Earth Moon Planets*, 82-83, 167-190 "Global Ground-Based Electro-Optical and Radar Observations of the 1999 Leonid Shower: First Results"

Internal Publications and Conference Proceedings

LeBlanc, A.G., Welch, G.A., and Sage, L.J., 2001, poster presentation, CASCA conference, Hamilton, ON, May 26-29, 2001, "Properties of the Molecular ISM in the Lenticular Galaxy NGC 5866"

Hawkes, R.L., Campbell, M.D., LeBlanc, A.G., Parker, L., Brown, P., Jones, J.,Worden, S.P., Correll, R.R , Woodworth, S.C., Fisher, A.A., Gural, P., Murray, I.S., Connors, M., Montague, T., Jewell, D., Babcock, D.D., 2000, *Proceedings IAU 181 Dust in the Solar System and Other Planetary Systems*, "The Size of Meteoroid Constituent Grains: Implications for Interstellar Meteoroids"

Brown, P., Jones, J., Hawkes, R.L., LeBlanc, A., Campbell, M., Worden, P., Murray, I., Correll, R., Montague, T., Gray, J., 1999, *Leonid 1998 Electro-Optical Final Report* (to CRESTech, U.S. Space Command and other funding organizations), Oct. 15, 1999 (72 pages)

Correll, R.R., Campbell, M.D., LeBlanc, A.G., Worden, S.P., Hawkes, R.L., Montague, T., Brown, P., 1999, *Proc. of Leonid Meteor Storm and Satellite Threat Conference* (Los Angeles: Aerospace Corp. and AIAA, April 1999) "Electro-Optical Observational Results of the 1998 Leonid Shower

REFERENCES

Dr. Bob Hawkes
Physics Department Head
Mount Allison University
67 York St.
Sackville N.B.
E4L 1E6
(506) 364-2582
rhawkes@mta.ca

Dr. Tom McLean
Supervisor, R&D
Bubble Technology Industries
Highway 17
Chalk River, ON
K0J 1J0
(603) 589-2456
mailroom@bubbletech.ca

Dr. Gary Welch
Associate Professor
Astronomy & Physics
Saint Mary's University
Halifax, NS
B3H 3C3
(902) 420-5637
gwelch@ap.stmarys.ca